



TUM School of Computation, Information and Technology

# **Fiber-Optic Multimode Interference Sensing and Imaging**

Kun Wang

Vollständiger Abdruck der von der TUM School of Computation, Information and Technology der Technischen Universität München zur Erlangung des akademischen Grades eines

Doktors der Ingenieurwissenschaften

genehmigten Dissertation.

Vorsitz: Prof. Dr.-Ing. Gerhard Rigoll  
Prüfer\*innen der Dissertation: 1. Prof. Dr.-Ing. habil. Dr. h.c. Alexander W. Koch  
2. Prof. Yosuke Mizuno, Ph.D.

Die Dissertation wurde am 17.04.2023 bei der Technischen Universität München eingereicht und durch die TUM School of Computation, Information and Technology am 11.11.2023 angenommen.



# Contents

<b>Abstract</b>	<b>1</b>
<b>1. Introduction</b>	<b>3</b>
1.1. Background . . . . .	3
1.1.1. Optical Fiber Sensors . . . . .	4
1.1.2. Fiber-Optic Imaging . . . . .	5
1.2. Aims and Objectives . . . . .	6
1.3. Dissertation Overview . . . . .	7
<b>2. Fundamentals and State of the Art</b>	<b>9</b>
2.1. Optical Fiber Characteristics . . . . .	9
2.1.1. Numerical Aperture . . . . .	11
2.1.2. Number of Modes . . . . .	12
2.2. Multimode Fiber Sensing . . . . .	12
2.2.1. Sensing Principle . . . . .	12
2.2.2. State of the Art . . . . .	14
2.2.3. Discussion and Summary . . . . .	20
2.3. Multimode Fiber Imaging . . . . .	23
2.3.1. State of the Art . . . . .	23
2.3.2. Discussion and Summary . . . . .	30
<b>3. Characterization of Standard Multimode Fibers</b>	<b>33</b>
3.1. Principles . . . . .	33
3.2. Comprehensive Characterization . . . . .	35
3.2.1. Core Diameter Dependence . . . . .	35
3.2.2. Numerical Aperture Dependence . . . . .	37
3.2.3. Length Dependence . . . . .	40
3.3. Strain-Insensitive Temperature Measurement . . . . .	43
3.4. Summary . . . . .	46
<b>4. Temperature and Strain Sensing Based on Square-Core Fiber</b>	<b>47</b>
4.1. Sensor Fabrication and Principle . . . . .	47

4.2. Temperature and Strain Measurement . . . . .	51
4.3. Strain-insensitive Temperature Measurement . . . . .	54
4.4. Summary . . . . .	56
<b>5. Core-Offset-Based Temperature and Strain Sensing</b>	<b>59</b>
5.1. Sensor Fabrication and Principle . . . . .	59
5.2. Temperature and Strain Measurement . . . . .	61
5.3. Discussion . . . . .	67
5.4. Summary . . . . .	69
<b>6. Multimode Fiber Imaging with Deep Learning</b>	<b>71</b>
6.1. Multimode Fiber Imaging System . . . . .	71
6.1.1. Experimental Setup . . . . .	71
6.1.2. Setup Calibration . . . . .	73
6.1.3. Multimode Fiber Imaging Data Acquisition . . . . .	75
6.1.4. Deep Learning Architectures . . . . .	77
6.2. Multimode Fiber Imaging Reconstruction: Handwritten Digits . . . . .	78
6.2.1. Neural Networks . . . . .	80
6.2.2. Image Reconstruction through Multimode Fibers . . . . .	83
6.2.3. Imaging Reconstruction under Thermal Perturbation . . . . .	84
6.2.4. Discussion . . . . .	92
6.3. Multimode Fiber Imaging Reconstruction: Natural Images . . . . .	92
6.3.1. Multi-Hidden-Layer Fully Connected Neural Network . . . . .	93
6.3.2. U-Net . . . . .	95
6.3.3. Discussion . . . . .	95
6.4. Summary . . . . .	96
<b>7. Conclusion and Outlook</b>	<b>99</b>
7.1. Conclusion . . . . .	99
7.2. Outlook . . . . .	102
<b>List of Symbols</b>	<b>105</b>
<b>List of Abbreviations</b>	<b>107</b>
<b>List of Figures</b>	<b>108</b>
<b>List of Tables</b>	<b>113</b>
<b>Acknowledgments</b>	<b>117</b>

<b>Bibliography</b>	<b>118</b>
<b>Publications</b>	<b>137</b>

# Abstract

Optical fibers, especially multimode fibers (MMFs), show unique physical properties in sensing and imaging. It has been proven that the multimode interference (MMI) phenomenon in MMF can improve the performance of optical fiber sensors and fiber-optic imaging systems. A variety of optical fiber sensors have been developed. However, the demand for higher sensitivity and multi-parameter sensing is still growing, which motivates this presented study to improve the temperature and strain sensitivity of the MMI-based optical fiber sensors. The blossom of machine learning methods significantly promotes the practical usability of the MMF imaging system. It provides the other motivation to study the robustness of the MMF imaging system to thermal perturbations, which is unavoidable and would enhance the performance of the imaging systems.

A comprehensive characterization of the standard MMF-based optical fiber sensors is conducted experimentally to evaluate the core diameter, numerical aperture, and the length dependences of the temperature and strain sensitivities of a single-mode–multimode–single-mode (SMS) structure. This study is complementary to the theoretical analysis of the SMS structures.

According to the literature research and the comprehensive study, the methodology improvement focuses on new specialty MMFs and optical fiber sensor configurations. First, an MMI-based fiber sensor is developed using a new specialty fiber, square-core fiber, for temperature and strain sensing. The sensor configuration is the SMS structure consisting of a segment of square-core fiber, and the experimental results are compared to other specialty fibers with conventional circular core shapes. The proposed fiber sensor can also exhibit strain-insensitive high-sensitivity temperature sensing. Besides, another MMI-based fiber sensor is demonstrated with a core-offset SMS structure for temperature and strain sensing. The sensitivity dependences on the core-offset amplitudes at the input and output single-mode fiber (SMF)/MMF boundaries are experimentally analyzed. These two studies show that new specialty fibers and structures are promising to enhance the sensitivity of MMI-based fiber sensors. Their simplicity, cost efficiency, and robustness also contribute to the design and development of SMS structures in the future.

An MMF imaging system combined with deep learning is developed to study two factors that limit its practical usability. Two neural networks, i.e., fully connected neural networks (FCNN) and U-Net, are designed and adapted for image reconstruction through an MMF.

The first factor, the thermal perturbation on the MMF imaging system, is studied by reconstructing the MNIST handwritten digits dataset with both neural networks in the temperature range of 25 to 75°C. The reconstructed images of simulated and experimental data are compared. The second factor, the complexity of the images for the neural networks, is demonstrated by the revival of the natural images dataset. A multilayer FCNN and U-Net are tested and compared. This study is prominent for the practical use of the MMF imaging system in medical endoscopic imaging and industrial applications.

# 1. Introduction

Unnoticeably, optical fibers have become the backbone of our daily lives. When we are on the Internet, making video calls, or sharing files, they are all through optical fibers. Without optical fibers, having all the current facilities we have gotten used to would be impossible. Nowadays, the world is being "fibered."

## 1.1. Background

For a long time, optical systems took a backseat in technology development until the laser was invented in the 1960s [1]. It became realistic to have a workable and practical optical system in the near future. At that time, the propagation of laser beams in the atmospheric environment was established. It was also well-known that glass can be shaped into thin and flexible threads to guide light. However, due to the high transmission loss, transmitting information through such threads was still impossible. Among different materials that have been studied, fused silica, which is composed of  $SiO_2$ , was the most suitable one. Still, even so, the light transmitted in fused silica was attenuated by at least one-third after a distance no longer than 1 m. Apparently, it has no use. At just the right time, in 1966, Kao and Hockham made a breakthrough with their discovery in fiber optics [2]. They predict the strong attenuation of glass was not an intrinsic property but rather caused by chemical impurities in the glass composition. Their careful calculation of how to transmit light over long distances in optical glass fibers predicted the possibility of producing glass with an attenuation no more than 20 dB/km instead of the 1000 dB/km common at that time. In 1969, the first graded index fiber was presented with an attenuation below 100 dB/km [3]. Since then, tremendous progress in this direction has been achieved. In 1969, the first graded index fiber was presented with an attenuation below 100 dB/km. Only one year later, the first single-mode fiber (SMF) with an attenuation below 20 dB/km was created [4]. Later, by fine-tuning the manufacturing procedure, the attenuation of 4 dB/km was achieved. With a better understanding that the loss is wavelength-dependent, the milestone of 1 dB/km was reached in 1976 [5]. Finally, in 1979, a loss of only 0.2 dB/km at 1550 nm [6], which is very close to the limit of what is possible at all with fused silica, was realized. As fiber began to be deployed, with the development of manufacturing, various auxiliary components arose,

too. The evolution in optical fibers not only matured optical communications [7, 8] but also led to the advent of optical fiber sensors [9, 10], even optical fiber-based imaging today.

As optical fiber product maturity developed rapidly, the properties of optical fibers have been studied exhaustively [11–13]. Optical fiber sensors have been promising sensing devices for years due to the notable intrinsic characteristics developed from optical fiber properties, for example, light weight, immunity to electromagnetic, and resistance to corrosive and hazardous environments. The density of fused silica is  $\sim 2.2 \text{ g/cm}^3$ , and that of copper wire is  $\sim 8.9 \text{ g/cm}^3$ . It is not so much realizable by comparing the densities. In a realistic comparison, 1 km of bare fiber only weighs  $\sim 30 \text{ g}$ , while 1 km of copper wire weighs  $\sim 36.6 \text{ kg}$ . In this case, it is a rule of thumb that 1 g of fiber cable replaces 10 kg of electrical cable. It clearly indicates the advantage where a weight limit is required, like on vehicles, ships, or even spacecraft.

Optical fiber ( $\text{SiO}_2$ ) is an excellent insulating material with resistivity as high as  $1 \times 10^{18} \text{ } \Omega/\text{cm}$ . Therefore, even close to high-voltage installations, there is no interference gathered by the fiber. This feature enables the optical fiber to be immune to electromagnetic. In the application with strong electromagnetic fields, even if the short circuit happens, the occurrence of fire can be avoided due to the transmission medium. Moreover, silica is chemically quiet, and the protective jackets of optical fibers are usually also made of inert materials. Therefore, optical fiber cables can be deployed in harsh environments where metallic parts would corrode quickly.

### 1.1.1. Optical Fiber Sensors

Over the last two decades, optical fiber sensors have grown tremendously, and now the technology offers significant practical benefits over electrical sensors due to their intrinsic characteristics, such as compact size, lightweight, fast response, immunity to electromagnetic interference, remote sensing capabilities, as well as resistance to corrosive and hazardous environments [14–17]. Besides, optical fiber sensors are able to measure multiple measurands independently and simultaneously. Therefore, numerous research efforts have been devoted in the past several decades. Thanks to the advancement of fabrication techniques for optical fibers and related accessories, numberless discrete structures and methods have been created and reported. Among them, several have received significant attention, like fiber Bragg gratings (FBGs) [18, 19], long-period gratings (LPGs) [20, 21], Raman scattering [22, 23], Brillouin scattering [24, 25], surface plasmon resonance [26], etc. The most prominent FBG sensors have been employed for various real-world applications, including structural health monitoring, biomedical, gas, etc [27, 28]. Therefore, FBG sensors have been produced massively.

Nevertheless, the utility of these optical fiber sensors requires the consideration of so-

phisticated equipment, cost, fabrication complexity, and stability, for example. Another option is an easy-to-fabricate and low-cost structure utilizing the discrete single-mode–multimode–single-mode (SMS) fiber structure based on multimode interference (MMI), which offers enhanced sensitivity and selectivity. [29, 30]. The so-called SMS structure is composed of a short segment of multimode fiber (MMF) sandwiched between two single-mode fibers (SMFs). Besides the unique spectral features and high sensitivity of MMI-based sensors, the fabrication is easily feasible and relatively low-cost using a standard fusion splicer. Therefore, it has received substantial attention in the last decade, and a variety of sensors have been designed, like temperature sensors [31, 32], strain sensors [33, 34], humidity sensors [35, 36], curvature sensors [37, 38], biomedical sensors [39, 40], vibration sensors [41], and chemical sensors [42, 43].

However, with the growing need for optical fiber sensors, e.g., higher sensitivity or multi-parameter sensing, some questions still need to be answered, and further research is necessary. An everlasting requirement is to improve the measurement sensitivity. Besides, the crosstalk that occurred in multi-parameter sensing is undesired, meaning further study is highly needed.

### **1.1.2. Fiber-Optic Imaging**

Due to the optical transmission properties of fiber to transmit an image from end to end, fiber-optic imaging caught the attention of researchers. To accomplish this, most fiber-optic imaging uses an SMF bundle to collect an image of the target. The bundle contains hundreds/thousands of identical individual SMFs, as one SMF is only capable of transmitting one pixel of the target image. Fiber-optic imaging has been widely used in medical endoscopy, i.e., fiber-optic endoscopes, which are pliable and highly maneuverable as the fibers can be easily bent and twisted. It allows access to channels in the human body that semirigid instruments cannot access at all or can access only at great discomfort to the patients. However, access to small tissues is still limited as the SMF bundle usually has a millimeter thickness.

The image transmitted through MMFs has the potential to revolutionize the current fiber-optic endoscope. Because MMF can transmit multiple spatial modes of light simultaneously, which, in principle, could replace the SMF bundle with a few hundred microns thick MMF. It will open up new, less invasive endoscopes to perform high-resolution imaging of tissues out of reach of current endoscopes. Therefore, since 1967 the first reported analog transmission of images through an MMF [44], for half a century, scientists have sought ways to use MMF to transmit images. Particularly, based on imaging in scattering media, measuring the phase and amplitude of the electromagnetic wave coming out of the MMF and using these measurements to infer the relationship between the input and the output of

the MMF. For example, remarkable techniques include analog phase conjugation [45–47], digital phase conjugation [48–51], and the transmission matrix (TM) method [52–54]. The TM method, which measures both the phase and amplitude of the output patterns corresponding to multiple input images to create a matrix of complex numbers relating the input to the output, is currently the most widely used. This TM can be used to project the output pattern, display the input images, or reconstruct the input images from the output patterns.

These methods are dependent on phase measurement, which is also their drawback. There are mainly two reasons. First, phase measurement requires a nontrivial apparatus. An extra reference beam is usually brought to the output of the fiber to generate an interference pattern, which contains the complex optical field (amplitude and phase). Although reference-beam-less phase measurement has been reported, multiple quadrature phase measurements must be done for the phase extraction. The other reason is that the phase is sensitive to ambient perturbations, e.g., thermal perturbation and fiber bending, which results in significant changes in the phase. It is possible to calibrate these changes; however, this complicates the setup and implementation. A method that can simplify the imaging system and is robust to the perturbations will bring MMF imaging to the next level of practical applications.

## 1.2. Aims and Objectives

This dissertation aims to improve the temperature and strain sensitivity of the MMI-based optical fiber sensors and investigate the robustness of the MMF imaging system to thermal perturbations. The development of the methodology is summarized as follows:

1. A comprehensive characterization of standard MMFs. Although MMFs have been widely used for sensing and various MMI-based optical fiber sensors have been reported, the question of the sensitivity dependences based on the principle of SMS structure still needs to be answered. Considering the assumptions of the sensing principle of the SMS structure, an experimental characterization is preferred, which will offer a guideline for designing the MMI-based optical fiber sensors.
2. Investigation on new specialty MMF. The unique properties of specialty optical fiber are very likely to introduce a possibility of sensitivity enhancement. Besides, it matures the study of specialty optical fibers and opens up other potentials for further implementation. An SMS structure consisting of a specialty MMF, which has the potential to improve sensitivity, should be studied.
3. Design of a new configuration of MMI-based optical fiber sensors. The easiest way to generate MMI is to use the SMS structure. Nevertheless, the conventional SMS

structure only excites a few higher-order modes in the MMF section. Based on the principle of SMS structure, which is that higher-order modes may improve sensitivity, a new configuration for higher-order modes of excitation should be designed and tested.

4. Superiorities of machine learning in MMF imaging against thermal perturbation. Machine learning has been proven to be robust for reconstructing the images transmitted through the MMF, but it significantly suffers from thermal perturbation and geometric deformation. The robustness needs to be investigated quantitatively, which will benefit the further use of MMF imaging, for example, in medical endoscopy. In general, the performance of machine learning is limited by the complexity of the images. Different neural networks should be tested on natural images, which will broaden the application of optical-fiber-based endoscopic imaging.

## 1.3. Dissertation Overview

This dissertation contains seven chapters. In this chapter, a general background of this study, which starts with a brief history of optical fibers, is presented. The scientific problems, the aim, and the objectives of this study are described.

Chapter 2 introduces the fundamentals and literature research of MMI-based optical fiber sensors and MMF imaging. First, the main characteristics of optical fibers are summarized. Then, the principle of MMI-based optical fiber sensors is presented, followed by the state of the art of MMI-based fiber sensors and the related discussion. A literature review and discussion of MMF imaging are given at the end.

Chapter 3 shows a comprehensive characterization of the standard MMF-based SMS structure for temperature and strain sensing to investigate the sensitivity dependences on the core diameter, the numerical aperture (NA), and the length of the MMF. According to the comprehensive study, a strain-insensitive temperature fiber sensor based on MMI implementing a section of standard MMF is proposed and verified experimentally.

Chapter 4 proposes an optical fiber sensor for temperature and strain measurement using a new specialty fiber, i.e., square-core fiber. The sensor configuration is the SMS structure consisting of a segment of square-core fiber, and the experimental results are compared to other specialty fibers with conventional circular core shapes. The results indicate that the proposed fiber sensor can exhibit strain-insensitive high-sensitivity temperature sensing.

Chapter 5 demonstrates an MMI-based fiber sensor with a core-offset SMS structure for temperature and strain sensing. The sensitivity dependences on the core-offset amplitudes at the input and output SMF/MMF boundaries are experimentally analyzed. Additionally,

pull tests are performed to evaluate the mechanical strengths of the core-offset SMS structures.

Chapter 6 presents the MMF imaging system with deep learning. The MMF imaging system is illustrated, and the data acquisition is described. Further, two neural networks are trained with different datasets to reconstruct the images transmitted through an MMF, which indicates the robustness of deep learning in MMF imaging. To investigate the current research problems in MMF imaging, thermal perturbations are applied and tested with these two verified neural networks. Finally, the retrieval of natural images transferred through an MMF is studied using different neural networks.

## 2. Fundamentals and State of the Art

As optical fibers are widely used in sensing and imaging applications, the theoretical background of optical fibers is introduced for a better understanding. The development of multimode fiber sensors is dropped, and the state of the art of multimode fiber imaging is presented in the following. The current research challenges are discussed, and further developments in multimode fiber sensing and imaging are proposed.

### 2.1. Optical Fiber Characteristics

Optical fiber is a flexible kind of optical waveguide of clear glass, which is capable of carrying information in the form of light. It confines electromagnetic waves within its interface by the principle of total reflection and directs the optical waves along the optical fiber axis. The most commonly used glass for optical fibers is fused silica (quartz glass, amorphous silicon dioxide  $SiO_2$ ), either in pure form or with some dopants. The classic structure of an optical fiber contains the core, cladding, and coating, as shown in Fig. 2.1, where  $a$  and  $b$  represent the radius of the core and cladding, respectively. The core is the central region of an optical fiber in which the light is guided. The area directly surrounding the core is called fiber cladding. The diameter of the cladding is commonly chosen to be  $125\ \mu\text{m}$ , a standard value recommended by the International Telecommunication Union Telecommunication Standardization Sector (ITU-T). The coating is a non-glass layer applied to the optical fiber to offer mechanical protection to the glass.

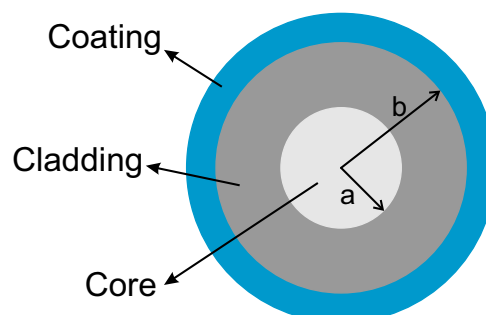


**Figure 2.1.:** Schematic of the cross-section of a standard optical fiber.

Depending on the number of modes allowed to propagate in the optical fiber, two catalogs can be observed and classified: single-mode fiber (SMF) and multimode fiber (MMF). The mode is generally defined as the path of optical wave transmission. Single-mode fibers usually have a relatively small core (with a diameter of only a few micrometers) and support only a single propagation mode (disregarding the fact that there are two different polarization directions). Multimode fibers have a much larger core and support multiple modes with different intensity distributions. Common types of MMF are 50/125  $\mu\text{m}$  and 62.5/125  $\mu\text{m}$  fibers, having a core diameter of 50  $\mu\text{m}$  and 62.5  $\mu\text{m}$ , respectively, and a cladding diameter of 125  $\mu\text{m}$ . Multimode fibers are mainly categorized into step-index (SI) and graded-index (GI) fibers. The comparison of SMF, step-index MMF, and graded-index MMF are compared in Fig. 2.2.

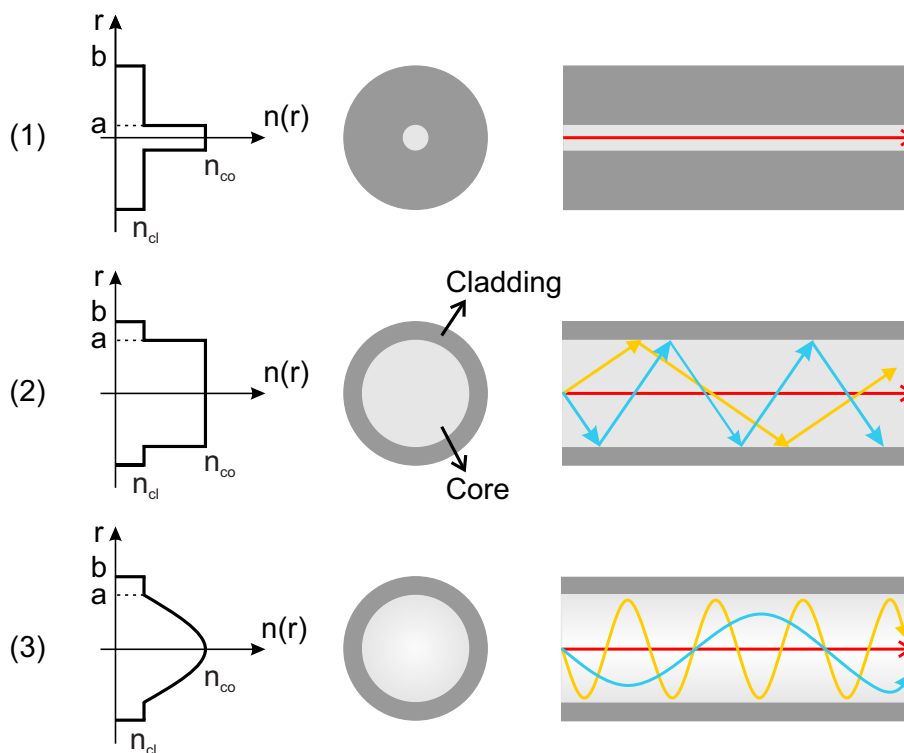


**Figure 2.2.:** Comparison of (1) single-mode fiber, (2) step-index multimode fiber, and (3) graded-index multimode fiber.

The step-index MMF is a type of fiber in which the core has a uniform refractive index (RI) right up to the interface of the core and cladding where a sharp index change occurs, as shown in Fig. 2.2(2), where  $a$  is the core radius,  $b$  is the cladding radius,  $n_{co}$  is the RI of core, and  $n_{cl}$  is the RI of cladding. When  $r = a$ , the RI changes in a step-like fashion.

The graded-index MMF is a type of fiber whose core has a radially decreased RI from the

center of the core to the interface of core and cladding. When light is injected into a GI fiber, the light travels faster at the edge of the core than in the center, as shown in Fig. 2.2(3).

When light is injected into a step-index MMF, the propagation velocity of each mode is highly dependent on the incident angle. The light injected at a larger angle (light way in blue in Fig. 2.2(2)) propagates at a slower velocity, and correspondingly the path length is longer. Different modes travel different path lengths through the fiber, which leads to a modal dispersion problem. However, when the light is injected into a graded-index MMF, different modes travel in curved paths with nearly equal travel time, which greatly reduces modal dispersion in the MMF.

In this dissertation, as only step-index MMF is used, the following characters will be introduced only for step-index MMF. The MMF represents step-index MMF without specification.

### 2.1.1. Numerical Aperture

Numerical Aperture (NA) represents an estimation of the maximum acceptance angle for most multimode fibers but not for single-mode fibers. Qualitatively, NA is a measure of the light-gathering ability of a fiber. In the ray model of light, a ray's angle of incidence determines whether it will be coupled into the fiber core. The cutoff angle is the maximum acceptance angle ( $\theta_{max}$ ), which is related to the NA, as illustrated in Fig. 2.3. Rays with an angle of incidence  $\leq \theta_{max}$  are totally internally reflected at the boundary between the fiber core and cladding. To occur the total internal reflection (TIR), the RI of the core ( $n_{co}$ ) must be larger than that of the cladding ( $n_{cl}$ ).

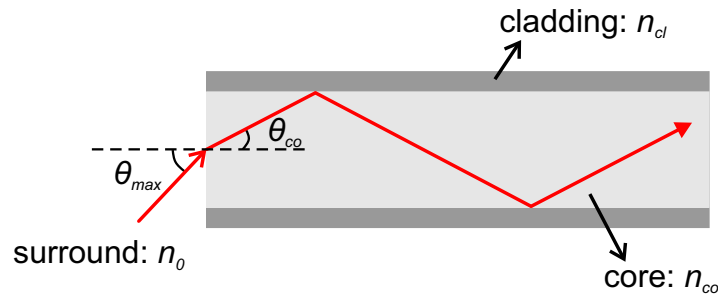


**Figure 2.3.:** Numerical aperture of optical fiber.

The NA of step-index fiber is defined as

$$NA = n_0 \sin \theta_{max} = \sqrt{n_{co}^2 - n_{cl}^2}, \quad (2.1)$$

which indicates that NA is determined only by the refractive indices of the core and the cladding. Note that the NA is independent of the RI of the medium surrounding the fiber.

If an input medium has a higher RI, the maximum input angle will be smaller, while the numerical aperture remains unchanged.

### 2.1.2. Number of Modes

The number of modes allowed to propagate in the optical fiber can be estimated by

$$N_m = \frac{g}{2(g+2)} V^2, \quad (2.2)$$

where  $g$  is the RI profile parameter and  $V$  is the normalized optical frequency, which is also simply called  $V$  number. It is defined mathematically as

$$V = \frac{2\pi}{\lambda} a (NA), \quad (2.3)$$

where  $\lambda$  is the vacuum wavelength,  $a$  is the radius of the fiber core, and  $NA$  is the numerical aperture. Various essential properties of an optical fiber are relevant to  $V$  numbers, and the value of  $V$  is the decisive criterion to establish how many modes an optical fiber can support. When  $V < 2.405$ , the optical fiber only supports one mode per polarization direction, i.e., SMF. Multimode fibers can have much higher  $V$  numbers, the number of supported modes of a step-index and graded-index MMF can be estimated by Eq. 2.2. When  $g \rightarrow \infty$ , it is a step-index MMF; when  $g = 2$ , it is a graded-index MMF. Therefore, the number of modes in a step-index MMF can be calculated approximately as

$$N_m \approx \frac{V^2}{2}. \quad (2.4)$$

## 2.2. Multimode Fiber Sensing

Since the simplest MMI-based fiber structure, i.e., SMS fiber structure, was reported, a variety of MMI-based fiber sensors were developed. However, the sensing principle is founded on the basic SMS fiber structure.

### 2.2.1. Sensing Principle

The SMS structure consists of a short MMF section with ends connected to the SMFs. The injected light is guided from the input SMF into the MMF and propagates along with the MMF. At the first SMF/MMF boundary, the spot-size difference between the fundamental modes in the SMF and MMF excites multiple modes in the MMF, which propagate with their own propagation constants. At the second SMF/MMF boundary, the net field coupled to

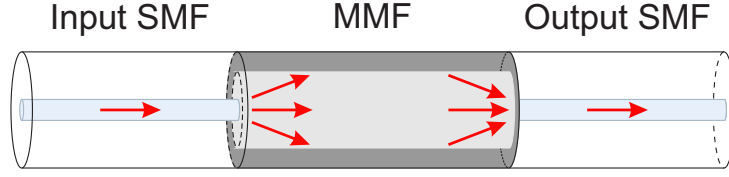


**Figure 2.4.:** Schematic of the basic SMS fiber structure.

the output SMF is determined by the relative phase differences among the many modes guided in the MMF. Based on the assumption that the SMFs and MMF are axially aligned, the modes excited in the MMF are axially symmetric. The power in the output SMF  $P_{out}$  can be given as

$$P_{out} = |A_0^2 + A_1^2 e^{i(\beta_0 - \beta_1)L} + A_2^2 e^{i(\beta_0 - \beta_2)L} + \dots|^2, \quad (2.5)$$

where  $\beta_m$  is the propagation constant of the  $m$ -th mode, and  $A_m$  is the field amplitude determined by the modal overlap between the fundamental mode of the SMF and the concerned  $m$ -th symmetric mode of the MMF, defined as

$$A_m = 2\pi \int_0^\infty \Psi_S \Psi_m r dr. \quad (2.6)$$

By using a well-known Gaussian approximation, the fundamental modal field of the single-mode fiber can be written as

$$\Psi_S(r) = \sqrt{\frac{2}{\pi}} \frac{1}{w_S} e^{(-r^2/w_S^2)}, \quad (2.7)$$

where  $w_s$  is the Gaussian spot size of the mode. It can be approximated as

$$\frac{w_S}{a_S} = \left[ 0.65 + \frac{1.619}{V_S^{3/2}} + \frac{2.879}{V_S^6} \right]; \quad 0.8 \leq V_S \leq 2.5, \quad (2.8)$$

here,  $a_S$  and  $V_S$  represent the core radius and the  $V$ -number of the SMF, respectively.

The step-index MMF is characterized by the following refractive-index profile

$$n(r) = \begin{cases} n_{co}; & r \leq a_M \\ n_{cl}; & r \geq a_M \end{cases}, \quad (2.9)$$

where  $n_{co}$  is the RI of the MMF core,  $n_{cl}$  is the RI of the MMF cladding, and  $a_M$  is the core radius of the MMF. The modal field for the  $m$ -th mode can be obtained by

$$\Psi_m(r) = \begin{cases} \frac{A}{J_0(U)} J_0\left(\frac{Ur}{a_M}\right); & r \leq a_M \\ \frac{A}{K_0(W)} K_0\left(\frac{Wr}{a_M}\right); & r \geq a_M \end{cases}, \quad (2.10)$$

with

$$U = a_M (k_0^2 n_{co}^2 - \beta_m^2)^{1/2} \quad (2.11)$$

and

$$W = a_M (\beta_m^2 - k_0^2 n_{cl}^2)^{1/2}, \quad (2.12)$$

where  $A$  is a constant,  $k_0$  is the free-space wave number,  $m = 0, 1, 2, \dots$  and  $\beta_m$  is the corresponding constant that are calculated numerically by the eigenvalue equations as

$$U \frac{J_1(U)}{J_0(U)} = W \frac{K_1(W)}{K_0(W)}. \quad (2.13)$$

Substituting the propagation constants and modal field distributions in Eq.2.5 and Eq.2.6, the power in the output SMF  $P_{out}$  can be calculated.

## 2.2.2. State of the Art

The MMI-based fiber sensors are suitable for many measurement scenarios. In recent years, the demand for higher measurement sensitivity and multi-parameter sensing has led to the rapid growth of various MMI-based fiber sensors with distinct structures.

### I. Basic SMS Structure

The conventional SMS structure is, at this point, the most common one, shown in Fig. 2.5(a), and is used for different physical parameter measurements. In 2007, Liu and Wei [55] proposed a basic SMS fiber sensor for strain and temperature sensing. The strain and temperature sensitivities were  $18.6 \text{ pm}/\mu\epsilon$  and  $58.5 \text{ pm}/^\circ\text{C}$ , respectively. In 2011, Gong et al [56] presented a curvature sensor using the same structure, which could be applied to measure very small curvatures over a relatively large scale by suitably choosing to measure the wavelength shifts or intensity changes. The maximum sensitivity based on wavelength shift was  $-10.38 \text{ nm}/\text{m}^{-1}$ . In the same year, Wu et al. [57] used the same structure for displacement and temperature sensing. However, the spectral dip shifted to shorter wavelengths with increasing displacement but longer wavelengths with increasing temperature. Therefore, it was not practicable to discriminate between displacement and temperature. A

bent SMS fiber sensor was introduced to distinguish the displacement and temperature by measuring changes in both the central wavelength and bandwidth of the spectrum. The realized sensitivity was  $5.89 \text{ pm}/\mu\text{m}$  for displacement and  $11.6 \text{ pm}/^\circ\text{C}$  for temperature. Upon this structure, Huang et al. [58] showed an SMS fiber sensor implemented with a section of multimode polymer optical fiber (POF) for measuring large strains up to  $2 \times 10^4 \mu\epsilon$  with a sensitivity of  $-1.72 \text{ pm}/\mu\epsilon$ . Numata et al. [59] studied a similar SMS fiber sensor consisting of a section of perfluorinated graded-index POF for temperature and strain measurement in 2014. The achieved sensitivities were  $-112 \text{ pm}/\mu\epsilon$  and  $49.8 \text{ nm}/^\circ\text{C}$ , respectively.

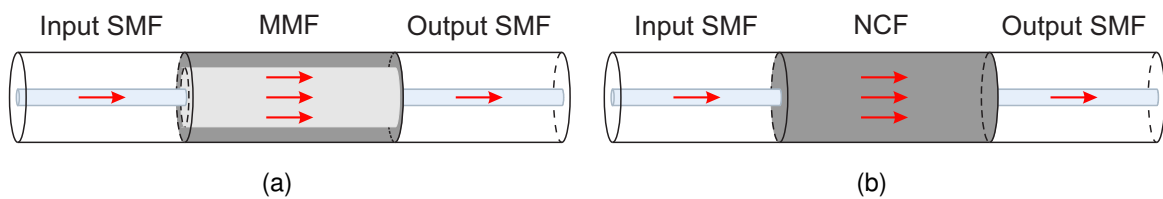


**Figure 2.5.:** Schematic of (a) basic SMS fiber structure and (b) basic SMS composed of NCF.

Instead of using the MMF in the basic SMS structure, the no-core fiber (NCF) is an attractive alternative to function as the multimode section and enhance sensitivity. Silva et al. [60] demonstrated an ultrahigh-sensitivity temperature fiber sensor based on a basic SMS structure using a section of NCF. The sensor was proposed to measure RI changes of a surrounding medium to determine the temperature dependence in a high-sensitivity RI range. The achieved maximum temperature sensitivity was  $-1880 \text{ pm}/^\circ\text{C}$  in the range of  $0$  to  $80^\circ\text{C}$ . The same structure was studied for RI sensing by Chen et al. [61], and the obtained maximum sensitivity was  $259.85 \text{ nm}/\text{RIU}$  (RIU: refractive index unit). Besides, this structure was also used as a salinity sensor for the NaCl solution with a salinity range from  $3.86\%$  to  $21.62\%$ , and the maximum sensitivity of  $19.4 \text{ pm}/\%$  was realized.

## II. MMI-based Fiber Sensor with Etched/Polished MMF

The etched/polished MMF reduces the diameter in the MMF section, which results in the evanescent field penetrating further into the surroundings, and the sensitivity increases. The schematic configurations of utilized MMI-based structures with a short segment of etched/polished MMF are shown in Fig. 2.6. In 2000, Ren Xi Gao et al. [62] investigated temperature sensing in liquid with an MMF, in which the cladding was evenly etched with Hydrofluoric acid, as shown in Fig 2.6(a). The achieved maximum sensitivity was  $0.001^\circ\text{C}$  at a particular temperature range of  $52\text{--}60^\circ\text{C}$ . Besides, the authors also demonstrated that this structure could be further used as an RI sensor for liquids [63], which proved that this structure is suitable for various scenarios. Continually, Yong Zhao et al. [64] proposed this

structure as an RI sensor with the MMF diameter etched to 40  $\mu\text{m}$ , where the maximum RI sensitivity of 286.2 nm/RIU was obtained in the RI range from 1.33 to 1.75.

Similar to the basic SMS structure, the NCF has also been implemented in the etched SMS structure to improve sensitivity. In 2017, Yamile Cardona-Maya et al. [65] analyzed this configuration with a section of etched NCF as an RI sensor and applied a simple fast Fourier transform (FFT) measurement technique with an optical spectrum analyzer (OSA) to realize simultaneous real-time monitoring. The obtained maximum sensitivity was 1442 nm/RIU in the RI range from 1.32 to 1.35 with the enhancement of using an indium tin oxide (ITO) deposition. Meanwhile, Omar Fuentes et al. [66] proposed a liquid level sensor with this configuration. After the NCF diameter was etched to 50  $\mu\text{m}$ , the achieved maximum sensitivity was 0.41 nm/mm, which was 2.77 times the sensitivity before etching (0.15 nm/mm).

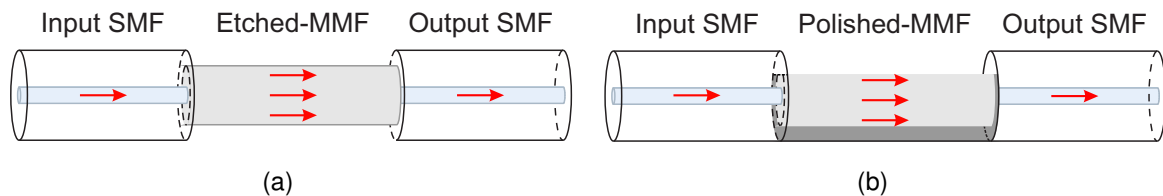


**Figure 2.6.:** Schematic of the SMS fiber structure composed of (a) etched MMF and (b) polished MMF.

At the same time, Jieyuan Tang et al. [67] investigated a side-polished SMS structure as a RI sensor as well, as shown in Fig. 2.6(b). The polished MMF has advantages as various materials can be easily coated onto the surface of the MMF. The maximum sensitivity of 65 nm/RIU was obtained with a polished depth of 20.6  $\mu\text{m}$ , which was the optimal polished depth and led to the highest sensitivity. The same structure was used by Xianfan Wang et al. [68] as relative humidity (RH) sensor, which could work over a relatively high-temperature range that many RH sensors based on moisture-sensitive material coatings cannot perform. The authors proved that the RH sensitivity is related to the polished surface roughness. Higher roughness results in increased RH sensitivity. Therefore, the maximum RH sensitivity was obtained at around 0.069 dB/%RH within the humidity range of 30%RH to 90%RH for a relatively high-temperature environment of 70 to 90°C.

Additionally, Xianfan Wang et al. [69] reported a double-polished SMS structure for RI sensing inspired by the one-sided polished SMS structure. The results showed the sensing performance with a high dependence on polished depth. The maximum measured RI sensitivity was 151.29 nm/RIU in the RI range of 1.3450 to 1.4050.

### III. MMI-based Fiber Sensor with Tapered MMF

Though etched/polished MMI-based structures have many advantages, they increase fabrication difficulties, and meanwhile, the induced surface roughness also influences measurement sensitivity. Alternatively, the tapered fiber structure can replace the etching/polishing process, as shown in Fig. 2.7(a). Because light, guided in a tapered fiber, has a significant fraction of power propagating in the evanescent wave. Consequently, the effective index of the guided mode is affected by the RI of the external medium. It is well known that the fraction of power in the evanescent wave increases at small taper diameters. Thus, the sensitivity to environmental changes increases as well. In 2011, Pengfei Wang et al. [70] proposed this structure as an RI sensor theoretically and experimentally with a 30  $\mu\text{m}$  MMF taper waist diameter. The obtained maximum sensitivity was 1913 nm/RIU in the RI range of 1.33 to 1.44. Recently, Biyao Yang et al. [71] tried to apply this structure as a curvature sensor. The optimum waist diameter was about 68.7  $\mu\text{m}$  for balanced consideration. An average sensitivity of  $-21.734 \text{ dB/m}^{-1}$  over the range of  $0.7064 \text{ m}^{-1}$  to  $1.9129 \text{ m}^{-1}$  and the maximum sensitivity of  $-144.876 \text{ dB/m}^{-1}$  at a curvature of  $1.9129 \text{ m}^{-1}$  have been achieved.

As mentioned in Section 2.2.2. I, NCF is regularly used in the MMI-based structure. Some researchers further investigated tapered NCF. Claudecir R. Biazoli et al. [72] demonstrated the SMS structure with a tapered NCF with a waist diameter of 55  $\mu\text{m}$  for RI sensing. The maximum sensitivity of 2946 nm/RIU in the RI range of 1.42 to 1.43 was attained. Furthermore, Ricardo M. André et al. [73] also studied the same structure for strain sensing. Several taper waists were analyzed, and the measurement sensitivity increased with the taper waist diameter decreased. When the taper diameter was down to 15  $\mu\text{m}$  from 125  $\mu\text{m}$ , the maximum sensitivity was  $-23.69 \text{ pm}/\mu\epsilon$ . The conclusion indicates the possibility of measuring strain and temperature simultaneously by combining two different tapered structures with different strain and temperature sensitivities.

Later, in 2015, Qizhen Sun et al. [74] proposed a fiber sensor based on an SMS structure with Fresnel reflection, as shown in Fig. 2.7(b), for simultaneous measurement of RI and temperature. A standard SMF was tapered down to several micrometers in diameter to form the multimode microfiber (MMMf) to function as an MMF. The light transmits through the structure and generates one Mach-Zehnder interferometer (MZI), then it is reflected at the end face of SMF due to the Fresnel reflection. The reflected MZI pattern is injected into the MMMf again; thus, the other MZI is produced at the first taper region. Therefore, a reflection spectrum, also an intensity-modulated interference spectrum is obtained. By demodulating the fringe power and free spectrum range (FSR) of the spectrum, RI sensitivities of  $-72.247 \text{ dB/RIU}$  and  $68.122 \text{ nm/RIU}$ , as well as temperature sensitivities of  $0.0283 \text{ dB}/^\circ\text{C}$  and  $-17 \text{ pm}/^\circ\text{C}$  were achieved.

In the same year, Yong Zhao et al. [75] experimented with a new RI sensor based on a

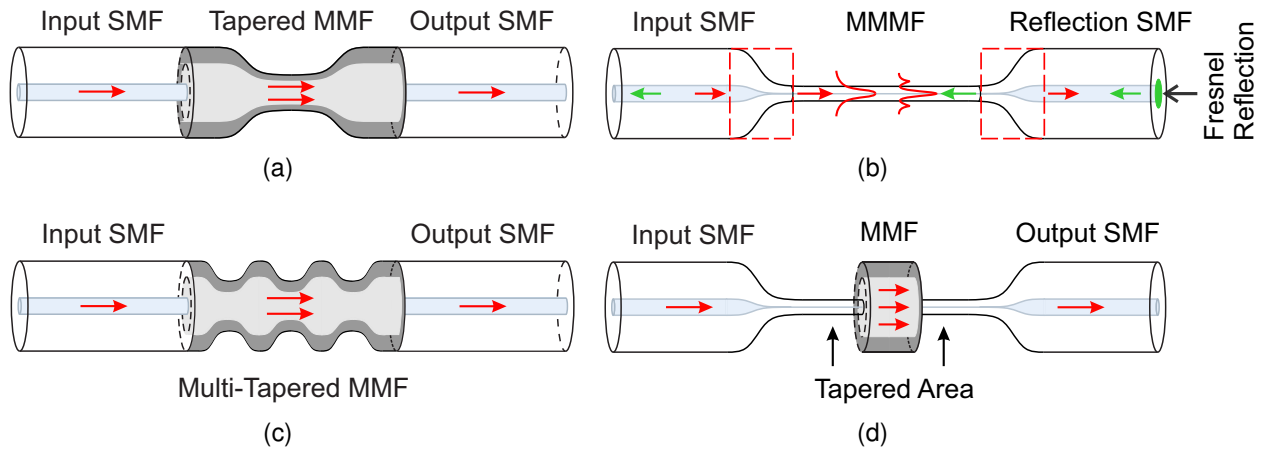


**Figure 2.7.:** Schematic of SMS structure with tapered fiber: (a) tapered MMF; (b) tapered multi-mode microfiber (MMMMF) combining Fresnel reflection; (c) multi-tapered MMF; and (d) MMF sandwiched between two half-tapered SMFs.

multi-tapered SMS structure, as shown in 2.7(c). The sensors were fabricated with three tapers, five tapers, and eight tapers to reveal the influence of the taper number on the RI sensitivity theoretically and experimentally. The maximum measuring sensitivity of 261.9 nm/RIU was obtained when the number of tapers was up to eight. The conclusion indicates that the number of tapers, the higher the RI sensitivity achieved.

In 2016, Guoyong Sun et al. [76] studied the MMF sandwiched between two half-tapered SMFs, as illustrated in 2.7(d). This structure did not require any tapering or cladding elimination of the MMF, and the half-tapers of the SMF did not need to be too thin. Therefore, this structure can endure highly longitudinal stress, measured at 4000  $\mu\epsilon$ , until breaking, nearly equal to conventional SMS structure. The response sensitivity monotonically increases to the maximum value of 500.6 nm/RIU when the RI varies from 1.333 to 1.411.

#### IV. Cascade of MMI-Based Fiber Sensors

With the development of MMI-based structures, some other new structures are brought into different applications. The new configurations can keep the advantages of the conventional SMS structure, such as easy fabrication, compactness, and low cost. Meanwhile, they also can improve measurement performance. In 2008, Linh Viet Nguyen et al. [77] proposed a high-temperature fiber sensor with an SMF-MMF-SMF-MMF-SMF (SMSMS) structure, as shown in Fig.2.8(a). The two sections of MMF are very short and play the role of mode couplers so that a clear interference pattern can be obtained between the core mode of the MMF-SMF-MMF (MSM) segment and the cladding modes. It illustrates that though several

cladding modes of the SMF are excited, typically, one high-order cladding mode is dominant and interferes with the core mode. The measurement range was up to  $900^{\circ}\text{C}$  stably, and a maximum sensitivity of  $0.088\text{ nm}/^{\circ}\text{C}$  could be reached. Similarly, in 2012, Yue Ma et al. [78] extended the same structure as an RI sensor, which took advantage of the reaction of the evanescent wave of the cladding modes to the surrounding RI variation. A sharp interference spectrum was obtained, and the dip wavelength shifted as a function of surrounding RI. By comparing different lengths of sensing SMF, it was demonstrated that the sensitivity increases with a longer sensing SMF. A maximum sensitivity of  $188\text{ nm}/\text{RIU}$  was obtained when the length of SMF was  $40\text{ mm}$ . It also identified that this structure could provide a tailorable sensing performance and good reproducibility. Later in 2014, Rui Xiong et al. [79] demonstrated that this structure could also be used for measuring temperature and RI simultaneously by the wavelength shifts of the two wavelength transmission dips formed by the cladding modes interfering with the core mode. The experimental results indicated that the sensitivities of RI and temperature were  $-37.9322\text{ nm}/\text{RIU}$  and  $0.0522\text{ nm}/^{\circ}\text{C}$  within the RI range from 1.3105 to 1.3517 and the temperature range of  $25$  to  $85^{\circ}\text{C}$ , respectively.

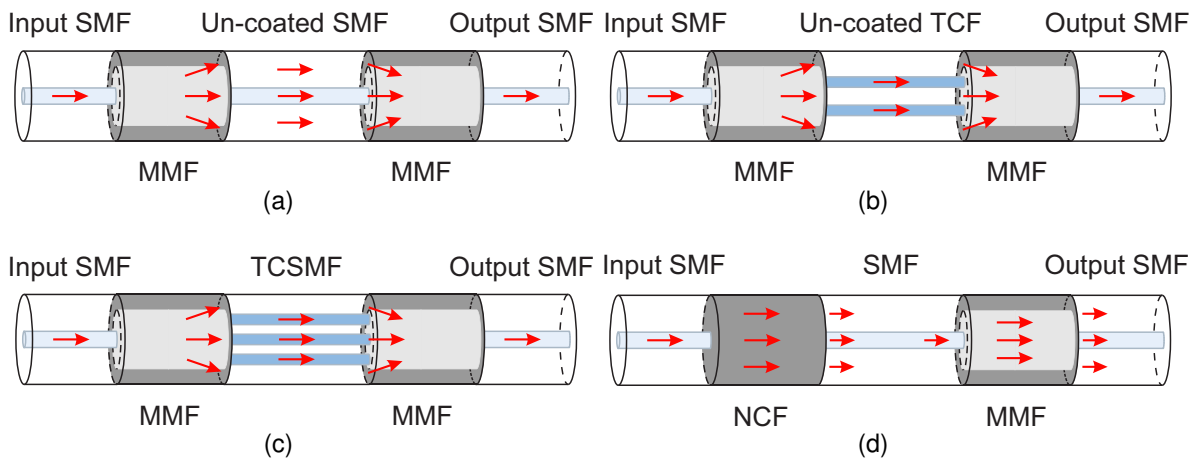


**Figure 2.8.:** Schematic of cascaded SMS fiber structure: (a) SMF-MMF-SMF-MMF-SMF; (b) SMF-MMF-TCF-MMF-SMF; (c) SMF-MMF-TCSMF-MMF-SMF; and (d) SMF-NCF-SMF-MMF-SMF.

Meanwhile, another research group, Zhengrong Tong et al. [80], investigated temperature and RI sensing as well. They used different lengths of MMF, with the long one ( $20\text{ mm}$ ) being the sensing section and the short one ( $5\text{ mm}$ ) acting as a mode coupler. The input SMS can be taken as an SMS structure, and the high-order core modes of the MMF are excited and interfere. At the same time, the MSM is taken as an MSM structure, and the interferences both happen between the excited cladding modes and the core mode. Two dips are generated by the SMS and MSM sections, respectively, which have different

spectral responses to temperature and RI to realize the simultaneous measurement. The realized sensitivities of temperature and RI could be up to a maximum of 0.1385 nm/°C and 100.97 nm/RIU, respectively.

Based on the SMSMS structure, in 2017, Yue Wu et al. [81] implemented a section of twin core fiber (TCF) to replace the un-coated SMF, as shown in Fig. 2.8(b), for simultaneous measurement of strain and curvature. Due to the large core pitch, the TCF has the uncoupled feature, and by splicing two segments of MMFs that are used as beam splitter and combiner, an in-fiber MZI can be formed. By utilizing coupled-mode theory and an equivalent refractive index model, the relation between peak wavelength and curvature is illustrated. The simultaneous measurement of curvature and strain can be realized by substituting the sensitivities to a coefficient matrix. The experimental sensitivities of temperature and strain were up to 103.35 nm/m<sup>-1</sup> and -4.01 pm/μ $\epsilon$ , respectively. Meanwhile, Yong Zhao et al. [82] studied the three-core single-mode fiber (TCSMF) for curvature measurement, as shown in Fig. 2.8(c). The TCSMF is a type of unusual optical fiber with three fiber cores separately containing one core mode, which acts as the key element for sensing. The MMFs are used for separating and combining the three core modes, as well as improving the coupling efficiency between SMF and the three cores. While light propagates through the MMF, the modal field is expanded due to the larger diameter of the MMF. Then, the light couples to the TCSMF, acting as the three core modes and other cladding modes via the modal mismatch interface. In the following, three core modes interfere with each other in the second MMF and then from the interference spectrum. According to the interference phase difference, the spectrum shifts change because of the elastic-optic effect as bending deformation is inflicted. Experiments showed that the maximum curvature sensitivity of -28.29 nm/m<sup>-1</sup> was obtained in the range of 2.79 m<sup>-1</sup> to 3.24 m<sup>-1</sup>.

As it is common to use NCF in these structures, Yaofei Chen et al. [83] proposed in 2016 a fiber sensor implemented with NCF for temperature and RI sensing, as shown in Fig. 2.8(d). It can be seen as a cascade of SMF-NCF-SMF (SNS) and SMS structures; therefore, like the principle of SMS, two distinguishable dips can be generated by appropriately choosing the lengths of NCF and MMF according to SNS and SMS, respectively. The two-parameter measurement was achieved by monitoring the wavelength shifts of these two dips in the transmission spectrum. The obtained maximum RI sensitivity was 113.66 nm/RIU, and temperature sensitivity was 9.2 pm/°C.

### 2.2.3. Discussion and Summary

Fiber sensors based on MMI have been widely used and developed into various applications, primarily based on the wavelength shifts of the selected dips (or peaks) in the transmission spectrum. Although the sensitivity is enhanced and the fabrication process is

improved, some common problems still need to be solved.

### **I. Current Challenges**

The measurement sensitivity commonly takes the linear fit of the wavelength shifts of the selected peaks (or dips) in the transmission spectrum. Thus, the excellent linearity is promising for high-resolution sensing [84], for example, bio-sensing, chemical sensing, and gas sensing. In general, when the sensitivity of a sensor increases, the resolution of the sensor also improves. However, the relationship between the wavelength shifts and measurand changes is often nonlinear, or they are only linear in limited ranges. This limit could be quite a challenge in the design of commercial fiber sensors, especially multi-parameter fiber sensors [85]. Besides, crosstalk is usually undesirable because it induces measurement errors and thus makes the measurement results unreliable, and it mainly occurs in multi-parameter sensing. For example, in the RI and temperature sensing scenario, the RI-temperature crosstalk is unavoidable because of the inherent thermo-optic and thermo-expansion effects in fibers [58, 83]. Therefore, it is necessary to measure, control, or compensate for the nonlinearity and crosstalk to calibrate the measurement sensitivities of SMS structure-based fiber sensors.

Additionally, in many cases, the measurement range is limited due to the properties and structure of the fiber sensor. For example, the temperature measurement employed with polymer optical fibers (POFs) is mainly limited to 80°C due to its material properties. The strain measurement utilizing silica optical fibers has a limit of 4000  $\mu\epsilon$  in most reported strain sensors [58]. These limits are mainly caused by the properties of different optical fibers. Some structures, such as tapered fiber sensors, could be exclusively used in a specific measurement range to obtain a boosted measurement performance. The tapered region results in lower stability and endurance, which indicates that, for instance, it can only be used in some applications with a moderate strain or temperature. Consequently, it is vital to seek solutions to overcome the limits.

### **II. Technique Outlook**

#### **1). New structures**

From the aspect of structure, the future aim is still simplification, miniaturization, and multi-parameter measurement. Firstly, simple structures can generally reduce the cost and fabrication complexity, which can broaden the application of SMS fiber sensors. Some unique SMS fiber sensors have a prominent measurement performance with their novel structures, for example, the S-tapered fiber structure [86], balloon-like fiber structure [87, 88], peanut-shaped fiber structure [89], twisted MMF based SMS structure [90, 91], SMS structure with two waist-enlarged tapers [92], and even an SMS structure with

periodically embedding short NCF sections in the MMF section [93]. However, these sensors are not desired because it is challenging to repeat the fabrication in the same condition, and the cost is relatively high. Secondly, in some cases, the sensor should be small enough, so the reduction of sensor size is still demanded. For example, the reported SMS sensors, in reflective configuration, can be theoretically half the size of the conventional SMS fiber sensors [94–96]. They indicate a new aspect of miniaturizing SMS fiber sensors. Finally, multi-parameter sensing is continually the main focus of future applications due to the unavoidable influence of the ambient environment. The structures introduced previously present some solutions and reveal that structural improvement could enhance multi-parameter sensing.

### **2). New compensation methods**

From the aspect of sensitivity compensation, generally, it refers to two methods: one is the combination of SMS structures with other different configurations; the other is thin-film coated sensing heads. In the established methods, integrating with FBGs is the most common one [97–101]. Further, other methods are also proved, like applying LPGs [102, 103] and the utility of a pair of SMS structures [104]. Besides, for coating the sensor head, which is typically the MMF segment of the SMS structure, different materials are studied like Pd/WO<sub>3</sub> film [105], Zeolite film [106], and Indium Tin Oxide (ITO) film [65]. The results show that the sensing performance of the coated fiber structure is improved compared to the conventional structure. These researches indicate that proper calibration and compensation can improve measurement sensitivity, range, and precision. However, most of these methods are primarily designed for specific applications. Thus, further research on applicable configurations that could be used in general scenarios is necessary, and the exploration of new potential coating materials is also essential for improvement.

### **3). New types of fibers**

From the aspect of innovative optic fibers, the specific properties of new fibers are mainly used. The feasibility and advantages of implementing novel fibers have been demonstrated, such as microfiber [74, 107, 108], hollow core fiber (HCF) [109, 110], twin core fiber (TCF) [81], three core single mode fiber (TCSMF) [82], hollow annular core fiber (HACF) [111], square NCF [112], thin-core fiber [113] and photonic crystal fiber (PCF) [114, 115]. Nevertheless, problems of complex fabrication, high cost, and low applicability still exist. This means further investigation of new fiber types is still required to solve the problems.

## 2.3. Multimode Fiber Imaging

Optical fibers are also prominently used in telecommunications [116] and biomedical imaging [117–121]. Optical fiber-based endoscopy has recently obtained prominent attention. The majority of these endoscopes utilize the SMF bundle, which contains thousands of SMFs. As only one mode, corresponding to one pixel of an image can be transmitted through an SMF, it is impossible to transfer images directly through an SMF. The single-mode fiber bundle circumvents this limitation, where each SMF transmits the information of one pixel in the output image. Due to the technical drawback of the fiber bundles, the separation between fiber cores, the output images are pixelated as the spacing between the cores cannot be observed. A thicker bundle with more SMFs and appropriate optics can minimize this drawback. However, a new problem appears: the diameter becomes too large and limits the accessibility of the endoscope.

Alternatively, the multimode fiber (MMF) offers another prospect due to its larger core diameter. It has an extremely high information transmission capacity as thousands of optical modes propagate simultaneously in the MMF [122]. For example, a typical 100- $\mu\text{m}$  core diameter MMF might carry around 10000 modes and could principally transfer an image with the same number of pixels [123]. Still, the waves propagating in the MMF are scrambled due to mode-mixing and modal dispersion, and the outputs are seemingly random patterns known as speckles. This effect cannot be avoided. Despite this, light transmission in the MMF remains deterministic [124]. The prospect of deterministic light propagating through MMFs has only been used due to the development of digital holography and empirical measurement of the transmission matrix (TM) based on the studies of highly turbid medium imaging. This leads to the possibility of extremely narrow and minimally invasive endoscopes.

### 2.3.1. State of the Art

In 1967, Spitz and Wertz experimentally demonstrated that the distortion introduced by modal dispersion could be eliminated by phase conjugation [44]. Several methods were then developed to understand light propagation in turbid medium. Light propagating through the turbid medium induces wavefront distortions, destroying the imaging quality [125]. However, these distortions can also be used to manipulate the wavefront to focus the light for better imaging [126, 127]. The information transmitted through the turbid medium is distorted due to the multiple scattering caused by the turbid medium. The information distortion can be eliminated if the transmission property of a turbid medium is characterized. For example, if the TM of the turbid medium is determined, the image distortion can be eliminated by the deterministic relation between the image distortion and the TM [128]. Then,

the turbid medium can become a useful optical element like the lens to improve the imaging [129]. It has been proven that turbid medium imaging can boost the resolution of the imaging system and eliminate background noise.

Optical fiber is treated as a unique turbid medium; therefore, MMF imaging is also a specific case of turbid medium imaging. With the rapid development of some techniques, like digital holography, its devices, spatial light modulator (SLM), and digital micromirror device (DMD), it is more accurate and viable to modulate the wavefront. Therefore, one MMF imaging system becomes feasible.

### I. Transmission Matrix (TM) Method

The transmission matrix is a subpart of the usual scattering matrix as introduced in [130], which describes the relationship between the incident light wave and scattered light wave in the amplitude and phase distribution. If the TM of the medium is known, the image information transmitted through the turbid medium can be reconstructed using the relationship deterministically connecting the output pattern and the TM. A brief introduction of the basic concept of turbid medium imaging is presented as the foundation for MMF imaging.

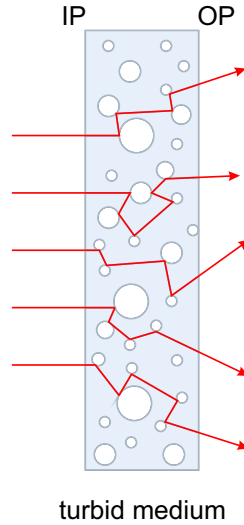


**Figure 2.9.:** Schematic of the basic SMS fiber structure.

The image information is carried by an input light wave  $E_{IP}(\theta_x, \theta_y)$  in terms of angular spectrum transmitting through a turbid medium from the input plane  $(x, y)$ , as shown in Fig. 2.9. The output light wave  $E_{OP}(\xi, \eta)$  at the output plan  $(\xi, \eta)$  is described as

$$E_{OP}(\xi, \eta) = T(\xi, \eta; x, y) E_{IP}(\theta_x, \theta_y), \quad (2.14)$$

where  $T(\xi, \eta; x, y)$  is the TM of the turbid medium. Then the original image at the input plan can be reconstructed by

$$E_{OP}(\xi, \eta)E_{IP}(\theta_x, \theta_y) = T(\xi, \eta; x, y)^{-1} E_{OP}(\xi, \eta), \quad (2.15)$$

where  $T(\xi, \eta; x, y)^{-1}$  is the inversion of the TM.

Based on this, various research has been reported for measuring the TM in an MMF imaging system. Most techniques use variations of the interferometric method to acquire the TM of the MMF. An example of a commonly used MMF imaging system is shown in Fig. 2.10. The incident laser is divided into two beams, the measuring beam and the reference beam, by a beam splitter (BS1). The CMOS captures the intensity but not the phase information of the transmitted light. The interference of the measuring and reference beams enables the phase information. However, these methods are difficult to implement as the system is sophisticated. A reference-free system would be tremendously helpful.

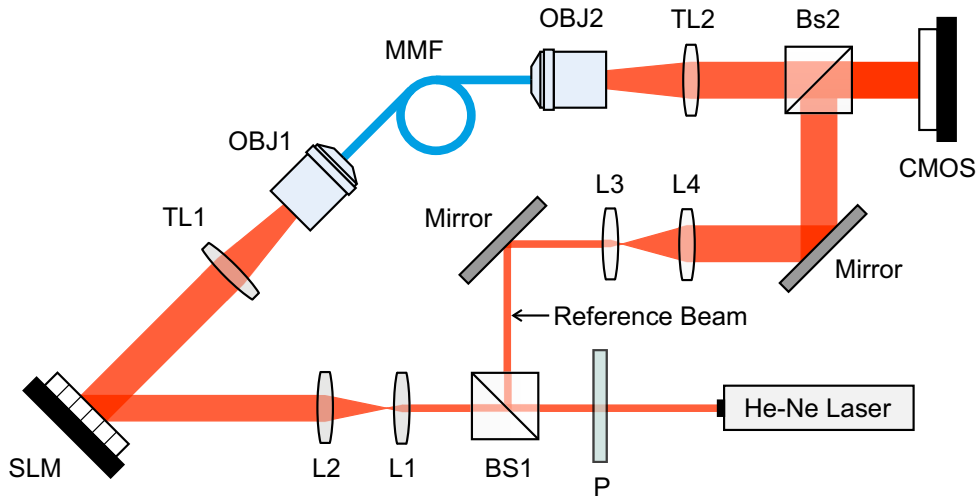


**Figure 2.10.:** Example of a commonly used MMF imaging system. P, polarizer; BS1, beam splitter; L1, lens; L2, lens; TL1, tube lens; OBJ1, objective lens; MMF, multimode fiber; OBJ2, objective lens; TL2, tube lens; BS2, beam splitter; L3, lens; L4, lens.

In 2012, a concept of scanner-free and wide-field endoscopic imaging using an MMF was proposed and investigated [131]. The measured TM of an MMF was used to reverse the on-the-way-out distortion of the detected light. With the implementation of the speckle imaging and turbid medium imaging method, seeing an object through an MMF was realized. This proposed technique utilized a reference beam and also suffered from the bending of the MMF.

New methods were developed based on numerical modeling to measure and analyze the TMs of real-life MMFs [124]. The results also showed which modes are the most vulnerable

or immune to fiber deformations. Furthermore, the TM changes induced by deformation, e.g., bending, could be tuned by selecting the refractive index and Poisson's ratio. The imaging through the MMF was realized without acquiring the TM experimentally.

In 2018, a reference-less optical system was proposed combined with complex semidefinite programming for measuring the TM of the MMF by mode control [132]. The semidefinite program using convex optimization, together with an SLM, was implemented to generate the TM of the optical system by using intensity-only measurement. As no reference beam was needed, no interferometric measurements were required, and therefore, the system was simple yet powerful. The concept of acquiring the TM without a reference beam, as shown in Fig.2.11, is a meaningful improvement for endoscopic imaging.

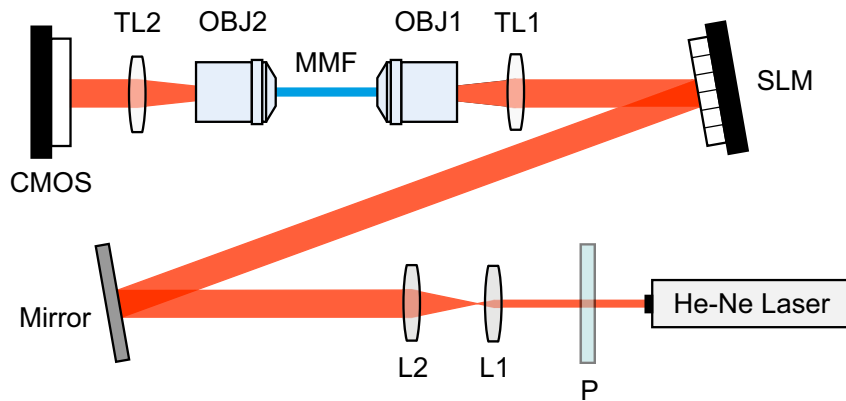


**Figure 2.11.:** Concept of a reference-less MMF imaging system. P, polarizer; L1, lens; L2, lens; SLM, spatial light modulator; TL1, tube lens; OBJ1, objective lens; MMF, multimode fiber; OBJ2, objective lens; TL2, tube lens.

Meanwhile, another method for acquiring the complete TM of an MMF in a reference-less system with phase retrieval techniques was studied [133]. Due to the high speed of the DMD, a distributed or parallel calculation can be achieved to accelerate the data acquisition. The obtained TM has demonstrated a strong predictive ability for diffraction-limited imaging and light focusing.

Later, in 2020, with the reference-less system, a method was introduced based on an assumption of a pseudo-linearity between the input and output light intensity distributions of MMF [134]. This method utilized a real-value intensity transmission matrix, which connects the input and output light intensities. The input images could be retrieved from the intensity values of the output speckles. This method realized a high-speed image retrieval within 0.01 s for 1024-pixel images.

## II. Machine Learning Method

With the development of computation power, machine learning methods are booming and dramatically improving image classification and object recognition. Machine learning includes supervised learning, unsupervised learning, and semi-supervised learning. These categories are classified according to the tasks, input data, and output data. The parameters of the network are optimized during the labeled training process, where the model learns the training dataset (including input and correct output). The algorithm evaluates its accuracy through the loss function, adjusting until the error has been minimized sufficiently. Unsupervised learning is commonly used for finding the characteristics of unlabeled input data. The models are used for three main tasks: clustering, association, and dimensionality reduction. Semi-supervised learning is a hybrid technique between supervised and unsupervised learning, which utilizes a limited number of labeled data and a large amount of unlabeled data. According to the availability of the dataset, the most suitable machine learning method can be chosen.

Deep learning, as a subfield of machine learning, automates much of the feature extraction of the process, eliminating some of the human intervention. Neural networks, specifically artificial neural networks (ANNs), are the backbone of deep learning methods, as they determine the number of node layers, or depth, of neural networks that distinguish a single neural network from a deep learning algorithm, which must have more than three layers.

Recently, various machine learning methods have been applied to MMF imaging to address the limitations that prohibit the efficiency of information transmitted through MMFs, like fiber length and environmental instability. The changes in the output speckle patterns and the TM of the MMFs are sensitive to ambient perturbations, such as thermal and mechanical perturbations, which affect machine learning methods at a low level. With a similar setup, as shown in Fig. 2.11, the complexity of the time-consuming measurement of the TM of the MMF can be significantly reduced.

Navid Borhani et. al [135] used deep neural networks (DNNs) to classify and reconstruct the input images (handwritten digits from the MNIST database [136]) from the intensity of the output speckle patterns propagated through an MMF. First, a "U-Net" type [137] convolutional neural network (CNN) with 14 hidden layers was used to reconstruct the SLM input images from the output speckle patterns. Followed by the use of a "Visual geometry group (VGG)" type CNN [138] was used to classify the distal speckle patterns and reconstructed SLM images. The results showed that the classification performance was enhanced with these two steps. The influence of fiber length up to 1 km was also investigated. The measured classification accuracy was 96.8% for 10-m-long fiber but dropped to 69.9% for 1-km-long fiber.

A CNN-architecture SpeckleNet was proposed and studied for object classification trans-

mitted through an MMF [139]. Face images (from the Labeled Face in the Wild database [140]) and nonface images (from the Corel5k database) were tested, and the classification accuracy reached 96%.

In 2019, Pengfei Fan used deep learning to address the geometric shape changes of the MMF, i.e., bending [141]. First, the DNN was trained with input and output pattern pairs collected with a non-bent MMF. Then, the same data acquisition was performed with different geometric states of the MMF, named G1, G2, and G3. The DNNs reconstruct the input pattern excellently when trained by the data under the same MMF geometric state. However, it could not predict the input pattern at other MMF geometric states. When the DNN was trained by a mix of data collected at G1, G2, and G3, it could predict the input patterns for different MMF geometric states. Further, the appropriately trained CNN was tested to predict the input patterns at a continuously changing geometric state. The results showed that a DNN trained with possible variations might overcome the high variability and randomness of the MMF in an imaging system.

Later, in 2020, a pre-trained autoencoder, including an encoder and decoder, was proposed for image reconstruction with an MMF imaging system. First, the network was pre-trained with the complete data (Fashion-MNIST [142]), excluding the images that will be transmitted through the MMF, to initialize the parameters. Then, the images and related output speckle patterns were used to train the network with the parameters initialized by pre-training. The reconstructed results showed a higher accuracy compared to using U-Net and fast convergence speed. This network has the potential to reconstruct more complex images, e.g., natural images.

Meanwhile, a method based on principal component analysis (PCA) for establishing the inverse TM of the MMF was proposed. The idea of PCA was about the dimension reduction of a dataset, which preserved as much statistical information as possible [143]. Combined with a support vector machine (SVM), the proposed method reconstructed and recorded grayscale images of natural scene images at high resolution and high frame rates with few training samples. The shortening of training time and low computational power requirement made this method feasible for MMF endoscopic imaging. However, this method is limited to the class of natural images, and the background noise influence still needs to be tackled.

A single hidden layer dense neural network (SHL-DNN) was proposed and compared with commonly used CNNs on MNIST and Fashion-MNIST datasets, in 2021 [144]. The SHL-DNN is one of the simplest dense neural network architectures. The comparison of reconstruction accuracy of SHL-DNN and U-Net showed that the SHL-DNN could achieve a similarly high reconstructed image fidelity, as Structural Similarity Index Measure (SSIM) 0.775 for SHL-DNN and 0.767 for U-Net. However, SHL-DNN required a much shorter training time, 16 minutes for SHL-DNN and 3.5 hours for U-Net and less network complexity. Further, a "VGG-type" neural network was compared, which did not show improved

performance over the SHL-DNN. Comparatively, when the images vary significantly in the training dataset, the proposed neural network performs poorly on the image reconstruction.

Recently, a new dual-function MMF system for simultaneous illumination and imaging was proposed [145]. The illumination light and images were transmitted through the same MMF, which reduced the size and complexity of the MMF imaging system. At the same time, a new deep learning-based encoder-decoder network containing full-connected (FC) layers was designed for image reconstruction. Five methods, including encoder-decoder network, FC-encoder-decoder network, encoder-FC-decoder network, encoder-decoder-FC network, and SHL-DNN network, were compared with three datasets, like Fashion-MNIST, Quickdraw [146], and SIPaKMeD [147]. The experimental results show that the reconstruction accuracy performed by the FC-encoder-decoder network is significantly boosted with the least training time. However, the imaging resolution still needs to be improved with new techniques.

An artificial intelligence-enhanced orbital angular momentum (OAM) data transmission system was developed, and an approach using multiple parallel neural networks was proposed, which combined a deep CNN with OAM techniques [148]. The image transmission was performed through a 1-km-long MMF using single networks and parallel networks, and the results indicated the parallel network had achieved better performance with reduced required training data. It can lower the requirement for computation power and hardware. Further, the quality of reconstructed natural images was drastically improved, with model accuracy increased from 78.17% (single networks) to 96.26% (parallel networks).

To further reduce the required training dataset, an attention-mechanism-assisted U\_Net model (AM\_U\_Net) with the structural dissimilarity index merit (DSSIM) loss function was proposed for image reconstructions transmitted through MMF [149]. The DSSIM loss function has been verified to learn the nonlinear mapping relationship between the input images and output speckles more effectively than traditional loss functions, e.g., the mean squared error (MSE) loss function. Besides, the attention mechanism enables the network to extract more useful information from the images. Therefore, it was possible to train the network with an ultra-small dataset obtained using a polarization system, where speckle images are acquired at two linear polarization states. This AM\_U\_Net was tested at MMF lengths from 1.2 m to 3.0 m and laser intensities in the range of 1.51 mW to 18.3 mW. The results indicated that it performed excellently for distorted output speckle images due to the varying MMF length or laser intensity. Furthermore, the bimodal fusion method utilized the S- and P-polarized speckles with orthogonal polarization vectors was proposed to increase the classification accuracy of the reconstructed images up to 98.44%, which is much higher than non-polarized (80%), P-polarized (87.5%), and S-polarized speckles (90%).

A significant improvement in optical fiber-based endoscopic imaging at high speeds was made by Liu et al. [150]. The proposed MMF imaging was achieved by transferring two-

dimensional spatial information into one-dimensional temporal pulsed streams. The neural network was trained to reconstruct images from the temporal waveforms instead of the spatial waveforms. When a laser pulse with a temporal duration of less than the delay difference between different modes is used, the phase delays, at the output of the MMF, can be split into many isolated subpulses in the time domain. The nonlinear effects in the MMF can be ignored, and then the temporal distribution of the isolated subpulses depends on the spatial distribution (images) at the input of the MMF. Therefore, the spatial information of objects can be encoded into the time waveforms of the output pulses. This technique utilizes the advantages of the time-stretching method while still having a real-time image acquisition with a frame rate of over 15 Mfps. This high-speed proof-of-concept system contributes to the practical use of optical fiber-based endoscopy in vivo applications.

### 2.3.2. Discussion and Summary

Multimode fiber imaging is developed based on scattering medium imaging. Many conventional methods, like the TM method, have been investigated to reconstruct the input images from the output speckle patterns propagated along the MMF. However, the MMF imaging system is usually complicated, and the TM measurement is time-consuming, which limits the implementation of the MMF imaging into the endoscopes.

The blossom of machine learning techniques accelerates the improvement of MMF imaging in endoscopic applications. Various machine learning-based methods have been proposed and verified that reconstructing the input images from the output speckle patterns transmitted through the MMFs is feasible, and the reconstruction accuracy is significantly enhanced. The machine learning methods can also help to overcome the typical limitations of the MMF imaging system, such as sensitivity to the ambient perturbations, the fiber length, and the complexity of the setup. Still, many limitations need to be solved to bring MMF imaging to the next level in terms of practical usage.

The MMF imaging suffers from the deformation of the MMF, including thermal perturbations, laser wavelength drifts, and geometric changes. A sophisticated optical setup contributes to overcoming some limits while increasing the imaging system's complexity. Besides, implementing machine learning methods improves imaging quality and image reconstruction accuracy but is limited by the types of images used. For example, the reconstruction of natural images is still not well established [123]. The reconstruction accuracy and the image resolution need to be improved. For more complicated images, the combination of a complex optical setup and a more powerful neural network may boost the feasibility of image reconstruction. However, this solution needs to be revised, and a trade-off between complexity and accuracy needs to be decided. First, the MMF imaging system needs to be optimized to reduce the number of optical components to be compact and

flexible. As MMF-based endoscopic imaging demands the flexibility of the MMF, the deformation of the MMF is inevitable. Therefore, the neural network needs to be tuned to fit the imaging system, which should be adjusted to the deformation of the MMF. Further, the neural network needs to be investigated for thermal perturbation, as the MMF is sensitive to temperature changes. The image reconstruction accuracy and the reconstructed image resolution are the essential factors for MMF-based endoscopic imaging.



## 3. Characterization of Standard Multimode Fibers

The theoretical analysis presented in Chapter 2 indicates that the optical power in the output SMF of an SMS structure is affected by changes in the propagation constants, i.e., the NA, core diameter, and the length of the MMF. For simplicity, this theory has some assumptions, such as that the SMFs and the MMF are perfectly aligned. [151] Therefore, this theoretical analysis cannot be simply applied to practical scenarios as many other modes need to be simultaneously considered. [152]. In this chapter, a comprehensive characterization of the standard MMF-based SMS structure for temperature and strain sensing is performed to investigate the sensitivity dependences on the core diameter, the NA, and the length of the MMF. The detailed study also shows that the strain sensitivity is relatively small and thus has the potential to develop strain-insensitive temperature sensors with standard MMFs instead of specialty fibers, such as small-core photosensitive fiber [153] and seven-core fiber [154]. According to this study, the strain-insensitive temperature fiber sensor based on MMI implementing standard MMF is verified experimentally.

### 3.1. Principles

Equation 2.5 indicates that the optical power in the output SMF of an SMS structure is affected by ambient physical parameters, including temperature and strain. Due to the inherent thermal expansion and thermo-optic effects of the material of the MMF, the spectral characteristics of an SMS structure are temperature-dependent, as the core diameter, length, and refractive index of the core of the MMF are all functions of the applied temperature change. The relative wavelength shift ( $\Delta\lambda/\lambda$ ) against temperature can be theoretically expressed as [155]

$$\frac{\Delta\lambda}{\lambda} = (\alpha_1 + \xi) \Delta T, \quad (3.1)$$

where  $\alpha_1$  and  $\xi$  are the coefficients of the thermal expansion and the normalized thermo-optic coefficient of the MMF material, respectively. It indicates that the spectral shift and

temperature changes are linearly correlated, and it is determined by the properties of the MMF material.

The situation is almost the same in strain. When applying strain to the SMS structure, a spectral shift will occur due to the changes in fiber dimensions and the photoelastic effect. At a constant temperature, the strain-induced spectral shift can be given as [155, 156]

$$\frac{\Delta\lambda}{\lambda} = \left[ \frac{\Delta n_{co}}{n_{co}} + 2 \frac{\Delta a}{a} - \frac{\Delta L}{L} \right]_T, \quad (3.2)$$

where  $n_{co}$  is the refractive index of the MMF core,  $a$  is the core radius, and  $\Delta$  indicates the changes in corresponding parameters. Assuming that only an axial strain is applied to the fiber, then it can be expressed as

$$\frac{\Delta\lambda}{\lambda} = -(1 + 2\nu + p_e) \varepsilon, \quad (3.3)$$

where  $\nu$  is the Poisson ratio of the fiber and  $p_e$  is the effective strain-optic coefficient. It clearly shows that an axial strain leads to a spectral shift and is related to the properties of the MMF. Here, we simply calculate strain as [157]

$$\Delta\varepsilon = \frac{\Delta L}{L}. \quad (3.4)$$

The theoretical analysis [158] also proves that these physical changes (temperature and strain) can be quantitatively evaluated by measuring the shift in either power or the spectral location of the dips (or peaks), which are related to the core diameter, NA, and the length of the MMF. However, it is difficult to analyze or simulate the performance of the SMS fiber sensors by simply applying these equations, as an enormous number of modes need to be considered. This promotes the need for the experimental study of its characteristics for the design guidelines of SMS structures.

Figure 3.1 schematically shows the experimental setup for temperature and strain measurement. Note that all the MMFs are unjacketed and uncoated. The MMF section is heated and clamped on two precision translation stages, which can apply varying axial tensile stress on the sample. Both ends of the MMF are connected to the SMFs. The other end of the input SMF is connected to a broadband light source (BLS, central wavelength: 1550 nm), while the other end of the output SMF is connected to an OSA, which detects the changes in the light spectrum.

The temperature sensitivity is first measured without strain applied during the experiment. Due to the different operating temperatures of the MMFs, the temperature range is chosen from 30 to 70°C in steps of 5°C. Then the strain sensitivity is measured at room temperature ~20°C. The strain range is 0 to 1750  $\mu\varepsilon$  according to the available devices in steps of 250  $\mu\varepsilon$ .

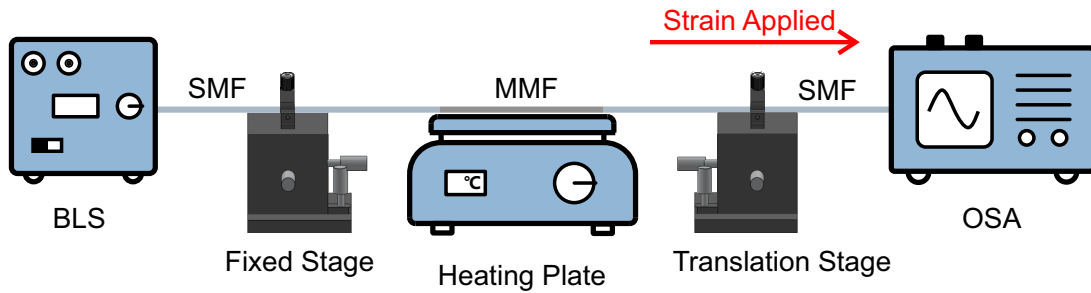


**Figure 3.1.:** Schematic diagram of the experimental setup for temperature and strain measurement. BLS, broadband light source; SMF, single-mode fiber; MMF, multimode fiber; OSA, optical spectrum analyzer.

## 3.2. Comprehensive Characterization

### 3.2.1. Core Diameter Dependence

The commonly used standard MMF has a 0.22 NA silica core with three different core diameters: 50  $\mu\text{m}$  (FG050LGA, Thorlabs), 105  $\mu\text{m}$  (FG105LGA, Thorlabs), and 200  $\mu\text{m}$  (FG200LGA, Thorlabs). Therefore, these three MMFs are used for investigating the core diameter dependence with a length of 8 cm, which is determined based on the length dependence in Section 3.2.3.

The temperature sensitivities of the MMF with different core diameters are illustrated in Fig. 3.2. The measured dependences of the spectral dip on temperature are shown in Fig. 3.2(a), 3.2(b), and 3.2(c) for 50- $\mu\text{m}$ , 105- $\mu\text{m}$ , and 200- $\mu\text{m}$  core diameters, respectively. The spectral dips shift to longer wavelengths when the temperature increases. The resulting wavelength shifts versus temperature are plotted and linearly fitted in Fig. 3.2(d), 3.2(e), and 3.2(f). The dependences are almost linear, with a coefficient of 8.18  $\text{pm}/^\circ\text{C}$ , 8.78  $\text{pm}/^\circ\text{C}$ , and 11.41  $\text{pm}/^\circ\text{C}$ , respectively.

In the same way, the strain measurement is presented in Fig. 3.3. With the increasing strain, the spectral dip shifts to shorter wavelengths of 50- $\mu\text{m}$  and 105- $\mu\text{m}$  but to longer wavelengths of 200- $\mu\text{m}$  core diameter, as shown in Fig. 3.3(a), 3.3(b), and 3.3(c). The corresponding dip wavelength dependence on strain leads to a coefficient of  $-2.11 \text{ pm}/\mu\epsilon$ ,  $-1.05 \text{ pm}/\mu\epsilon$ , and  $0.23 \text{ pm}/\mu\epsilon$ , as displayed in Fig. 3.3(d), 3.3(e), and 3.3(f).

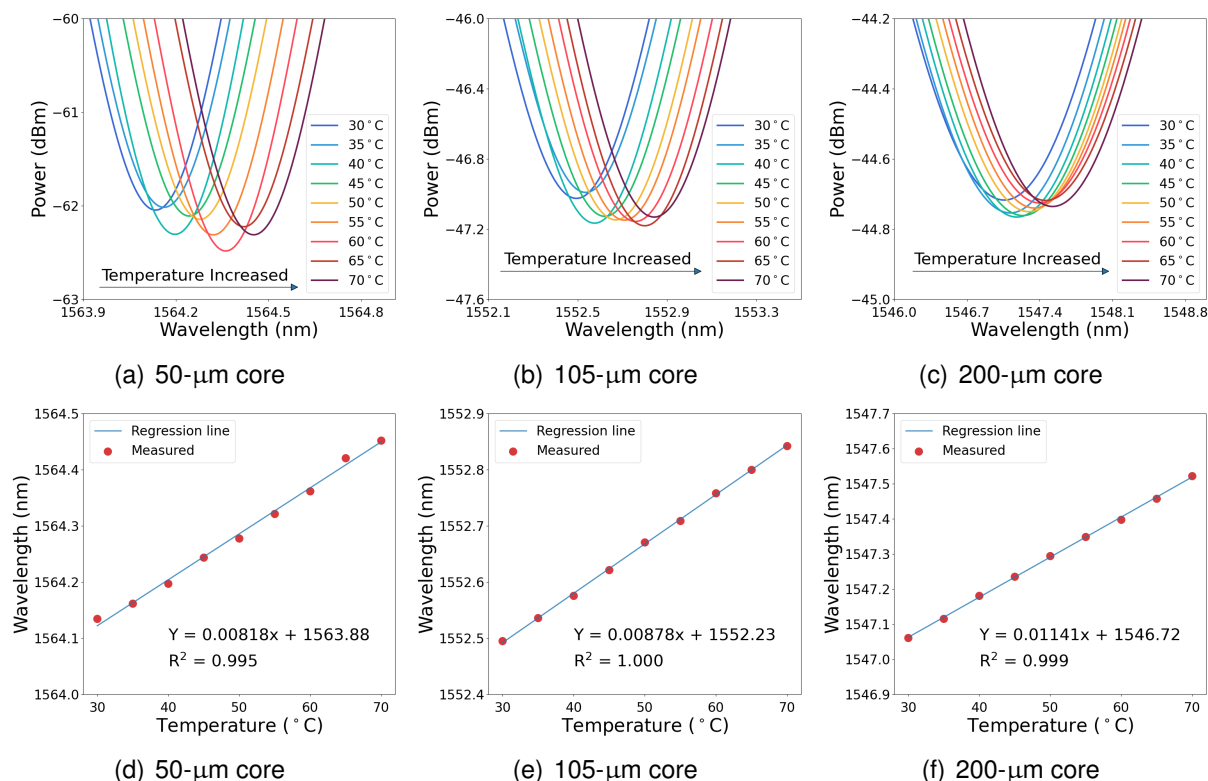


**Figure 3.2.:** Temperature measurement results for the MMF with different core diameters. Measured spectral dependence on temperature: (a) 50- $\mu\text{m}$  core diameter, (b) 105- $\mu\text{m}$  core diameter, and (c) 200- $\mu\text{m}$  core diameter. Spectral dip shifts as a function of temperature: (d) 50- $\mu\text{m}$  core diameter, (e) 105- $\mu\text{m}$  core diameter, and (f) 200- $\mu\text{m}$  core diameter.

**Table 3.1.:** Temperature and strain sensitivities measured with different core diameters of the MMF.

Fiber Info.	Dependence	Core Diameter	Sensitivity	$R^2$
0.22 NA Length = 8 cm	Temperature	50 $\mu\text{m}$	8.18 $\text{pm}/^\circ\text{C}$	0.995
		105 $\mu\text{m}$	8.78 $\text{pm}/^\circ\text{C}$	1.000
		200 $\mu\text{m}$	11.41 $\text{pm}/^\circ\text{C}$	0.999
	Strain	50 $\mu\text{m}$	-2.11 $\text{pm}/\mu\epsilon$	0.980
		105 $\mu\text{m}$	-1.05 $\text{pm}/\mu\epsilon$	0.981
		200 $\mu\text{m}$	0.23 $\text{pm}/\mu\epsilon$	0.984

The obtained temperature and strain sensitivities are summarized in Table 3.1. The linear

regression coefficients ( $R^2$ ) are in the range of 0.980 to 1.000 for both temperature and strain sensing, which indicate high linearity. This table points out that a larger core diameter of the MMF leads to higher temperature sensitivity but lower strain sensitivity (absolute values). The strain sensitivity dependence on the core diameter also implies that zero sensitivity can be realized at a specific core diameter.

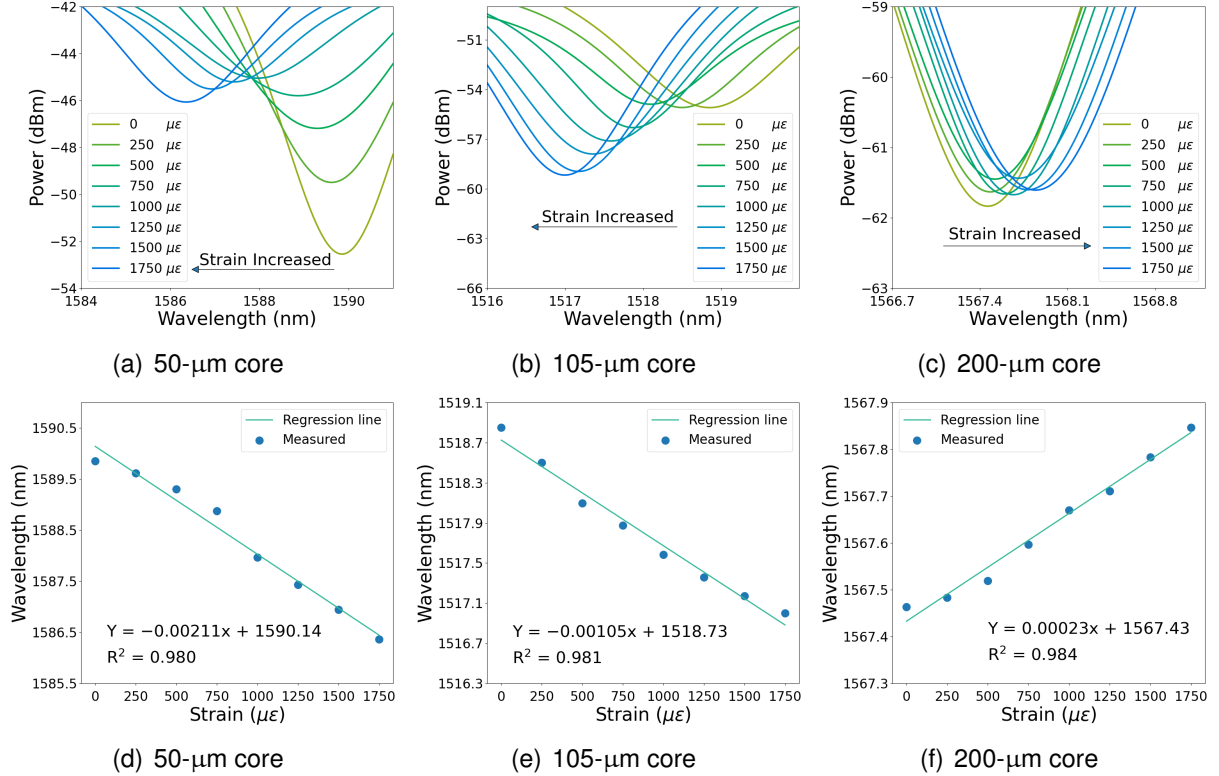


**Figure 3.3.:** Strain measurement results for the MMF with different core diameters. Measured spectral dependence on strain: (a) 50- $\mu\text{m}$  core diameter, (c) 105- $\mu\text{m}$  core diameter, and (e) 200- $\mu\text{m}$  core diameter. Dip wavelength versus strain: (b) 50- $\mu\text{m}$  core diameter, (d) 105- $\mu\text{m}$  core diameter, and (f) 200- $\mu\text{m}$  core diameter.

### 3.2.2. Numerical Aperture Dependence

The MMFs with a 200- $\mu\text{m}$  core diameter have variable numerical apertures: 0.22 NA (FG200LEA, Thorlabs), 0.39 NA (FT200EMT, Thorlabs), and 0.5 NA (FP200ERT, Thorlabs). In this experiment, due to the cladding materials of the MMFs, butt-coupling [159] is used to connect the MMF to the SMFs. Due to the configuration of the fiber sensor, a 20-cm-long MMF section is used for the measurement.

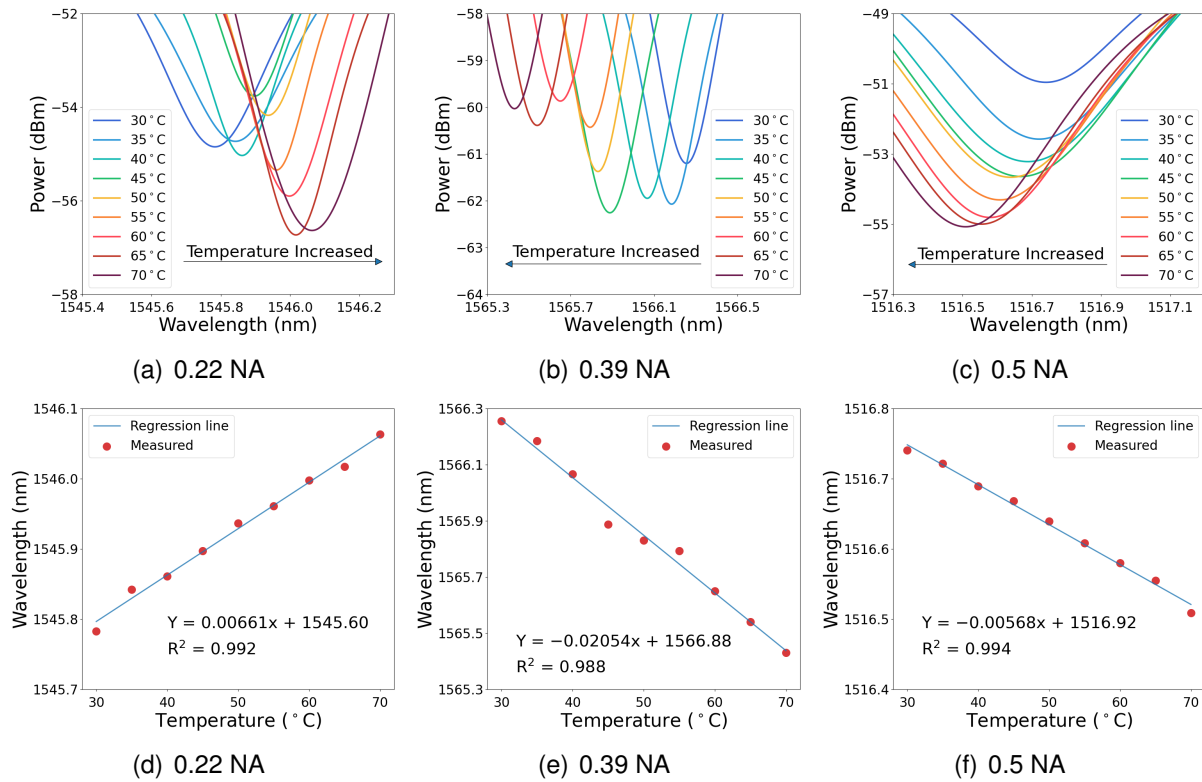


**Figure 3.4.:** Temperature measurement results for the MMF with different NAs. Measured spectral dependence on temperature: (a) 0.22 NA, (b) 0.39 NA, and (c) 0.5 NA. Spectral dip shifts as a function of temperature: (d) 0.22 NA, (e) 0.39 NA, and (f) 0.5 NA.

**Table 3.2.:** Temperature and strain sensitivities measured with different NAs of the MMF.

Fiber Info.	Dependence	NA	Sensitivity	$R^2$
Core Diameter = 200 $\mu\text{m}$ Length = 20 cm	Temperature	0.22	6.61 $\text{pm}/^\circ\text{C}$	0.992
		0.39	-20.54 $\text{pm}/^\circ\text{C}$	0.988
		0.5	-5.68 $\text{pm}/^\circ\text{C}$	0.994
	Strain	0.22	-0.087 $\text{pm}/\mu\epsilon$	0.992
		0.39	-0.091 $\text{pm}/\mu\epsilon$	0.983
		0.5	-0.120 $\text{pm}/\mu\epsilon$	0.978

The temperature sensitivity of the MMF with different NAs is demonstrated in Fig. 3.4. Figure 3.4(a) shows a clear redshift of the wavelength dips with the temperature increases for the MMF with 0.22 NA, while Fig. 3.4(b) and Fig. 3.4(c) show a blueshift for the MMF with

0.39 and 0.5 NA, respectively. Figure 3.4(d), 3.4(e), and 3.4(f) present the corresponding measured temperature sensitivities of 6.61 pm/°C, -20.54 pm/°C, and -5.68 pm/°C.

The strain sensitivity of the MMF with different NAs is illustrated in Fig. 3.5. The clear blueshifts of the wavelength dips are distinguished with strain applying for the MMF with 0.22, 0.39, and 0.5 NA, as shown in Fig. 3.5(a), 3.5(b), and 3.5(c). The related measured strain sensitivities are -0.087 pm/μ $\epsilon$ , -0.091 pm/μ $\epsilon$ , and -0.120 pm/μ $\epsilon$ , as plotted in Fig. 3.5(d), 3.5(e), and 3.5(f).

The obtained temperature and strain dependences on the NA of the MMF are summarized in Table 3.2, in which the  $R^2$  values also illustrate high linearity. It expresses that the temperature sensitivity is independent of the NA of the MMF, while the absolute value of strain sensitivity increases with the larger NA.

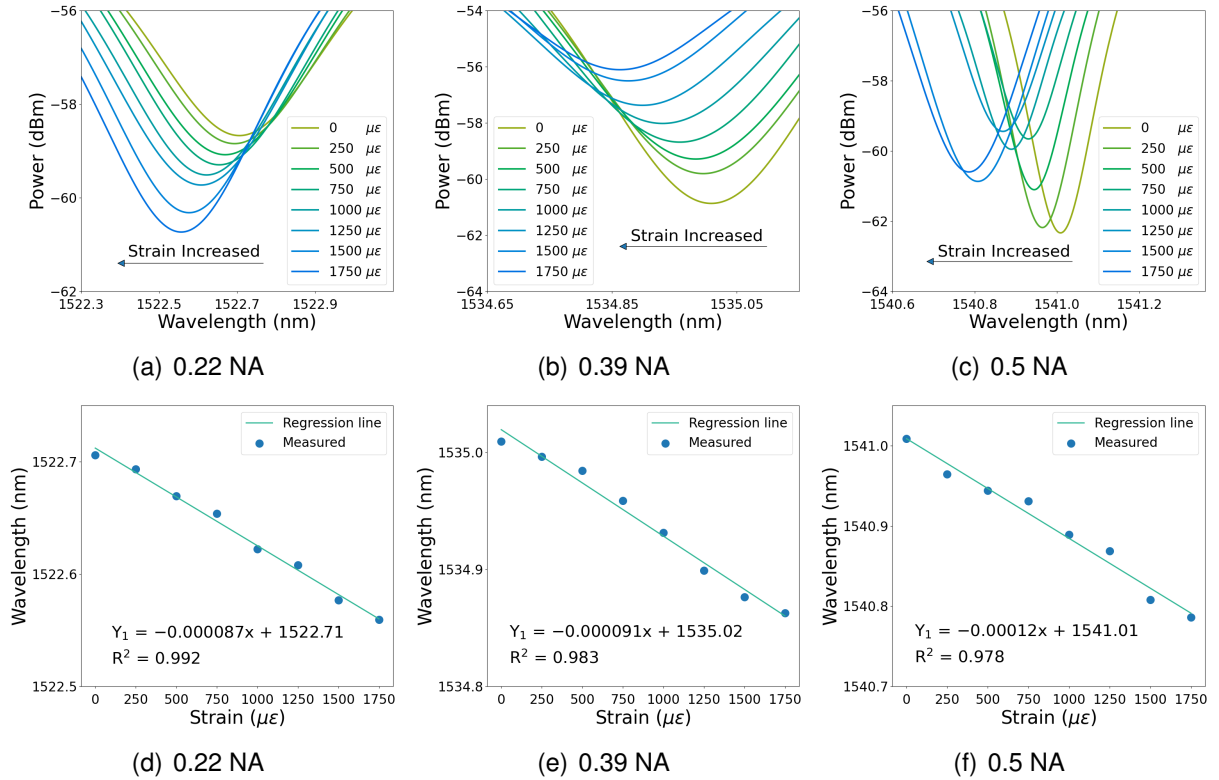


**Figure 3.5.:** Strain measurement results for the MMF with different NAs. Measured spectral dependence on strain: (a) 0.22 NA, (b) 0.39 NA, and (c) 0.5 NA. Dip wavelength versus strain: (d) 0.22 NA, (e) 0.39 NA, and (f) 0.5 NA.

### 3.2.3. Length Dependence

As previously described, the principle of the SMS fiber sensor has some assumptions. It leads to a discussion of whether the temperature and strain sensitivities are dependent on the MMF lengths. [160] As the scope of this work is to investigate the characteristics of standard MMFs, the 50- $\mu\text{m}$  core diameter MMF with a 0.22 NA is used. Figure 3.6 shows the temperature sensing results. The spectral dip exhibits a redshift in the wavelength domain when the temperature increases for 4-cm-long, 8-cm-long, and 12-cm-long MMFs, as shown in Fig. 3.6(b-d) and the resulting wavelength shift of the dip against the temperature variation is plotted and fitted in Fig. 3.7(b-d). The fitting results indicate that the relevant temperature sensitivities are determined to be 8.20  $\text{pm}/^\circ\text{C}$ , 7.98  $\text{pm}/^\circ\text{C}$ , and 7.31  $\text{pm}/^\circ\text{C}$ .

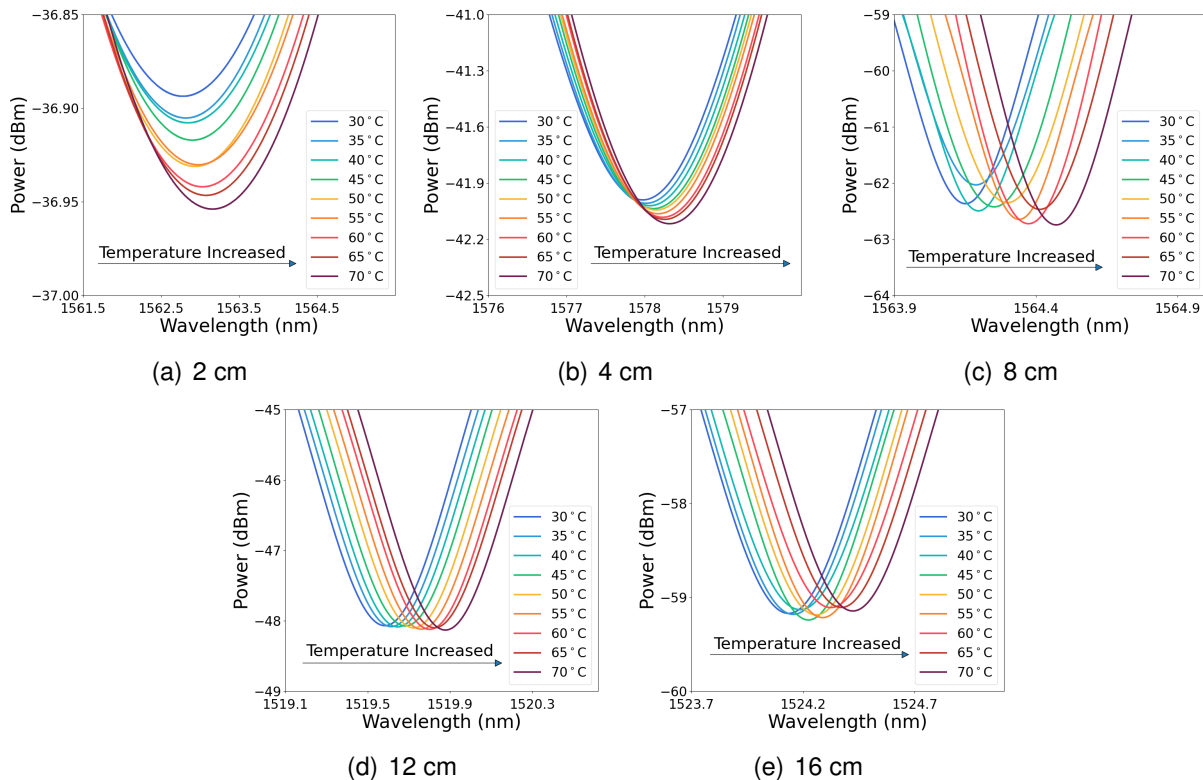


**Figure 3.6.:** Temperature measurement results for the MMF with different lengths. Measured spectral dependence on temperature: (a) 2 cm, (b) 4 cm, (c) 8 cm, (d) 12 cm, and (e) 16 cm.

The strain sensing results are presented in Fig. 3.8. The spectral dip has a blueshift with the strain applying for the 4-cm-long and 8-cm-long MMF but has a redshift for the 12-cm-long MMF, as shown in Fig. 3.8(a-c). The related resulting wavelength shift of the dip against the increasing strain is plotted and fitted in Fig. 3.8(d-f), and the measured strain sensitivities are  $-0.41 \text{ pm}/\mu\epsilon$ ,  $-2.11 \text{ pm}/\mu\epsilon$ , and  $0.30 \text{ pm}/\mu\epsilon$ .

The obtained temperature and strain dependences on the lengths of MMFs are summarized in Table 3.3. The temperature and strain dependences are both verified with the MMF length of 4 cm, 8 cm, and 12 cm. The results show that the strain sensitivity is independent of the MMF length, while the temperature sensitivity decreases with increasing MMF length. Based on the results, two more MMF lengths are studied to further enhance the results. Figure 3.6(a, e) shows that the spectral dip exhibits a redshift as well for the 2-cm-long and the 16-cm-long MMF, respectively. The obtained temperature sensitivities are  $9.17 \text{ pm}/^\circ\text{C}$  and  $7.10 \text{ pm}/^\circ\text{C}$ , as shown in Fig. 3.7(a, e), which strengthens the conclusion that the increasing length of MMF results in lower temperature sensitivity. Note that, besides the applied temperature change and strain, the core diameter and length of the MMF are also slightly changed due to the thermal expansion, thermo-optic effects, and photoelastic effects. The temperature increase leads to the core diameter expansion and length increasing, contributing to the sensitivity, whereas axial strain increases the length but reduces the core diameter, which also influences the sensitivity. This difference may partially explain the significant difference between temperature and strain dependences.

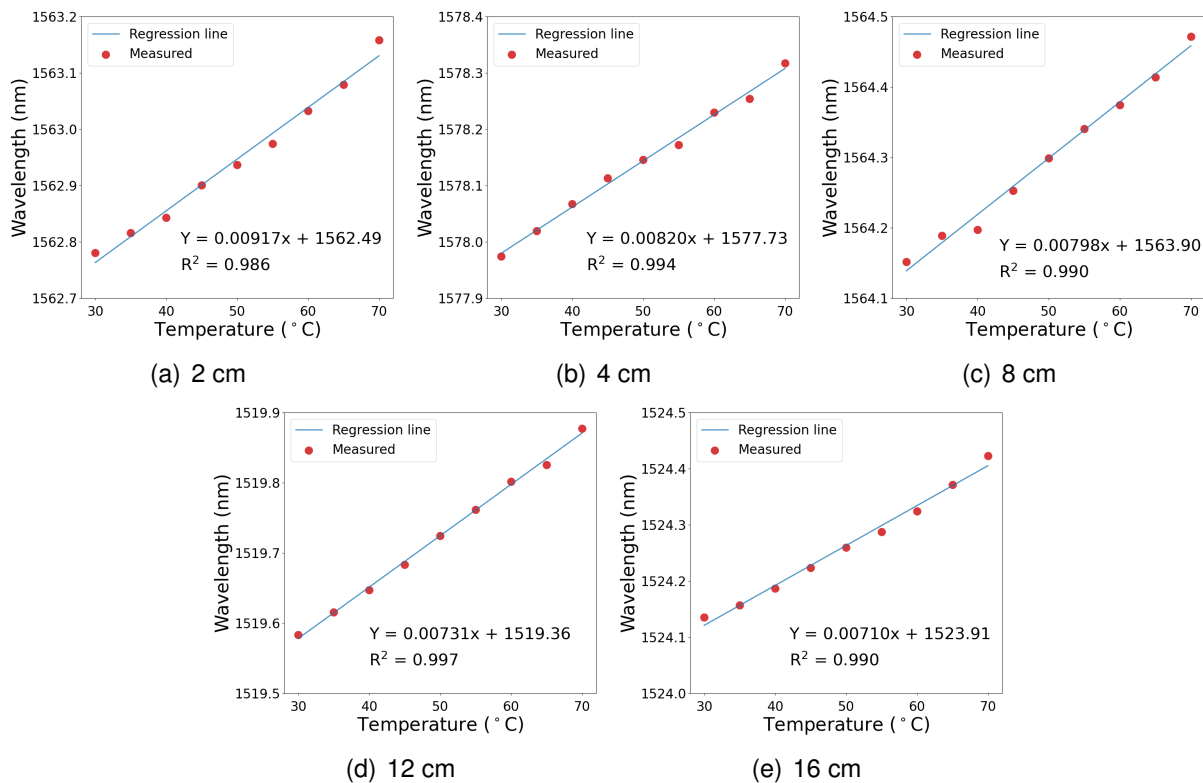


**Figure 3.7.:** Temperature measurement results for the MMF with different lengths. Spectral dip shifts as a function of temperature: (a) 2 cm, (b) 4 cm, (c) 8 cm, (d) 12 cm, and (e) 16 cm.

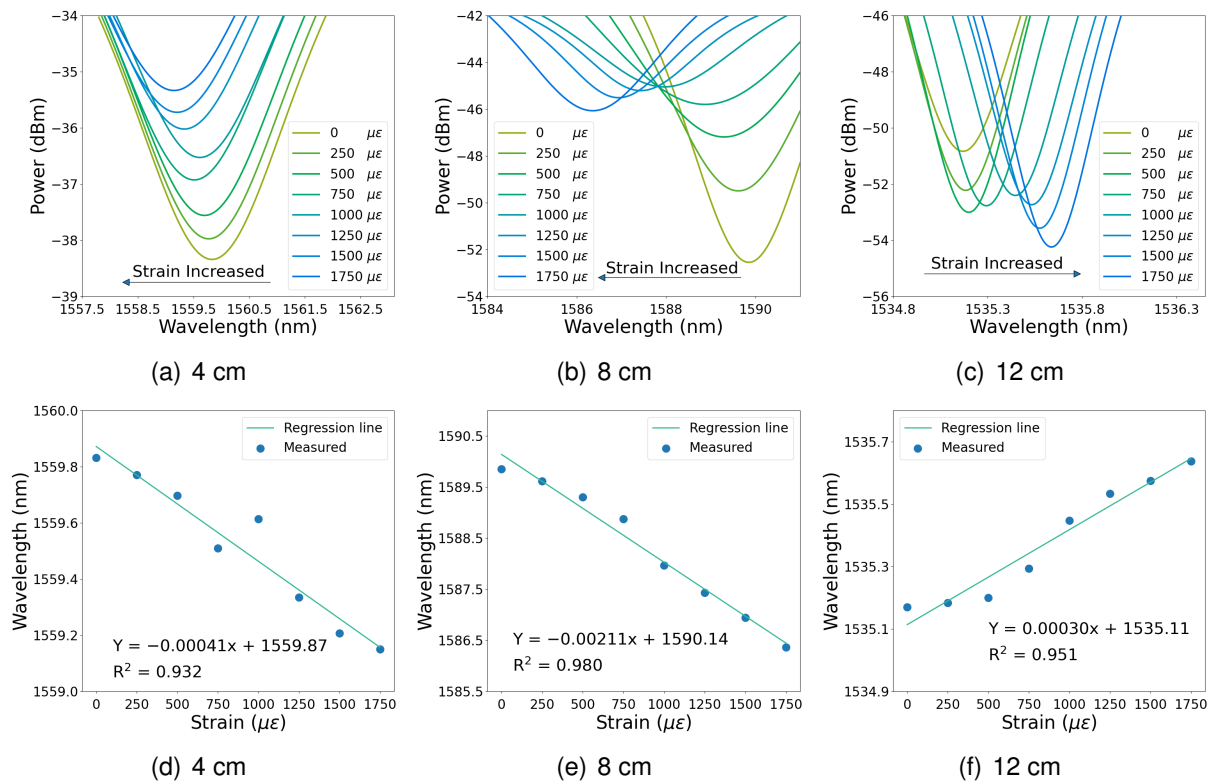


**Figure 3.8.:** Strain measurement results for the MMF with different lengths. Measured spectral dependence on strain: (a) 4 cm, (b) 8 cm, and (c) 12 cm. Dip wavelength versus strain: (d) 4 cm, (e) 8 cm, and (f) 12 cm.

**Table 3.3.:** Temperature and strain sensitivities measured with different lengths of the MMF.

Fiber Info.	Dependence	Length	Sensitivity	$R^2$
Core Diameter = 50 $\mu\text{m}$ NA = 0.22	Temperature	2 cm	9.17 $\text{pm}/^\circ\text{C}$	0.986
		4 cm	8.20 $\text{pm}/^\circ\text{C}$	0.994
		8 cm	7.98 $\text{pm}/^\circ\text{C}$	0.990
		12 cm	7.31 $\text{pm}/^\circ\text{C}$	0.997
		16 cm	7.10 $\text{pm}/^\circ\text{C}$	0.990
	Strain	4 cm	-0.41 $\text{pm}/\mu\epsilon$	0.932
		8 cm	-2.11 $\text{pm}/\mu\epsilon$	0.980
		12 cm	0.30 $\text{pm}/\mu\epsilon$	0.951

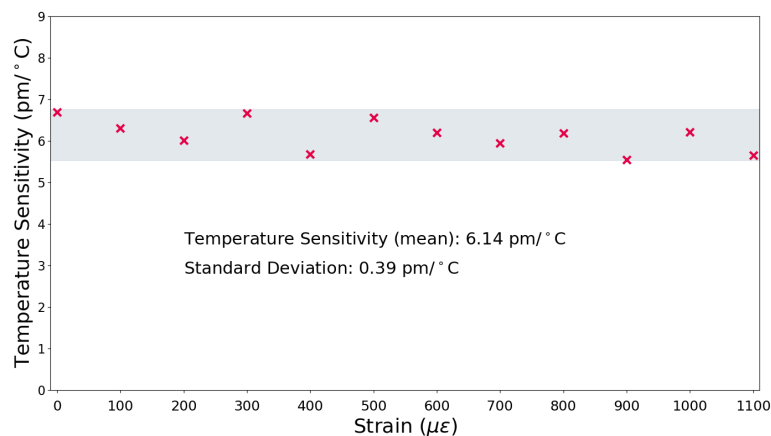
### 3.3. Strain-Insensitive Temperature Measurement

The comprehensive study of temperature and strain sensors based on the SMS structure using standard MMFs implies that the strain sensitivity is relatively low. Therefore, it is assumed that the SMS structure with standard MMF can be used as a strain-insensitive temperature sensor.

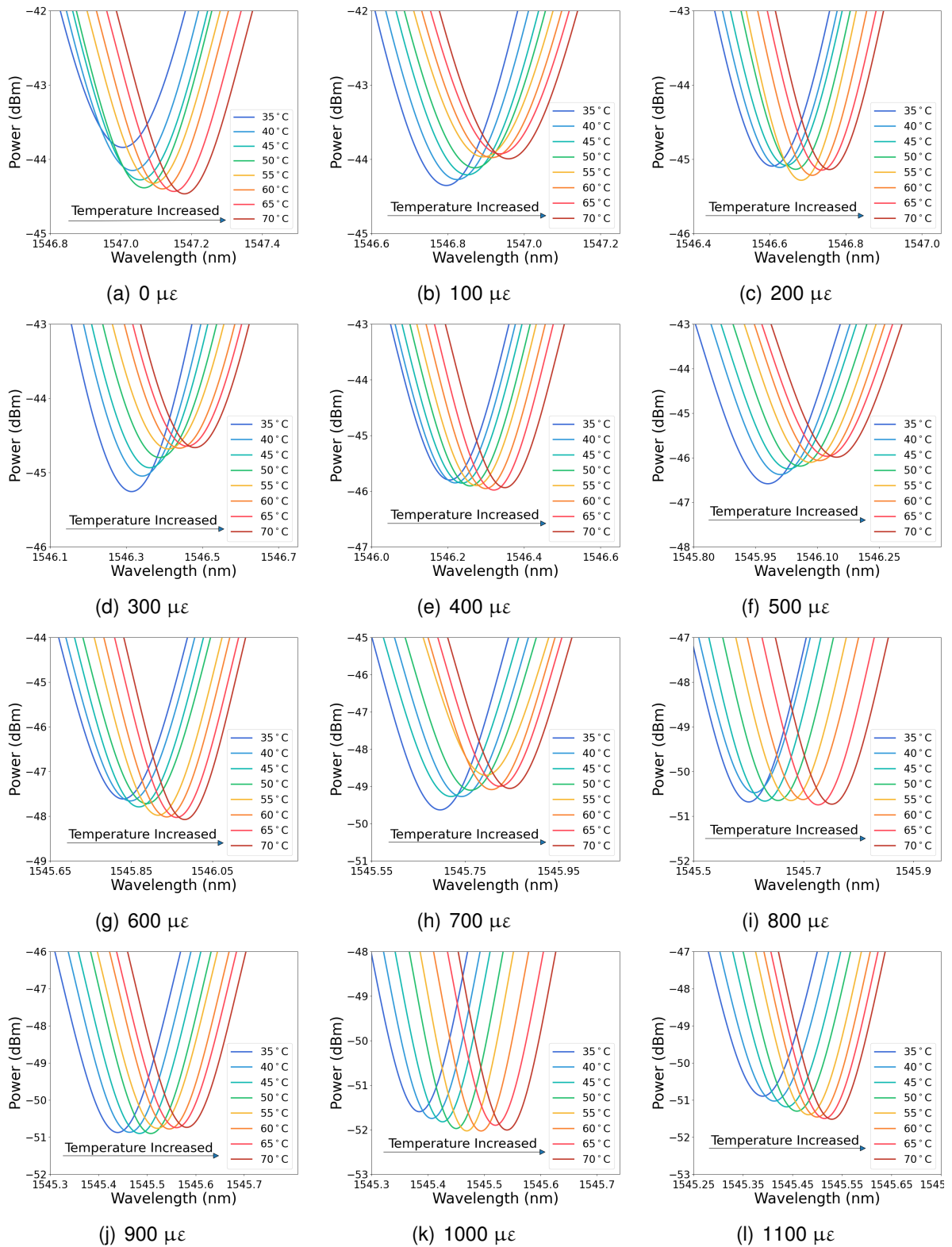
To prove it, the measurement is performed with the same setup as shown in Fig. 3.1. According to the configuration of the setup, a 25-cm-long MMF section is placed on the heating plate while the axial strain is applied, which is in the range of 0 to 1100  $\mu\epsilon$  with steps of 100  $\mu\epsilon$ . First, when no strain is applied, the temperature measurement is carried out in the same temperature range of 35 to 70°C with steps of 5°C. Then, a temperature measurement is completed under the same condition for each applied strain.

Figure 3.10 shows the measured dependences of the spectral dip on temperature with each applied strain, and Fig. 3.11 presents the related measured temperature sensitivity. First, the measurement results enhance the conclusion of the length of the MMF section. Figure 3.10(a) presents the measured dependence of the spectral dip on the temperature when no strain is applied, and the obtained temperature sensitivity is 6.69  $\text{pm}/^\circ\text{C}$  with an  $R^2$  value of 0.988, as shown in Fig. 3.11(a). Compared to Table 3.3, as the same MMF with 25 cm is used, it further enhances the conclusion that the longer MMF section leads to lower temperature sensitivity.

The measured results are summarized and plotted in Fig. 3.9. The temperature sensitivities are distributed within  $\pm 10\%$  of the mean temperature sensitivity while the strain is applied in the range from 0 to 1100  $\mu\epsilon$ , which indicates that the temperature sensitivity exhibits good stability and insensitivity against strain. The average measured temperature sensitivity is 6.14  $\text{pm}/^\circ\text{C}$  with a standard deviation of 0.39  $\text{pm}/^\circ\text{C}$ .



**Figure 3.9.:** Measured temperature sensitivity plotted as a function of strain. The gray area indicates the  $\pm 10\%$  range of the mean temperature sensitivity.



**Figure 3.10.:** Temperature measurement results with varied applied strains in the range of 0 to 1100  $\mu\epsilon$  with steps of 100  $\mu\epsilon$ .

### 3.3. Strain-Insensitive Temperature Measurement

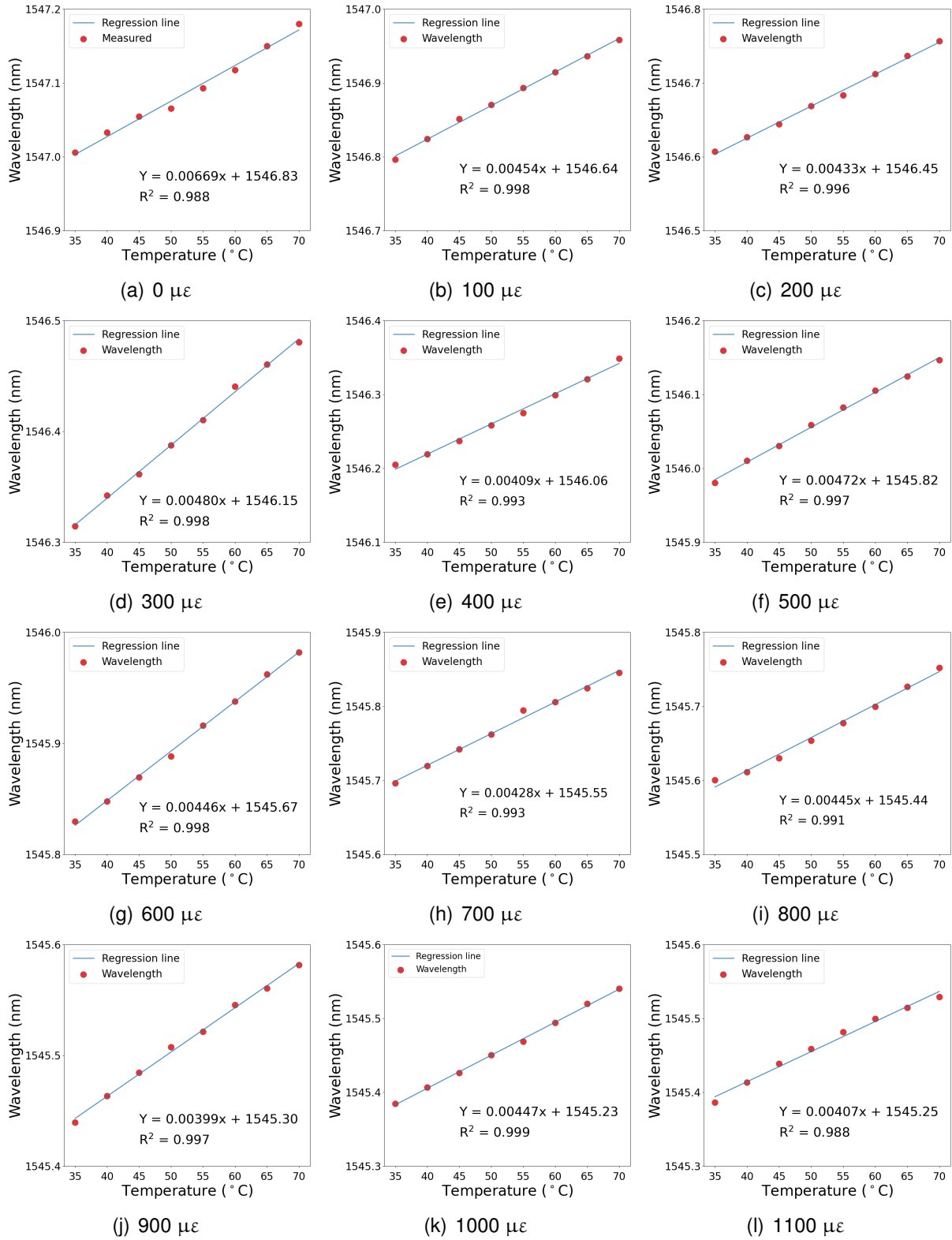


**Figure 3.11.:** Spectral dip shifts as a function of temperature with varied strains applied in the range of 0 to 1100  $\mu\epsilon$  with steps of 100  $\mu\epsilon$ .

### 3.4. Summary

Comprehensive research of three characteristics of the standard MMF was performed, and based on the findings, a strain-insensitive temperature sensor was proposed and investigated experimentally. Different commonly used standard MMFs were studied for temperature and strain sensing. The characterization study of these MMFs concludes:

- 1) The larger core diameter of the MMF leads to higher temperature sensitivity but lower strain sensitivity (absolute values).
- 2) The measured temperature sensitivity is independent of the NA of the MMF section, while the higher NA of the MMF leads to a higher absolute value of strain sensitivity.
- 3) The longer MMF section leads to lower temperature sensitivity, while the measured strain sensitivity is independent of the length of the MMF section.

This experimental study may contribute to the fundamental discussion of whether the temperature and strain sensitivities of the standard SMS fiber sensor are dependent on the length of the MMF, based on the theoretical analysis [151].

The strain-insensitive temperature sensor was tested based on these results. The applied strain range is from 0 to 1100  $\mu\epsilon$  with steps of 100  $\mu\epsilon$ , and the mean measured temperature sensitivity is 6.14  $\text{pm}/^\circ\text{C}$  with a standard deviation of 0.39  $\text{pm}/^\circ\text{C}$ . The results show that the proposed temperature fiber sensor with standard MMFs is insensitive to strain.

This work will be a valuable and essential guideline for developing MMI-based fiber sensors in the near future.

## 4. Temperature and Strain Sensing Based on Square-Core Fiber

As mentioned in Section 2.2.3.II, to solve current challenges, such as linearity, crosstalk, and compactness, it is essential to study new types of fibers. Recently, several new fibers, like HACF [111] and square NCF [112], have demonstrated advantages in overcoming some of these limits.

In this chapter, a new fiber, the square-core fiber (SCF), is investigated. The temperature and strain sensing based on the MMI in the SCF are studied. Square-core fiber produces an optical beam with uniform intensity over the core area because the shape of the core promotes mode mixing as light propagates through the fiber. It results in an even distribution of spatial modes in the output beam; therefore, it is ideal for applications such as laser machining. Further, square-core fiber also offers reduced focal ratio degradation, which means the square core shape is free from the input-output correlations, showing great potential for imaging and spectroscopy applications. These features of square-core fiber have been demonstrated by Velsink et al. by investigating the core shape, i.e., square core shape and circular core shape, for wavefront shaping applications where a focus is formed at the output of the MMF [161]. However, the sensing ability of square-core fiber has not been experimentally studied.

In the following, we demonstrate that the sensing performance of square-core fiber is promising. In addition, as the square core shape has yet to be experimentally proved, a comparison to other specialty fibers, mostly circular core shapes, is also presented. The experimental results also show this fiber sensor can exhibit strain-insensitive high-sensitivity temperature sensing.

### 4.1. Sensor Fabrication and Principle

The square-core fiber (FP150QMT, Thorlabs) features a  $150 \pm 10 \mu\text{m} \times 150 \pm 10 \mu\text{m}$  square silica core, surrounded by a  $\phi 225 \mu\text{m}$  circular polymer cladding, as shown in Fig. 4.1. As the cladding of SCF is made of hard polymer, it is not feasible to fusion splice the SCF with SMF, so it is connected to two silica SMFs by butt-coupling [159], i.e., both

ends of the SCF are connected to the ends of SMFs via FC/PC mating adaptors. It is noted that butt-coupling requires high optical quality end faces of the corresponding fibers. Due to the large core size and cladding materials of the SCF, the commonly used high-precision fiber cleaver cannot conduct the cleaving. It is necessary to point out that one possibility is to use a manual fiber scribe (Carbide Fiber Scribe, S90C, Thorlabs) to cleave the SCF and produce an optical quality end face.

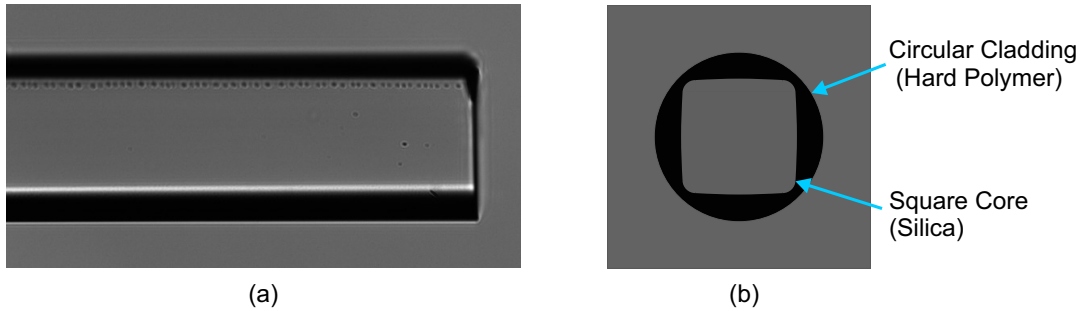


**Figure 4.1.:** (a) Photo of square-core fiber from the top view. (b) Schematic diagram of the square core shape.

The sensor configuration consists of a section of an SCF sandwiched between two SMFs. The general sensing principle of the SMS fiber sensor is based on the self-imaging effect in the multimode waveguide, i.e., multimode interference (MMI). When light is guided through the input SMF and injected into the multimode SCF, multiple modes are excited and travel along the SCF with their own propagation constants. At the second conjunction of SCF/SMF, these fields are coupled back to the fundamental mode of the output SMF. Under the assumption that the SCF and the two SMFs are perfectly aligned, the power in the output SMF can be expressed by Eq. 2.5.

**Table 4.1.:** Parameters of the fibers used in the beam propagation simulation.

Fiber Info.	Core Diameter	Cladding Diameter	Core RI	Cladding RI
SMF	9 $\mu\text{m}$	125 $\mu\text{m}$	1.4504	0.994
Circular MMF	105 $\mu\text{m}$	125 $\mu\text{m}$	1.45	1.4332
SCF	150 $\mu\text{m}$	225 $\mu\text{m}$	1.45	1.3966

To better understand the beam propagation in the SCF-implemented SMS structure, a simulation is conducted by BPM-Matlab [162] to compare the beam propagation in the circular core and square-core fiber. The parameters used for the beam propagation simulation, including core diameter, cladding diameter, core RI, and cladding RI, are adapted from

the commercial fibers (FG105LCA and FP150QMT, Thorlabs), as shown in Table 4.1. The lengths of the SMF and MMF are set to 1 cm and 10 cm, respectively, due to the computation power limit. Figure 4.2 and Fig. 4.3 show the beam propagating in the SMS structure comprising circular MMF and square-core fiber. The phase distributions in cross-sections at different lengths are also presented. Obviously, the periodic variation in the optical field intensity distribution due to the MMI occurs in both fibers. The difference is that the phase distribution is cross-shaped in the SCF, whereas it is asymptotic and circular in the circular MMF.

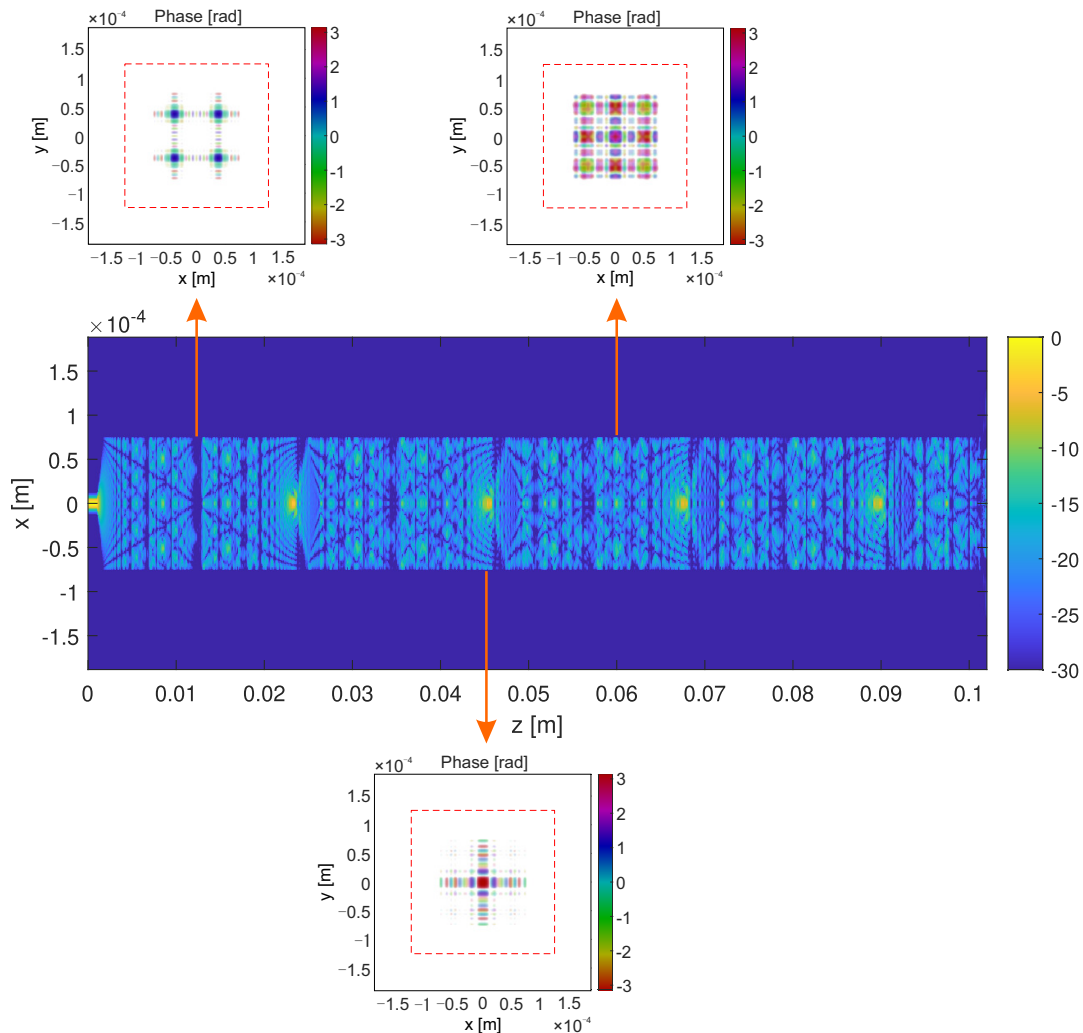


**Figure 4.2.:** Beam propagation in an SCF-based SMS structure with phase distributions at different lengths of the SCF.

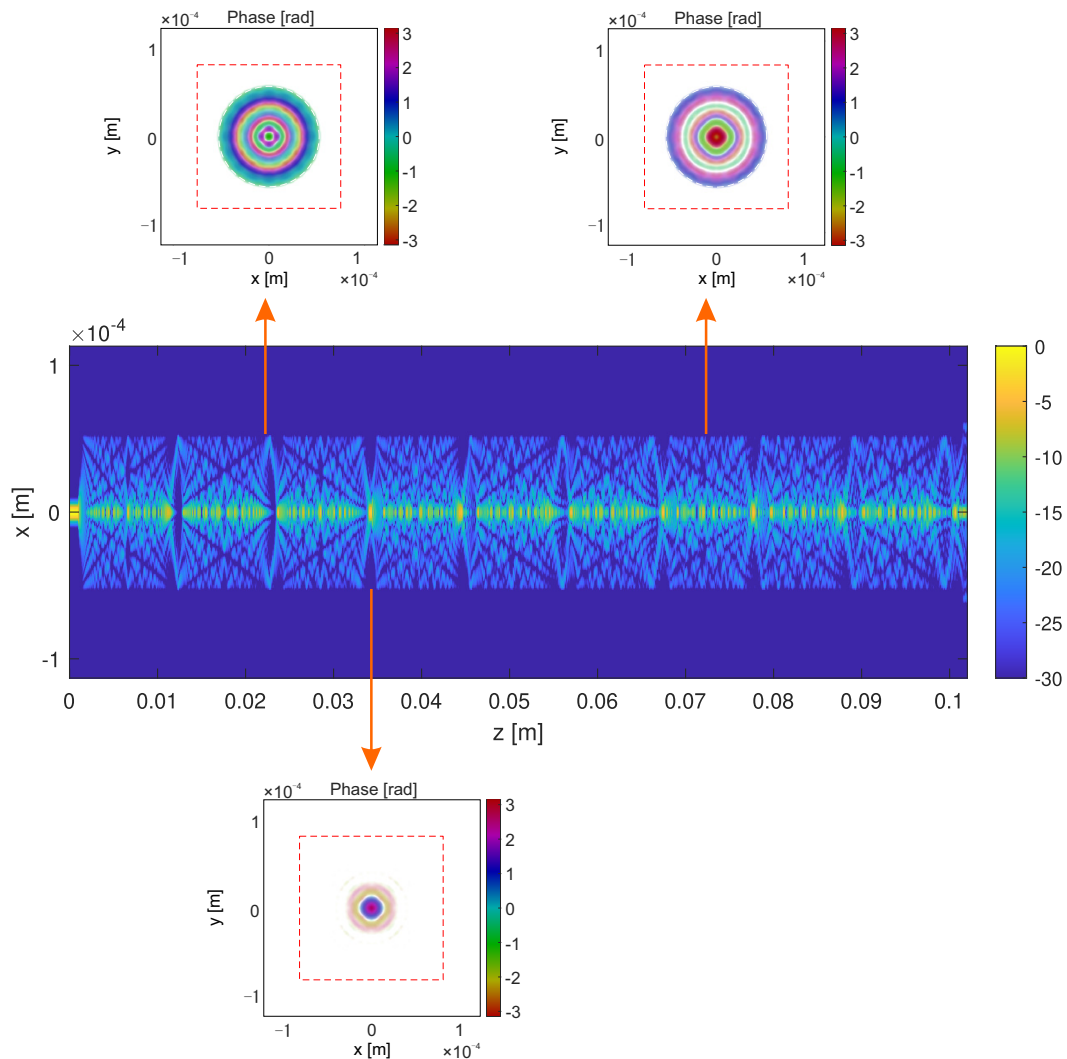


**Figure 4.3.:** Beam propagation in a circular MMF-based SMS structure with phase distributions at different lengths of the circular MMF.

This simulation clarifies the difference in beam propagation in the circular core MMF and the SCF. However, due to the limit of computational power, it is not feasible to simulate the same lengths and fiber types in this experiment. The sensing properties of the SCF are verified experimentally in the following.

The schematic diagram of the experimental setup for temperature and strain sensing is shown in Fig. 4.4. The SCF with a length of 30 cm is used as the sensing region and connected to two silica SMFs (size:  $9/125 \mu\text{m}$ ) by butt-coupling. The other end of the input SMF is connected to a BLS (central wavelength: 1550 nm) emitting the incident light, while the other end of the output SMF is connected to an OSA, which detects the changes in

the light spectrum. The SCF section is placed on a heating plate and clamped onto two precision translation stages, which are used to apply axial tensile stress on the sensor. The applied axial strain can be calculated by Eq. 3.4.

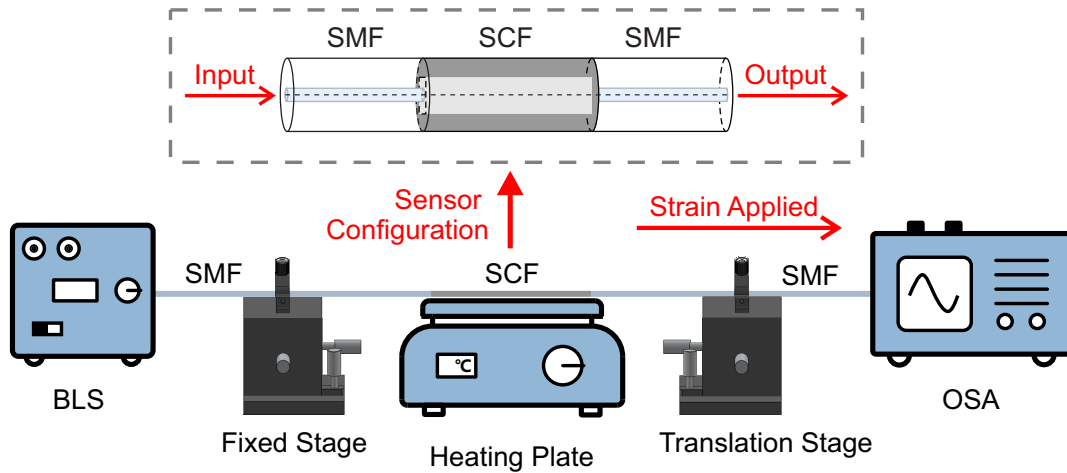


**Figure 4.4.:** Schematic diagram of the experimental setup and the sensor configuration. BLS, broadband light source; SMF, single-mode fiber; SCF, square-core fiber; OSA, optical spectrum analyzer.

The transmission spectrum contains multiple dips caused by multimode interference within the spectrum range. In typical multimode interference structures, the interference fringes are distorted due to multiple modes, which are excited and participate in the interference. Although any of these dips (or peaks) can be used as a spectral indicator for sensing, the least distorted one is typically chosen to minimize the measurement error. As the cleaved end face of the SCF is not perfect, as shown in Fig. 4.1, we choose the spectral dip close to the central wavelength 1550 nm of the BLS.

## 4.2. Temperature and Strain Measurement

The temperature dependence of the proposed fiber sensor was first measured without strain applied. The SCF section was heated in steps of 10°C to stabilize the sensing ability from 30 to 80°C. As shown in Fig. 4.5(a), the wavelength and power of the selected spectral dip change as the temperature changes. The dip shifts to a shorter wavelength when the temperature increases, accompanied by increased transmission power. The resulting changes in dip wavelength and transmission power versus temperature are plotted and fitted in Fig. 4.5(b). The fitting results of wavelength-temperature (blue solid line) and power-temperature (green dash-dot line) both exhibit a high linear regression coefficient value ( $R^2$ )

when subject to linear regression analysis. It is determined that the wavelength-temperature sensitivity is  $-15.0 \text{ pm}/^\circ\text{C}$  with an  $R^2$  value of 0.926, and the power-temperature sensitivity is  $0.0878 \text{ dBm}/^\circ\text{C}$  with an  $R^2$  value of 0.974. The absolute value of wavelength-temperature sensitivity is comparable with other specialty fiber-based sensors, such as the fiber sensor based on cascaded SNS and the SMS fiber structure; the absolute value of obtained wavelength-temperature sensitivity is around 1.7 times that [83].

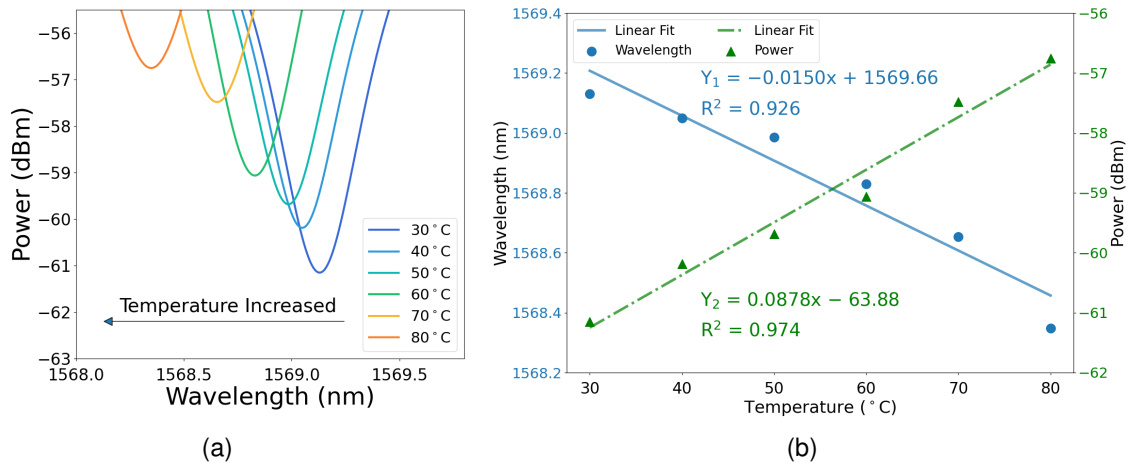


**Figure 4.5.:** (a) Measured dependence of spectral dip shifts on temperature in the range of 30 to  $80^\circ\text{C}$  in steps of  $10^\circ\text{C}$ . (b) Dip shift as a function of temperature. The blue solid line represents the dip wavelength shift against temperature, and the green dash-dotted line represents the dip power against temperature.

Furthermore, the experiment of strain measurement is conducted at room temperature (average of  $20^\circ\text{C}$ ). The strain is applied in the range of 0 to  $1000 \mu\epsilon$  with steps of  $200 \mu\epsilon$ . The measured dependence of the spectral dip on strain is shown in Fig. 4.6(a). The spectral dip shifts to the shorter wavelengths with increasing applied strain, whereas the transmission power increases. Figure 4.6(b) illustrates the dip wavelength and transmission power against strain, including the wavelength-strain (blue solid line) and power-strain (green dash-dotted line) sensitivities. It shows that both fitting curves exhibit good linearity with high  $R^2$  values. The wavelength-strain sensitivity is  $-1.0 \text{ pm}/\mu\epsilon$  with an  $R^2$  values of 0.868, and the power-strain sensitivity is  $0.0657 \text{ dBm}/\mu\epsilon$  with an  $R^2$  values of 0.983. The absolute value of the wavelength-strain sensitivity is comparable to the strain sensitivity of a thin core fiber implemented MMI-based fiber sensor with a core-offset structure [113].

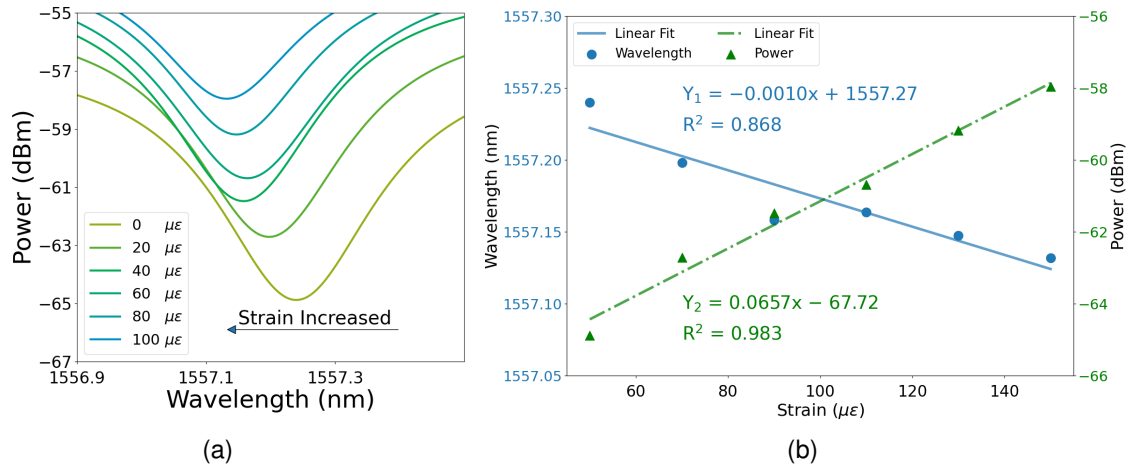


**Figure 4.6.:** (a) Measured dependence of spectral dip shifts on strain in the range of 0 to 100  $\mu\epsilon$  in steps of 20  $\mu\epsilon$ . (b) Dip shift as a function of strain. The blue solid line represents the dip wavelength shift against strain, and the green dash-dotted line represents the dip power against strain.

**Table 4.2.:** Comparison of temperature sensitivities with other MMI-based optical fiber sensors using specialty fibers.

Optical Fiber Sensor Structure	Measurement Range	Sensitivity (max.)	Reference
SMF – HCF – SMF (with abrupt taper joints)	18–50°C	12.3 pm/°C	[110]
SMF – NCF – SMF – MMF – SMF	30–90°C	9.2 pm/°C	[83]
SMF – Tapered NCF – SMF	0–280°C	16.56 pm/°C	[73]
SMF – NCF – SMF (with FBGs)	0–50°C	12.8 pm/°C	[100]
Tapered SMF – Micro MMF – Tapered SMF	35–60°C	0.028 dB/°C	[74]
SMF – SCF – SMF	30–80°C	–15.0 pm/°C 0.0878 dBm/°C	This work

Comparing Fig. 4.5(b) and Fig. 4.6(b), the absolute value of wavelength temperature sensitivity shows high-temperature measurability, while the small absolute value of wavelength-strain indicates that the proposed fiber sensor is less sensitive to applied strain. Therefore,

the multimode interference in the square-core fiber can be potentially exploited to develop high-sensitivity temperature sensors with reduced strain sensitivity. Table 4.2 presents a comparison of the temperature measurability for different specialty fibers, showing that square-core fiber's temperature sensing ability is promising with a simple structure.

### 4.3. Strain-insensitive Temperature Measurement

Based on the conclusion that the strain sensitivity at room temperature in an MMI-based sensor using an SCF can be extremely low, strain-insensitive temperature sensing is demonstrated using the SCF-based SMS structure. The sensor configuration and experimental setup are the same as shown in Fig. 4.4, where an SCF with a length of 25 cm is used in this experiment. The temperature dependence of the transmitted spectral dip is investigated while a strain is applied from 0 to 500  $\mu\epsilon$  with steps of 100  $\mu\epsilon$ .

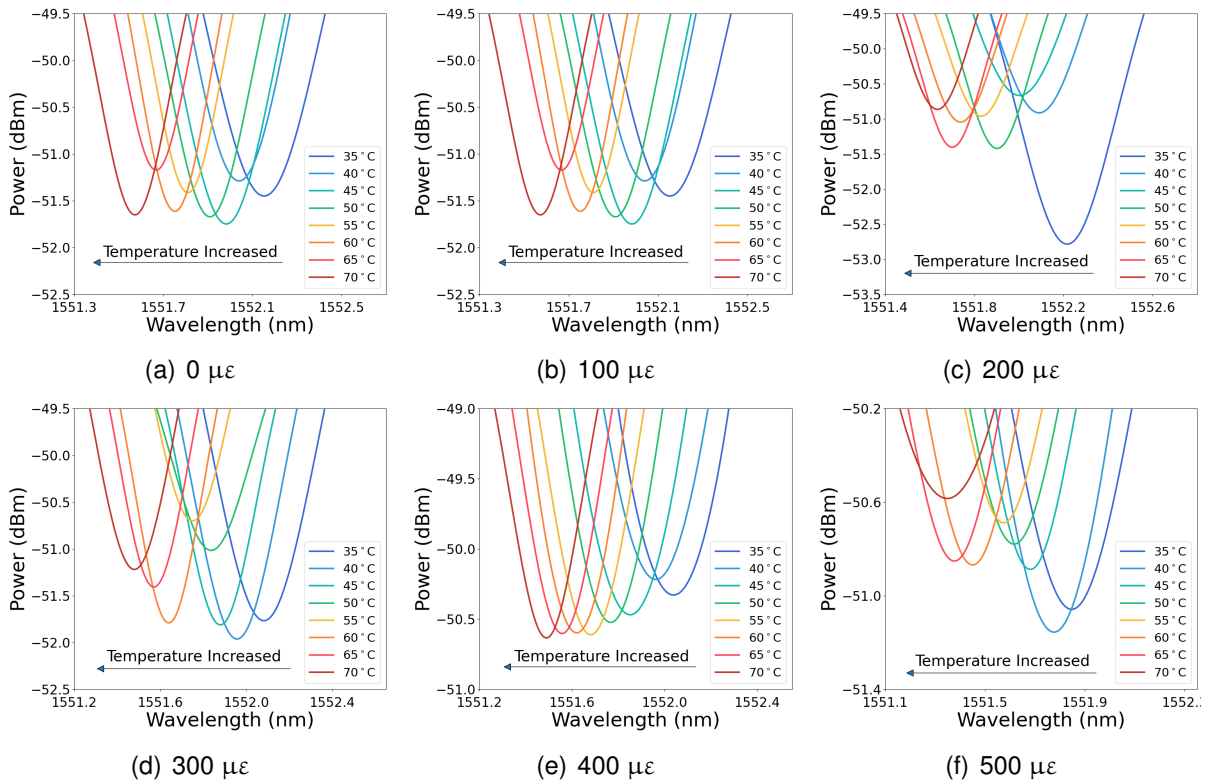


**Figure 4.7.:** Temperature measurement results with varied applied strains. Measured spectral dependences on temperature: (a) 0  $\mu\epsilon$ , (b) 100  $\mu\epsilon$ , (c) 200  $\mu\epsilon$ , (d) 300  $\mu\epsilon$ , (e) 400  $\mu\epsilon$ , and (f) 500  $\mu\epsilon$  strains applied.

First, the temperature measurement is performed in the range of 35 to 70°C in steps of

### 4.3. Strain-insensitive Temperature Measurement

5°C with no strain applied. Then, the experiment is carried out under the same conditions while the strain is applied in the range of 0 to 500  $\mu\epsilon$  with steps of 100  $\mu\epsilon$ . The measured dependences of the spectral dip on temperature are shown in Fig. 4.7. The spectral dips exhibit blueshifts in the wavelength domain when the temperature increases. The corresponding resulting wavelength shifts of the spectral dips against the increasing temperature are plotted and fitted in Fig. 4.8. The temperature sensitivities are calculated to be  $-22.19 \text{ pm}/^\circ\text{C}$ ,  $-22.19 \text{ pm}/^\circ\text{C}$ ,  $-22.79 \text{ pm}/^\circ\text{C}$ ,  $-23.01 \text{ pm}/^\circ\text{C}$ ,  $-21.96 \text{ pm}/^\circ\text{C}$ , and  $-21.93 \text{ pm}/^\circ\text{C}$  for 0  $\mu\epsilon$ , 100  $\mu\epsilon$ , 200  $\mu\epsilon$ , 300  $\mu\epsilon$ , 400  $\mu\epsilon$ , and 500  $\mu\epsilon$  strain applied. The fitting results are all with high  $R^2$  values in the range of 0.983 to 0.996.

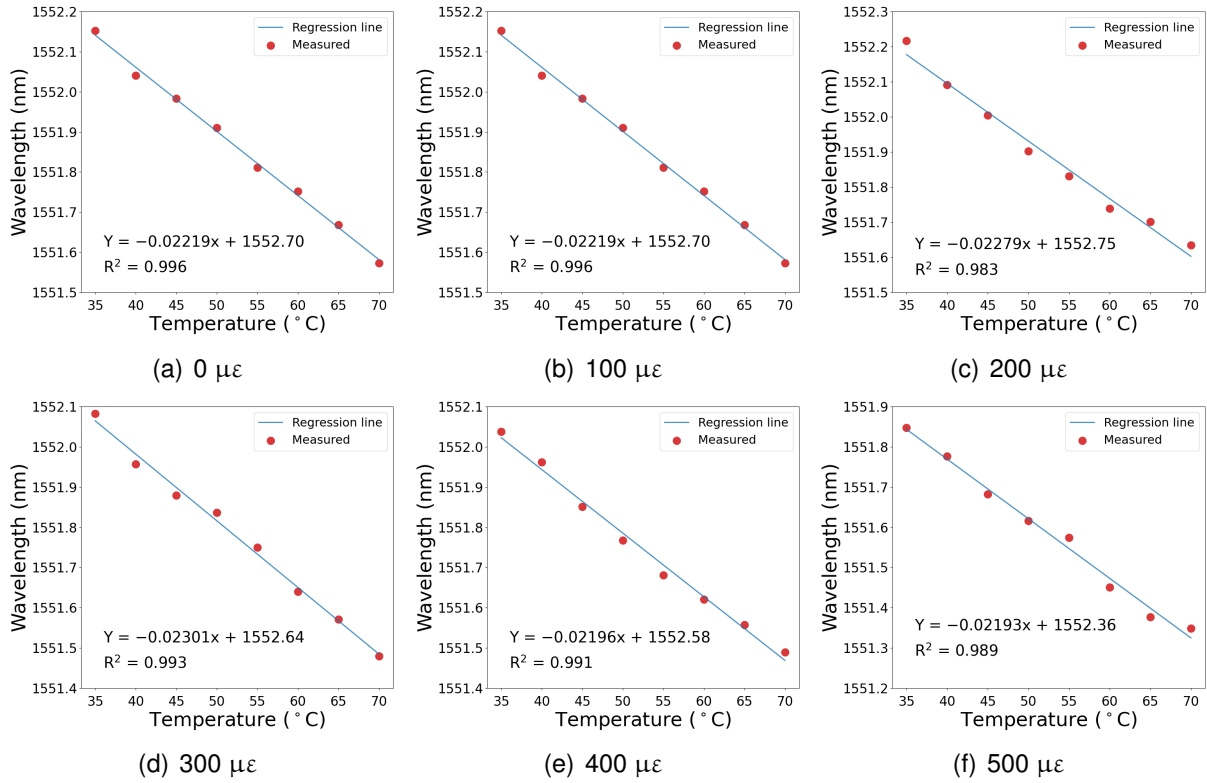


**Figure 4.8.:** Spectral dip shifts as a function of temperature with varied strains applied: (a) 0  $\mu\epsilon$ , (b) 100  $\mu\epsilon$ , (c) 200  $\mu\epsilon$ , (d) 300  $\mu\epsilon$ , (e) 400  $\mu\epsilon$ , and (f) 500  $\mu\epsilon$  strains applied.

Figure 4.9 shows the temperature sensitivities plotted as a function of strain, which are distributed within  $\pm 3\%$  of their mean value of  $-22.35 \text{ pm}/^\circ\text{C}$ . The standard deviation is as small as  $0.44 \text{ pm}/^\circ\text{C}$ . Chapter 3 demonstrated the temperature sensitivity of the strain-insensitive temperature sensor using a standard MMF with the same length (25 cm), which is  $6.32 \text{ pm}/^\circ\text{C}$ . Therefore, the absolute value of the temperature sensitivity of the SCF-based sensor is  $\sim 3.5$  times that of a standard MMF. This result indicates that the temperature

sensitivity exhibits remarkable stability with almost no influence of strain.

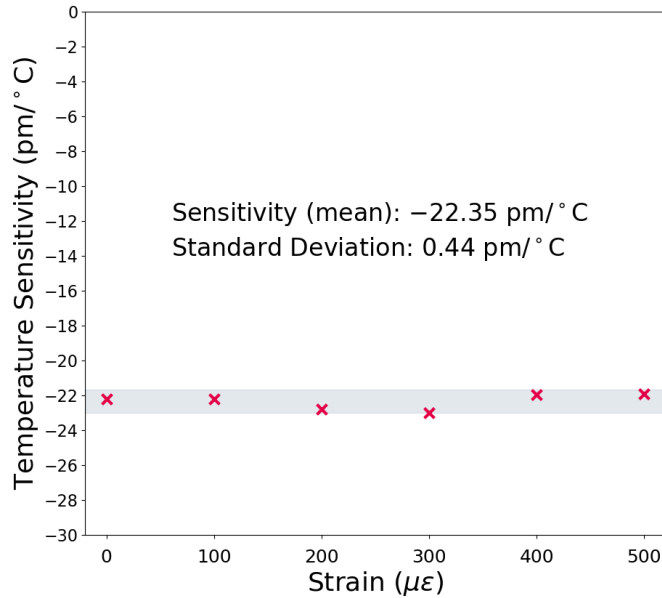


**Figure 4.9.:** Measured temperature sensitivity plotted as a function of strain. The gray area indicates the  $\pm 3\%$  range of the mean temperature sensitivity.

## 4.4. Summary

The sensing characteristics of the SCF were experimentally investigated in a simple SMS structure for temperature and strain measurement. Besides, a beam propagation simulation in the circular MMF and the SCF was conducted and compared for a better understanding of the MMI in the SCF.

The obtained maximal wavelength-temperature and wavelength-strain sensitivities are  $-15.0 \text{ pm}/^\circ\text{C}$  and  $-1.0 \text{ pm}/\mu\epsilon$ , respectively, with the maximal power sensitivities of  $0.0878 \text{ dBm}/^\circ\text{C}$  and  $0.0657 \text{ dBm}/\mu\epsilon$  for temperature and strain. The measurement results proved that the SCF is promising for sensing. As the strain sensitivity is extremely low compared to the temperature sensitivity, it also indicates that this sensor can exhibit great potential applications in strain-insensitive temperature measurement.

Based on the characterization of the SCF for temperature and strain sensing, a strain-insensitive high-sensitivity temperature sensor based on an SMS structure consisting of a section of an SCF was developed. The obtained mean temperature sensitivity is  $-22.35 \text{ pm}/^\circ\text{C}$  (with a standard deviation of  $0.44 \text{ pm}/^\circ\text{C}$  in the strain range of 0 to  $500 \mu\epsilon$ ), which is  $\sim 3.5$

times higher than the sensitivity (absolute value) of a standard MMF-based configuration under the same condition.

The investigation of the SCF refers to the technique outlook of fiber sensors that using a new type of optical fiber (in Section 2.2.3.II) may improve the sensitivity. This study will also contribute to the design of strain-insensitive temperature fiber sensors and the development of MMI-based specialty fiber sensors in the future.



## 5. Core-Offset-Based Temperature and Strain Sensing

New optical fiber sensor configurations are verified to enhance the sensitivities and overcome some limits mentioned in Section 2.2.3.II, like tapered and side-polished SMS structures. Recently, another structure, i.e., core-offset structure, has attracted considerable attention [163]. A Mach-Zehnder interferometer, based on the core-offset SMS structure comprising a few-mode fiber, has led to a strain sensitivity of  $3.35 \text{ pm}/\mu\epsilon$  within the range of 0 to  $1000 \mu\epsilon$  [164]. The offset structure also has the advantage of high RI sensitivity; for instance, by core-offset splicing of a triple cladding quartz specialty fiber between two SMFs, the RI sensitivity of as high as  $543.75 \text{ nm}/\text{RIU}$  has been achieved [165]. However, these core-offset structures utilized specialty fibers to enhance the sensitivities and had drawbacks such as fabrication difficulty, low repeatability, and high cost. Besides, for most core-offset structures, the balance between sensitivity and mechanical strength is another issue that needs to be studied. A larger core-offset value usually leads to higher sensing sensitivity, resulting in a vulnerable structure.

In this chapter, a simple, inexpensive, and high-sensitivity temperature and strain sensor based on an SMS structure with core offset is developed and experimentally characterized. This sensor does not include specialty fibers and can be fabricated using a standard fiber fusion splicer. The sensitivity dependences of the core-offset amplitudes at the input and output SMF/MMF boundaries are experimentally investigated. Additionally, as the larger core-offset also results in a more vulnerable structure, pull tests are performed to evaluate the mechanical strengths of the core-offset SMS structures.

### 5.1. Sensor Fabrication and Principle

The operating principle of conventional SMS sensing is based on the assumption that the MMF and two SMFs are perfectly aligned (refer to Eq. 2.5). However, this principle cannot be directly applied to the core-offset SMS sensing, where a larger number of higher-order modes are excited. It is natural to assume that the excitation of higher-order modes may lead to higher sensitivities; to verify this assumption, we experimentally characterize the

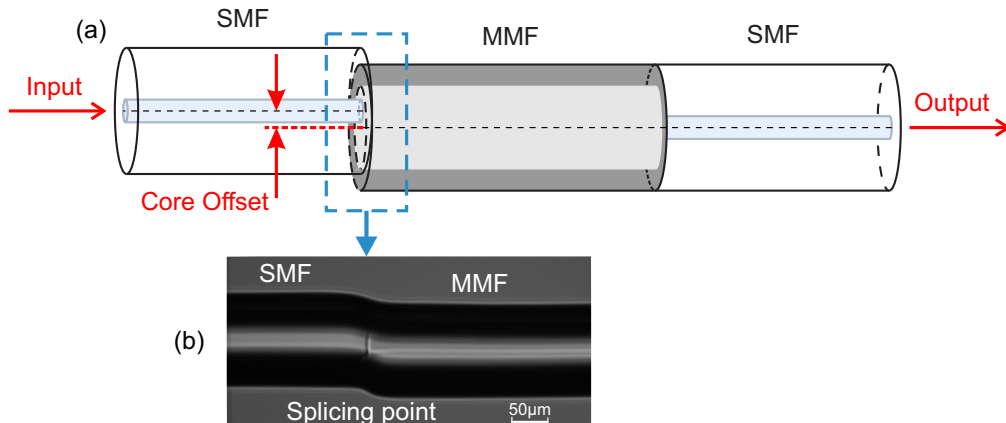


**Figure 5.1.:** (a) Schematic diagram of the core-offset SMS structure with an offset at the input SMF/MMF boundary. (b) Image of the core offset spliced (offset = 20  $\mu\text{m}$ ).

core-offset SMS structure and investigate the limit of the induced sensitivity enhancement.

The schematic diagram of the core-offset SMS structure is shown in Fig. 5.1(a). In this experiment, one side of the SMF is core offset spliced. To find the optimal core-offset SMS structure, different samples are fabricated utilizing standard SMFs (9/125) and a step-index MMF (50/125) with an inexpensive fiber fusion splicer (INNO View 7). The splicing settings are kept the same during the fabrication process of all the samples to ensure the consistency of the quality of the core offset. As the radius of the MMF core is 25  $\mu\text{m}$ , the samples with core-offset amplitudes of 10, 15, 20, 25, and 30  $\mu\text{m}$  are fabricated, as shown in Fig. 5.2.

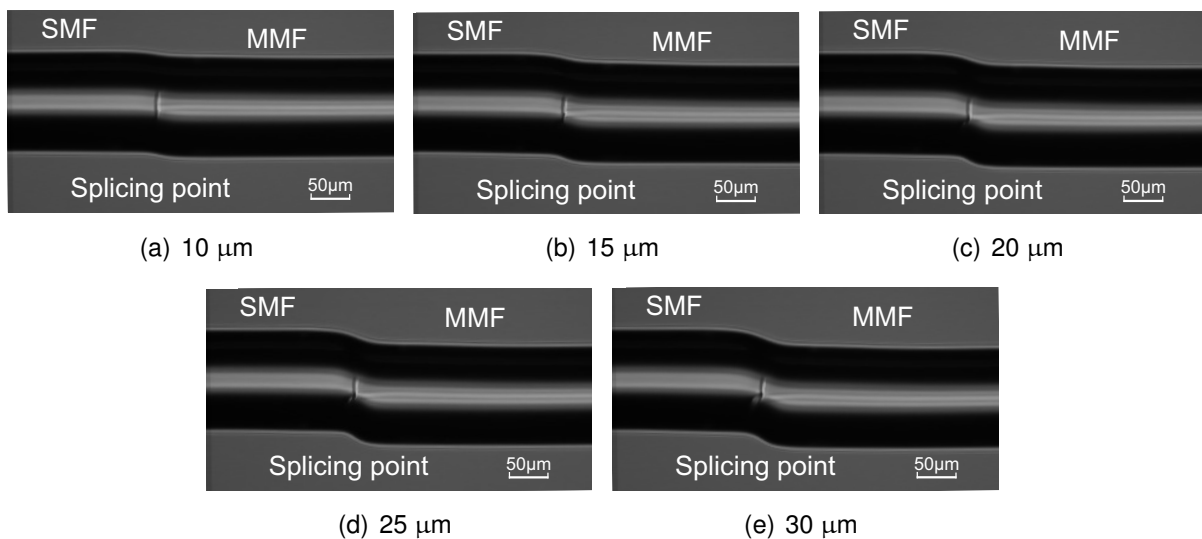
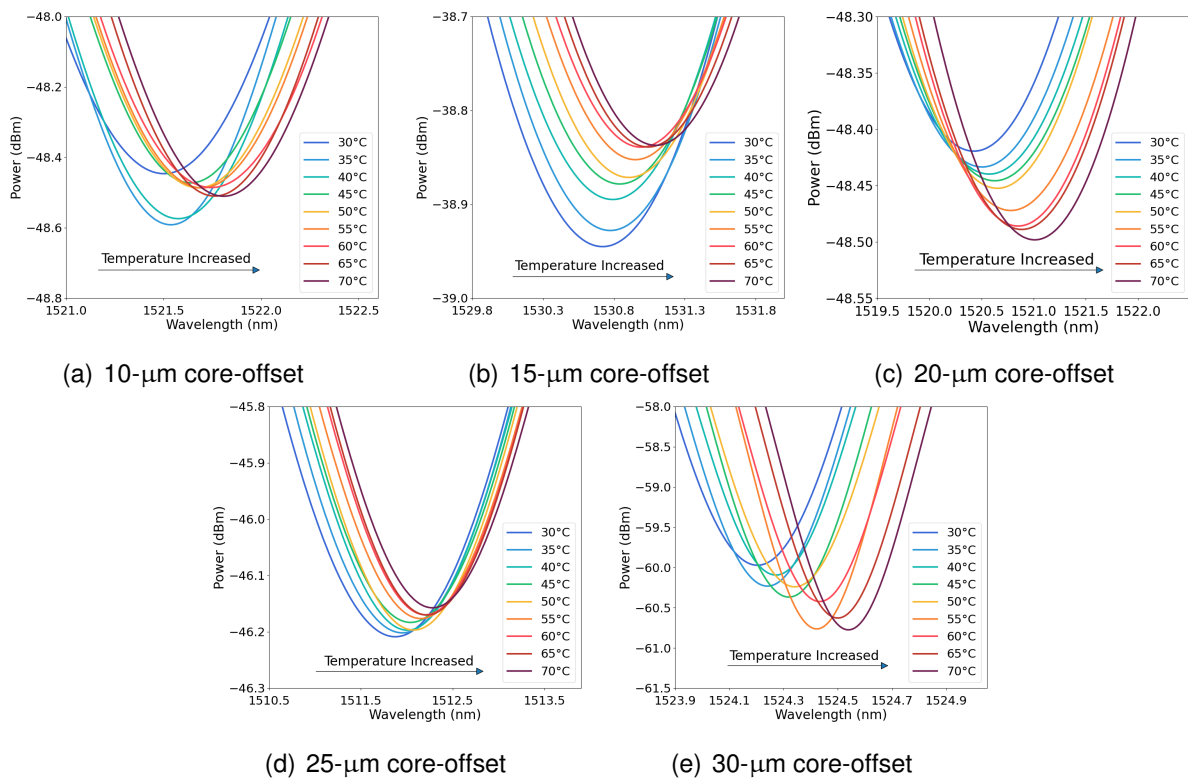


**Figure 5.2.:** Images of core-offset spliced parts with offset amplitudes of (a) 10  $\mu\text{m}$ , (b) 15  $\mu\text{m}$ , (c) 20  $\mu\text{m}$ , (d) 25  $\mu\text{m}$ , and (e) 30  $\mu\text{m}$ .

The experimental setup is illustrated in Fig. 3.1. The MMF section is heated and clamped onto two precision translation stages, which can apply varying axial tensile stress to the sample. The sensing characteristics of the input and output core-offset SMS structures are investigated separately. An aligned SMS sensor is also prepared in the same condition, as a reference. The applied axial strain can be calculated by Eq. 3.4. In addition, to check the mechanical strength of the core-offset SMS structures, pull tests are carried out using the same setup under the same conditions.

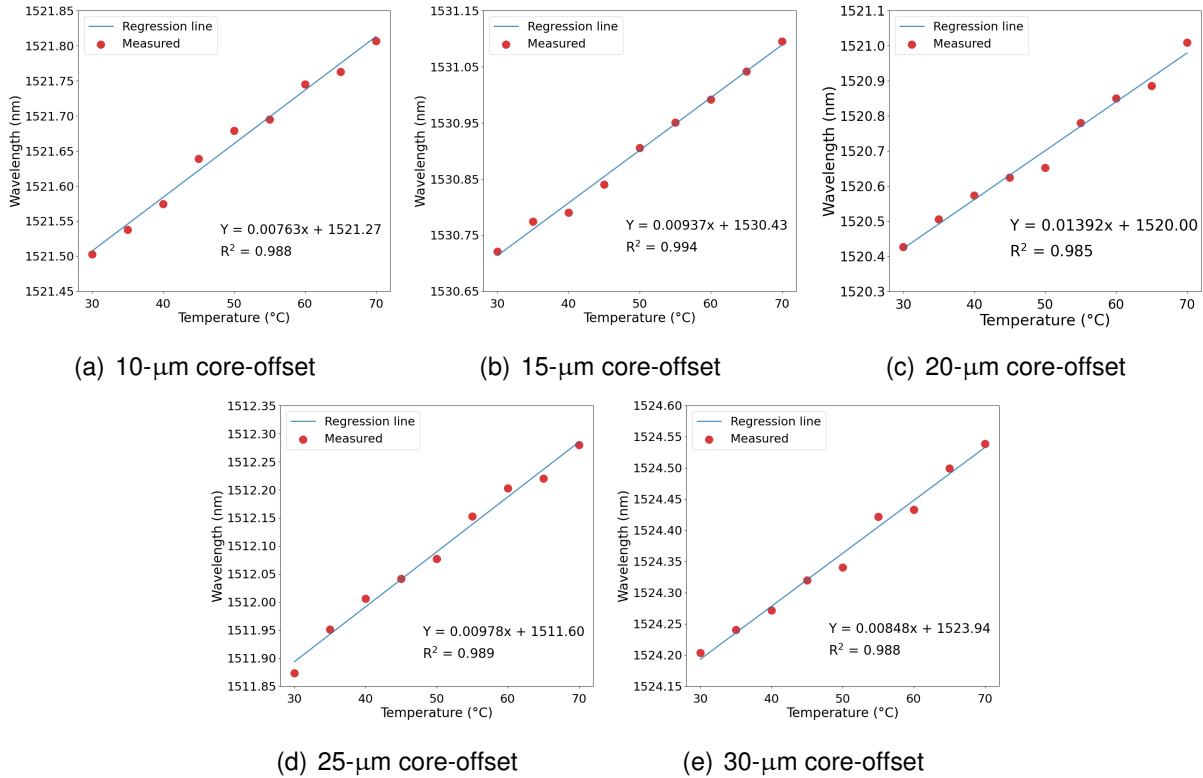
## 5.2. Temperature and Strain Measurement

The temperature measurement without applied strain is performed in the range of 30 to 70°C in steps of 5°C. Examples of the temperature sensing results for the input SMF with core-offset amplitudes of 10, 15, 20, 25, and 30  $\mu\text{m}$  are shown in Fig. 5.3. The spectral dips exhibit redshifts in the wavelength domain when the temperature increases, as shown in Fig. 5.3(a-e).



**Figure 5.3.:** Temperature measurement results for the input core-offset SMS structure. Measured spectral dependences on temperature with core-offsets of (a) 10  $\mu\text{m}$ , (b) 15  $\mu\text{m}$ , (c) 20  $\mu\text{m}$ , (d) 25  $\mu\text{m}$ , and (e) 30  $\mu\text{m}$ .

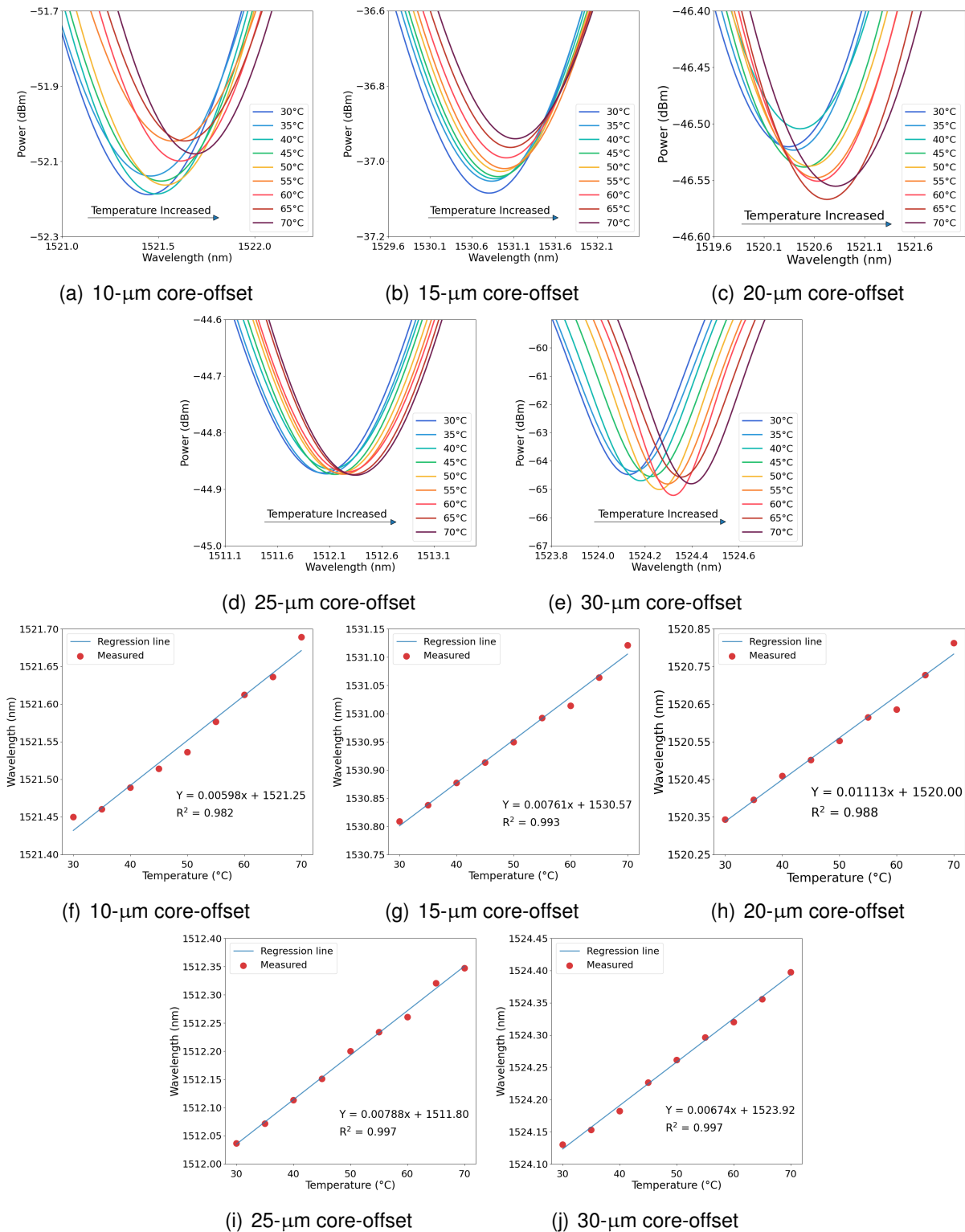
The corresponding resulting wavelength shifts of the spectral dips against the increasing temperature are plotted and fitted in Fig. 5.4(a-e). The dependences are almost linear, with coefficients of 7.63 pm/°C (10 μm), 9.37 pm/°C (15 μm), 13.92 pm/°C (20 μm), 9.78 pm/°C (25 μm), and 8.48 pm/°C (30 μm).



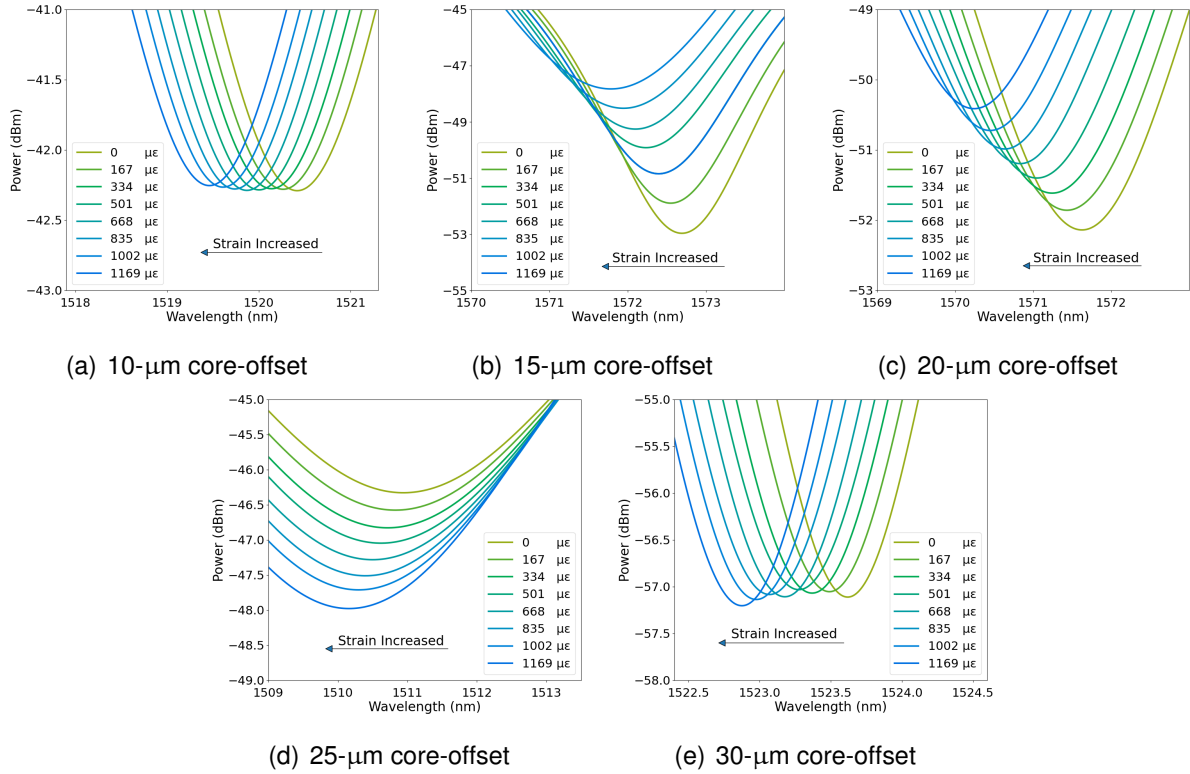
**Figure 5.4.:** Temperature measurement results for the input core-offset SMS structure. Spectral dip shifts plotted as a function of temperature with core-offsets of (a) 10 μm, (b) 15 μm, (c) 20 μm, (d) 25 μm, and (e) 30 μm.

Figure 5.5 shows the temperature sensing results for the output core-offset SMS structure. The spectral dip demonstrates a redshift in the wavelength domain when the temperature increases for the core offsets of 10, 15, 20, 25, and 30 μm, as displayed in Fig. 5.5(a-e). The corresponding resulting wavelength shift of the dip against the temperature variation is plotted and fitted in Fig. 5.5(f-j), which indicates that the relevant temperature sensitivities are determined to be 5.98 pm/°C (10 μm), 7.61 pm/°C (15 μm), 11.13 pm/°C (20 μm), 7.88 pm/°C (25 μm), and 6.74 pm/°C (30 μm).

## 5.2. Temperature and Strain Measurement



**Figure 5.5.:** Temperature measurement results for the output core-offset SMS structure. Measured spectral dependences on temperature with core-offsets of (a) 10  $\mu\text{m}$ , (b) 15  $\mu\text{m}$ , (c) 20  $\mu\text{m}$ , (d) 25  $\mu\text{m}$ , and (e) 30  $\mu\text{m}$ . Spectral dip shifts plotted as a function of temperature with core-offsets of (f) 10  $\mu\text{m}$ , (g) 15  $\mu\text{m}$ , (h) 20  $\mu\text{m}$ , (i) 25  $\mu\text{m}$ , and (j) 30  $\mu\text{m}$ .



**Figure 5.6.:** Strain measurement results for the input core-offset SMS structure. Measured spectral dependences on strain with core-offsets of (a) 10  $\mu\text{m}$ , (b) 15  $\mu\text{m}$ , (c) 20  $\mu\text{m}$ , (d) 25  $\mu\text{m}$ , and (e) 30  $\mu\text{m}$ .

Subsequently, the strain sensing is carried out at room temperature ( $\sim 20^\circ\text{C}$ ), and the results for the input core-offset SMS structure are illustrated in Fig. 5.6. The measured dependences of the spectral dip on strain are presented in Fig. 5.6(a-e) for the core-offsets of 10, 15, 20, 25, and 30  $\mu\text{m}$ , respectively. The spectral dips shift to shorter wavelengths with increasing strain. The corresponding resulting wavelength shifts of the spectral dips against the increasing strain are plotted and fitted in Fig. 5.7, which leads to coefficients of  $-0.8 \text{ pm}/\mu\epsilon$  (10  $\mu\text{m}$ ),  $-0.89 \text{ pm}/\mu\epsilon$  (15  $\mu\text{m}$ ),  $-1.19 \text{ pm}/\mu\epsilon$  (20  $\mu\text{m}$ ),  $-0.65 \text{ pm}/\mu\epsilon$  (25  $\mu\text{m}$ ), and  $-0.63 \text{ pm}/\mu\epsilon$  (30  $\mu\text{m}$ ).

The strain sensing results for the output core-offset SMS structure are presented in Fig. 5.8. The clear blueshifts of the wavelength dips are distinguished with increasing strain applied to the sensor with core-offsets of 10, 15, 20, 25, and 30  $\mu\text{m}$ , as shown in Fig. 5.8(a-e). The related wavelength shifts of the spectral dips against the increasing applied strain are displayed in Fig. 5.8(f-j). The measured strain sensitivities are  $-0.71 \text{ pm}/\mu\epsilon$  (10  $\mu\text{m}$ ),  $-0.78 \text{ pm}/\mu\epsilon$  (15  $\mu\text{m}$ ),  $-1.06 \text{ pm}/\mu\epsilon$  (20  $\mu\text{m}$ ),  $-0.60 \text{ pm}/\mu\epsilon$  (25  $\mu\text{m}$ ), and  $-0.57 \text{ pm}/\mu\epsilon$  (30  $\mu\text{m}$ ).

## 5.2. Temperature and Strain Measurement

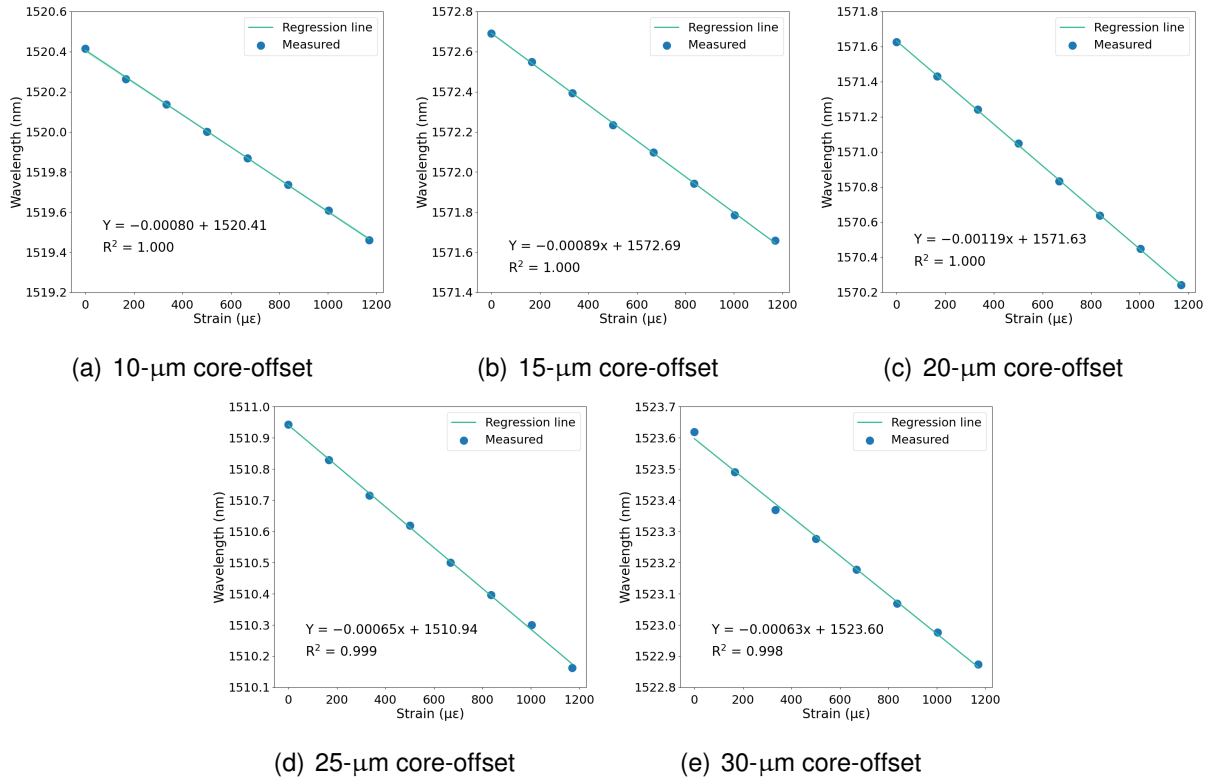


**Figure 5.7.:** Strain measurement results for the input core-offset SMS structure. Spectral dip shifts plotted as a function of strain with core-offsets of (a) 10  $\mu\text{m}$ , (b) 15  $\mu\text{m}$ , (c) 20  $\mu\text{m}$ , (d) 25  $\mu\text{m}$ , and (e) 30  $\mu\text{m}$ .

Note that 20  $\mu\text{m}$  is the largest offset when the core of the SMF is spliced to the core of the MMF; with offsets of  $>20 \mu\text{m}$ , the core of the SMF is (partially or totally) spliced to the cladding of the MMF, which does not promote the excitation of the higher-order modes in the MMF core.

Besides, the temperature and strain measurements of the aligned SMS sensor fabricated in the same conditions as the core-offset ones are performed to compare with the results of the offset SMS structures. The experiments are conducted using the same setup. The spectral dips shift to the longer wavelengths with increasing temperature and temperature sensitivity of  $5.83 \text{ pm}/^\circ\text{C}$  is obtained, as shown in Fig. 5.9(a-b). The blue shifts of the wavelength dips are clearly observed with increasing strain applied to the sensor, and the related strain sensitivity is  $-0.15 \text{ pm}/\mu\epsilon$ , as illustrated in Fig. 5.9(c-d).

## Chapter 5. Core-Offset-Based Temperature and Strain Sensing

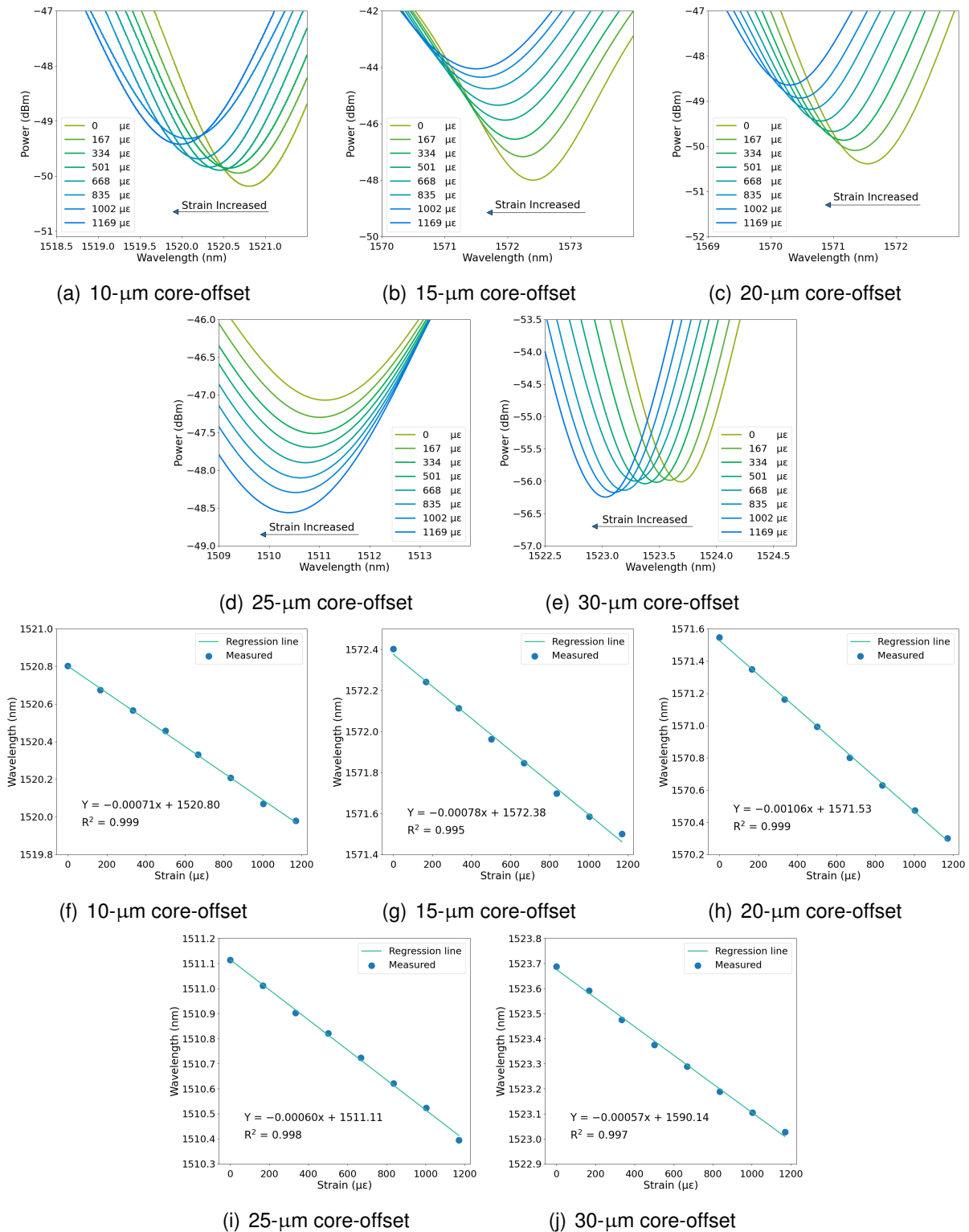


**Figure 5.8.:** Strain measurement results for the output core-offset SMS structure. Measured spectral dependences on strain with core-offsets of (a) 10  $\mu\text{m}$ , (b) 15  $\mu\text{m}$ , (c) 20  $\mu\text{m}$ , (d) 25  $\mu\text{m}$ , and (e) 30  $\mu\text{m}$ . Spectral dip shifts plotted as a function of strain with core-offsets of (f) 10  $\mu\text{m}$ , (g) 15  $\mu\text{m}$ , (h) 20  $\mu\text{m}$ , (i) 25  $\mu\text{m}$ , and (j) 30  $\mu\text{m}$ .

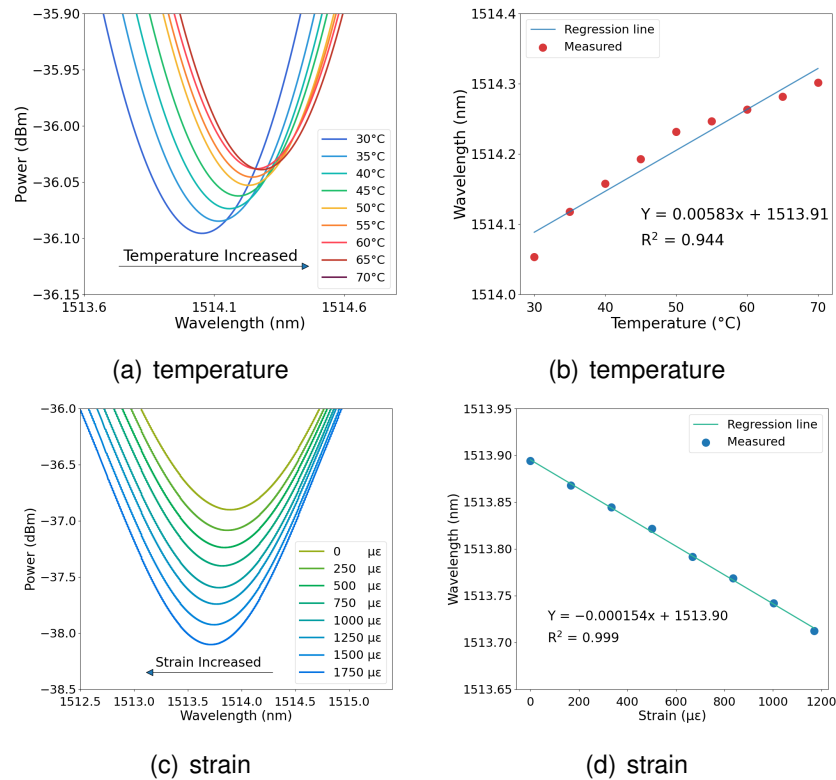


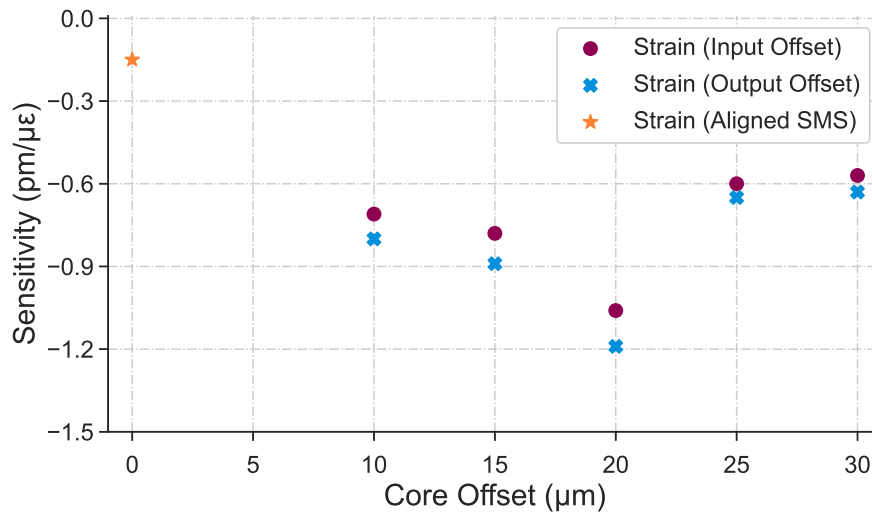
**Figure 5.9.:** Measured results of the aligned SMS sensor in the same conditions as core-offset sensors: (a) measured spectral dependences on temperature, (b) spectral dip shifts plotted as a function of temperature, (c) measured spectral dependences on strain, and (d) spectral dip shifts plotted as a function of strain.

### 5.3. Discussion

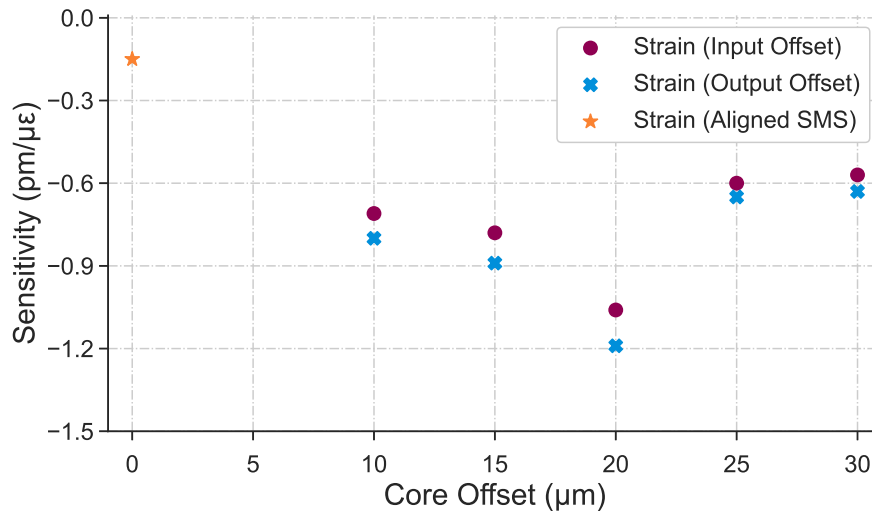
The summary of the temperature sensing with input and output core-offset SMS structures is illustrated in Fig. 5.10(a), which shows the temperature sensitivities with the input core-offset SMS are higher than those with output core-offset SMS. In addition, the temperature sensitivity exhibits a non-monotonic relationship with increasing core offset, and the highest temperature sensitivity of 13.92 pm/°C is achieved at the 20-μm core-offset. The maximal temperature sensitivity is approximately two times the value of the aligned SMS sensor's (5.83 pm/°C, refer to Fig. 5.9(b)).

Figure 5.10(b) shows the summary of the strain sensitivities with the input and output core-offset SMS structures. It indicates that the strain sensitivities (absolute values) with the input core-offset SMS are also higher than those with the output core-offset SMS. It also exhibits a non-monotonic relationship with increasing core-offset amplitude, and the maxi-

mal strain sensitivity (absolute value of  $-1.19 \text{ pm}/\mu\epsilon$ ) is obtained at the  $20\text{-}\mu\text{m}$  core-offset (where the highest temperature sensitivity is obtained). Compared to the strain sensitivity of the aligned SMS sensor ( $-0.15 \text{ pm}/\mu\epsilon$ , refer to Fig. 5.9(d)), the maximal strain sensitivity (absolute value) of the core-offset SMS sensor is enhanced by approximately eight times.



(a) temperature



(b) strain

**Figure 5.10.:** Summary of measurement with the input and output core-offset SMS structures: (a) temperature and (b) strain.

Besides, as it is assumed that the core-offset SMS results in a vulnerable structure, the pull tests are additionally performed to test the mechanical strength of core-offset SMS structures, and the result indicates that they can withstand at least 1.5% strain regardless of the offset amplitudes.

## 5.4. Summary

A high-sensitivity, easy-to-fabricate, and low-cost SMS sensor based on core-offset was developed and experimentally investigated for temperature and strain sensing. This sensor is implemented with a commonly used MMF and can be fabricated by a commercial arc fusion splicer.

The sensing characteristics of the SMS sensors with the core-offsets of 10, 15, 20, 25, and 30  $\mu\text{m}$  at the input and output SMF/MMF boundaries are investigated. The obtained maximal temperature and strain sensitivities are 13.92  $\text{pm}/^\circ\text{C}$  and  $-1.19 \text{ pm}/\mu\epsilon$ , which are  $\sim$ two times and  $\sim$ eight times the values of the aligned SMS sensor (5.83  $\text{pm}/^\circ\text{C}$  and  $-0.15 \text{ pm}/\mu\epsilon$ ), respectively. The results also indicate that the maximal sensitivities for both temperature and strain are obtained with the 20- $\mu\text{m}$  core offset, not the largest core offset of 30  $\mu\text{m}$ , which indicates the existence of a limit of the offset-induced sensitivity enhancement. In addition, both temperature and strain sensitivities—with the input core-offset SMS—are higher than those with the output core-offset SMS. Note that pull tests of the core-offset SMS structures are additionally performed, which indicates that they can withstand at least 1.5% of strain regardless of the offset amplitudes.

With its simplicity, cost efficiency, and robustness, this method will be a valuable tool for enhancing the sensitivities of SMS temperature and strain sensors in the future.



## 6. Multimode Fiber Imaging with Deep Learning

Multimode fiber imaging has attracted considerable attention recently due to the blossom of machine learning. It has been reported that applying machine learning techniques in MMF imaging significantly improves the practical usability of the MMF imaging system. However, this system still suffers from ambient perturbation, such as fiber deformation and temperature changes, as they change the transmission matrix of the MMF. Moreover, the neural networks are limited by the complexity of the images. In this chapter, an MMF imaging system combined with neural networks for image reconstruction is developed. Further, deep learning methods, like fully connected neural networks and convolutional neural networks, are tested to be robust to the thermal perturbations in MMF imaging. In the end, the reconstruction of natural images with different neural networks is investigated.

### 6.1. Multimode Fiber Imaging System

The MMF imaging system includes two main parts: experimental setup and deep learning. The former is for creating the dataset to train the neural networks, and the latter is for image reconstruction. Figure 6.1 illustrates the flowchart of the MMF imaging system with deep learning. The ground truth images are transmitted through an MMF, and the output speckle patterns are paired with the input ground truth images as the training dataset to train the neural networks for reconstructing the input images.

#### 6.1.1. Experimental Setup

The optical setup of an MMF imaging system is depicted in Fig. 6.2, and the related components are listed in Table 6.1. The laser beam of a 632.8 nm wavelength HeNe laser (HNLS008L-EC, Thorlabs) is coupled to an MMF with a 200  $\mu\text{m}$  core diameter and an NA of 0.39 (FT200UMT, Thorlabs). The input pattern displayed on a phase-only spatial light modulator (SLM, Holoeye PLUTO-VIS,  $1920 \times 1080$  pixels) is then demagnified and imaged on the entrance facet of the MMF through a  $4f$  imaging system composed of lens L1 and

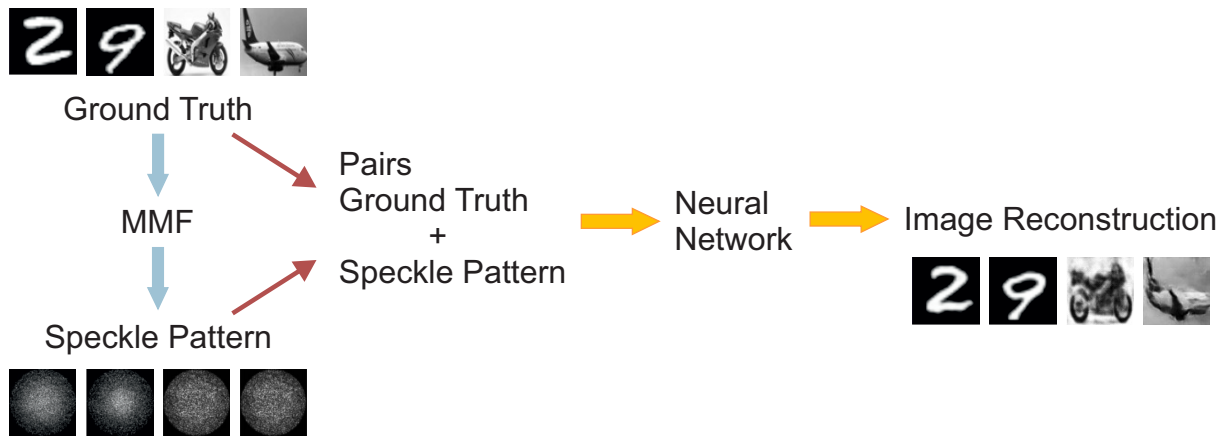


**Figure 6.1.:** Flowchart of MMF imaging system with deep learning.

Obj1. The speckle pattern from the output facet of the MMF is imaged onto a CMOS camera (DCC1545M, Thorlabs) by another  $4f$  imaging system.

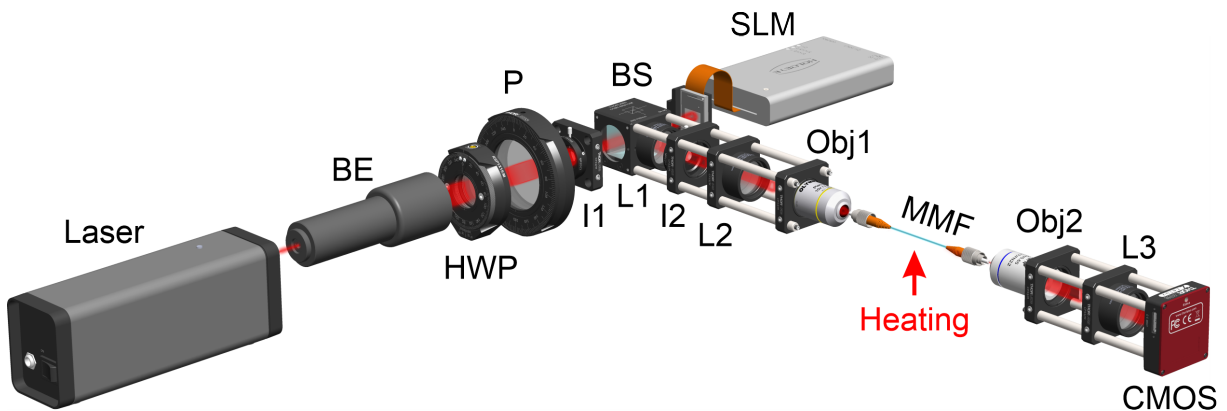


**Figure 6.2.:** Schematic diagram of the experimental setup; BE, beam expander; HWP, half-wave plate; P, polarizer; I1, iris; BS, beam splitter; SLM, spatial light modulator; L1, lens; I2, iris; L2, lens; Obj1, objective lens; MMF, multimode fiber; Obj2, objective lens; L3, lens; CMOS, CMOS camera.

The light source at 632.8 nm with a power of 0.8 mW is expanded and collimated by a beam expander (BE) and filtered by a half-wave plate (HWP) and a polarizer (P). The light is intensity regulated and linearly polarized. The beam diameter is controlled by an Iris (I1) and directed through a beam splitter (BS) on the spatial light modulator (SLM). The pattern created by the SLM is filtered by an Iris (I2) and imaged through the  $4f$  system (L1 and Obj1) at the MMF input. Then, the light travels along with the MMF, and at the output, another  $4f$  system (L1 and Obj2) magnifies the speckle pattern and projects it onto the CMOS camera. A heating device is used to generate the thermal perturbation during the

**Table 6.1.:** Components list of the MMF imaging system.

Components	Serial Number	Distributor
HeNe laser	HNLS008L-EC	Thorlabs
Beam expander (BE)	37-268	Edmund Optics
Half-wave plate (HWP)	WPH10M-633	Thorlabs
Linear polarizer	LPVISE200-A	Thorlabs
Iris diaphragms (I1 and I2)	SM1D12	Thorlabs
Cube beamsplitters (BS)	BS016	Thorlabs
Spatial light modulator (SLM)	PLUTO-VIS	Holoeye Photonics
Tube lens (L1, L2, and L3)	AC254-050-A-ML	Thorlabs
Objective 20x	HI Plan 11566070	Leica
Multimode fiber (MMF, 200- $\mu\text{m}$ )	FT200UMT	Thorlabs
Multimode fiber (MMF, 400- $\mu\text{m}$ )	FT400UMT	Thorlabs
Objective 40x	PLN40X	Olympus
CMOS camera	DCC1545M	Thorlabs

measurement.

The SLM used in the system is a phase-only liquid crystal SLM, which modulates and creates the desired shaped wavefront. This wavefront generates the desired images in the far field. To obtain these images, diffracting optical elements (DOEs) created by computer-generated holograms (CGHs) must be displayed on the liquid crystal screen of the SLM. The CGHs enable arbitrary removal or the addition of modes for properly transmitting the input images in the form of the DOEs, offering a high resolution and light efficiency simultaneously. The simplified working principle of the SLM is shown in Fig. 6.3. The far-field image will be coupled into the MMF.

### 6.1.2. Setup Calibration

The essential part of this setup is to couple the sharp far-field images created by the SLM into the MMF and obtain the speckle patterns at the output, which will contain the complete information of the images. Two critical variables need to be considered.

The first one is the spot size of the beam focused by the objective, which depends on its magnification and can be calculated as

$$s = \frac{4 M^2 \lambda f_L}{\pi D}, \quad (6.1)$$

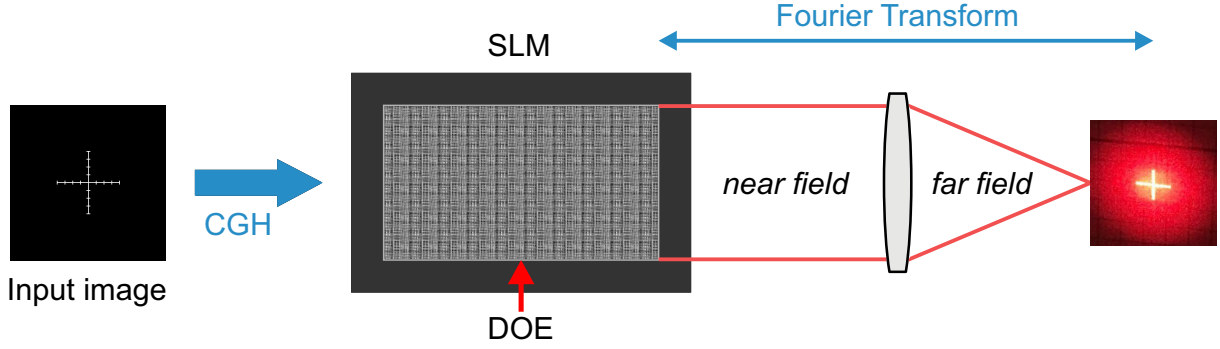


**Figure 6.3.:** Simplified working principle of the SLM. CGH, computer-generated hologram; SLM, spatial light modulator; DOE, diffracting optical element.

where  $M^2$  is the laser beam quality factor,  $\lambda$  is the wavelength,  $f_L$  is the lens focal length, and  $D$  is the input beam diameter at the lens. The beam quality factor of the beam reflected by SLM can be obtained by the beam parameter product (BPP), which is the product of a laser beam's divergence angle (half-angle  $\theta$ ) and the radius of the beam at its narrowest point (the beam waist  $w_0$ ) as

$$BPP = \theta w_0. \quad (6.2)$$

The BPP quantifies the quality of a laser beam and how well it can be focused on a small spot. A different and common beam quality expression is the  $M^2$  value. This value is a normalization of the BPP value, which is made against a diffraction-limited beam ( $BPP_0$ ) with the specific wavelength as

$$M^2 = \frac{BPP}{BPP_0} = BPP \frac{\pi}{\lambda}. \quad (6.3)$$

The divergence angle (half-angle  $\theta$ ) can be approximately obtained by

$$\theta = \arctan \frac{R(L)}{L}, \quad (6.4)$$

where  $R(L)$  is the beam radius at a certain distance, and  $L$  is considered as far field [166]. This beam radius can be measured, as shown in Fig. 6.4

The second variable is that the maximum incident angle at the end face of the MMF needs to be equal to or smaller than the acceptance angle of the MMF. The maximum acceptance angle is related to the NA of the MMF, as described in Section 2.1.1. To realize a high coupling efficiency, the NA of the objective ( $NA_{Obj}$ ) needs to be equal to or smaller than the NA of MMF ( $NA$ ). Assuming the beam entering the objective is collimated, the NA of the objective can be obtained by

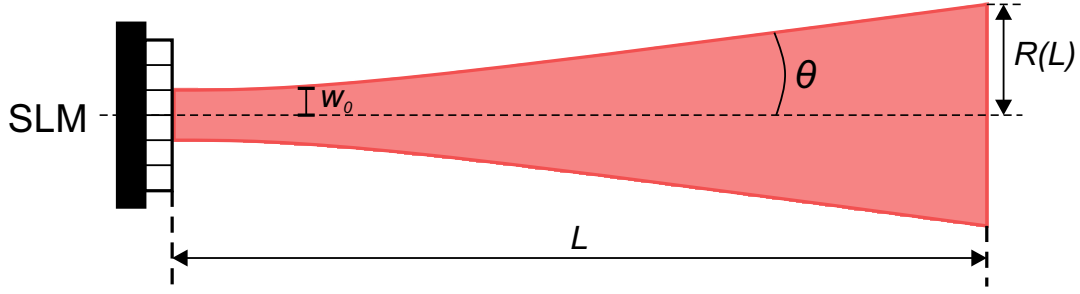


Figure 6.4.: Schematic diagram of beam quality measurement.

$$NA_{Obj} = \frac{D}{2f_{Obj}}, \quad (6.5)$$

where  $D$  is the beam diameter entering the objective and  $f_{Obj}$  is the focal length of the objective. Note that it is not critical that  $NA_{Obj} \leq NA$  because the beam cannot be ideally collimated. However, they should not be far from each other.

The divergence angle is measured at a distance  $L$  of 200 cm and an  $R(L)$  of 33 mm, which results in a half-angle  $\theta$  of 0.0165 rad. The beam waist ( $w_0$ ) of the beam incident onto the SLM is regulated by iris (I1) as 2.5 mm. With these parameters, the value of the beam quality factor  $M^2$  can be estimated as 204.7. Further, the magnifications of the objective lens can be determined according to the different core diameters of the MMFs. Note that, in this dissertation, the numerical apertures of the objective lens are 0.39 with different magnifications, and the numerical apertures of the MMFs are 0.4 with different core diameters. After the calibration of the setup, a coupling efficiency of >80% can be achieved, which satisfies the requirement for MMF imaging.

### 6.1.3. Multimode Fiber Imaging Data Acquisition

To obtain the MMF imaging data, the SLM and camera are integrated and controlled by a MATLAB script. The flowchart of the data acquisition is shown in Fig. 6.5. The DOEs of input images are computed by the software provided by Holoeye Photonics (HOLOEYE SLM Pattern Generator). All the generated DOEs are loaded to the SLM at once via MATLAB, and then each DOE is imaged on the SLM every 10 seconds. The CMOS camera captures the related speckle at the distal end of the MMF. Note that it is essential to correctly pair the generated DOE, input images, and output speckle. The MMF imaging setup needs to be stabilized before the image acquisition due to the mechanical strain of the components. As the limit of the computation power, a maximum of 25000 images can be loaded at once. The measurement of 5000 images takes  $\sim 2$  hours.

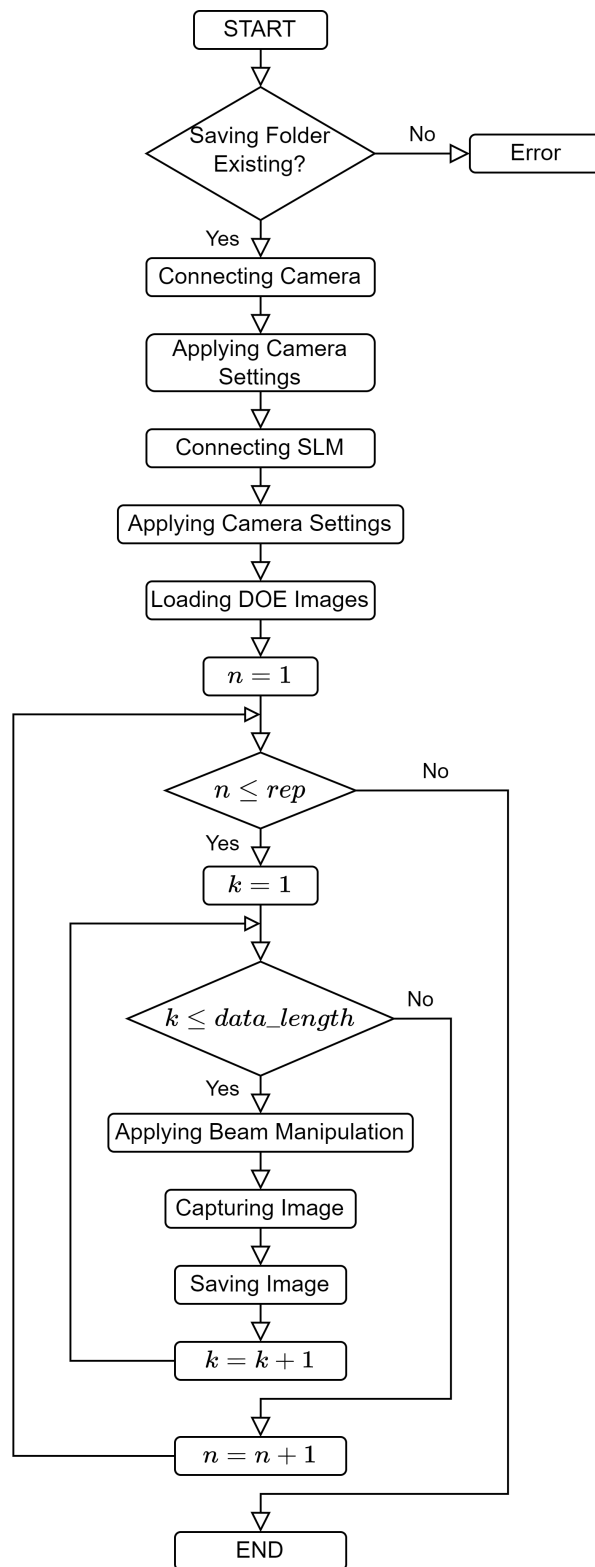


**Figure 6.5.:** Flowchart of the multimode fiber imaging data acquisition via MATLAB.

### 6.1.4. Deep Learning Architectures

Deep learning has skyrocketed in the past few years due to the astonishing improvement in computational power and advances in neural network architectures. Almost all deep learning neural networks stem from two types of networks: convolutional neural networks (CNNs) and fully connected neural networks (FCNNs).

A simple CNN is a sequence of layers, and three main types of layers are used to build CNN architecture: convolutional layer, pooling layer, and fully connected layer. An FCNN consists of a series of fully connected layers that connect every neuron in one layer to every neuron in the other layer, which has an advantage in that there is no need to make particular assumptions about the input.

#### Convolutional Layers

The convolutional layer is the core building block of a CNN, which carries the main computational load of the network. A convolution is effectively a sliding dot product between two matrices, where the kernel shifts through the whole image, repeating the same dot product operation, as shown in Fig. 6.6(a). Note that the kernel must have the same number of channels as the input images. Convolution is the process of placing a kernel on the top left corner of an image, multiplying kernel values by the pixel values and adding the results, moving the kernel to the right by one pixel at a time, and repeating this process. When the kernel moves to the top right corner, it moves down by one pixel and restarts the process from left to right. The complete process ends when the kernel moves to the bottom right corner of the image. In Fig. 6.6(a), after applying a  $2 \times 2$  kernel to a  $3 \times 3$  image, a  $2 \times 2$  image is obtained as the output. In addition, the number of weights per layer is much smaller, which benefits the possibility of having high-dimensional inputs, such as images.

#### Pooling Layers

The pooling layer performs downsampling to reduce the spatial dimensions of the input. Therefore, it reduces the number of learning parameters in the network, i.e., the learning time and computation. As the feature map produced by the convolutional layers is location-dependent, it can severely diminish the performance of the network. However, the pooling layer summarizes the features present in a region of the feature map generated by a convolutional layer, which enables further performance to be conducted on the pooling-layer-summarized features. With this, the network can be more robust to variations in the positions of the features in the input images. The most popular pooling is max pooling, which selects the maximum value from the region of the feature map covered by the filter. After the max pooling layer, the feature map only contains the most prominent features of

the previous feature map. In Fig. 6.6(b), a  $2 \times 2$  filter with a stride of 2 returns the maximum values while sliding through the feature map.

### Fully Connected Layers

Fully connected layers in a neural network connect every neuron in one layer to every neuron in the next layer, as shown in Fig. 6.6(c). It shows all the possible connections (layer to layer), where every input neuron influences every output neuron. However, not all the weights affect all output neurons. In Fig. 6.6(c), the red lines represent that an output neuron is calculated using all the input neurons with their weights. The value of an output neuron is the dot product between the input vector and a row of the weights matrix. The fully connected layer can be mathematically expressed as the neuron applies a linear transformation to the input vector through a weights matrix, and then a non-linear transformation is applied to the product through a non-linear activation function

$$y_{jk}(x) = f \left( \sum_{i=1}^n w_{jk} v_i + b_{j0} \right), \quad (6.6)$$

where  $v_i$  is the input vector,  $W_{jk}$  is the weights matrix, and  $b_{j0}$  is the bias term that can be added inside the non-linear activation function  $f$ , which wraps the dot product between the input of the layer and the weights matrix of that layer.

## 6.2. Multimode Fiber Imaging Reconstruction: Handwritten Digits

Two neural network architectures, based on U-Net and FCNN, are used in this dissertation. The U-Net is a CNN architecture first developed in 2015 to tackle biomedical image segmentation tasks, which has recently been used for MMF image reconstruction [167]. The architecture consists of a contracting and an expanding path, also called an encoder and a decoder path, as shown in Fig. 6.7. The encoder, a traditional stack of convolutional and max pooling layers, is used to capture the context of the image. The decoder is used for precise localization using transposed convolutions. Each blue box is a regular convolutional block. In the encoder, the size of the image reduces gradually with the downsampling while the depth gradually increases. Consequently, the network learns the context in the image but loses the localization information. In the decoder, the size of the image gradually increases with the depth decreases, which, intuitively, recovers the localization information by applying up-sampling. To combine the feature extraction with the location, the feature

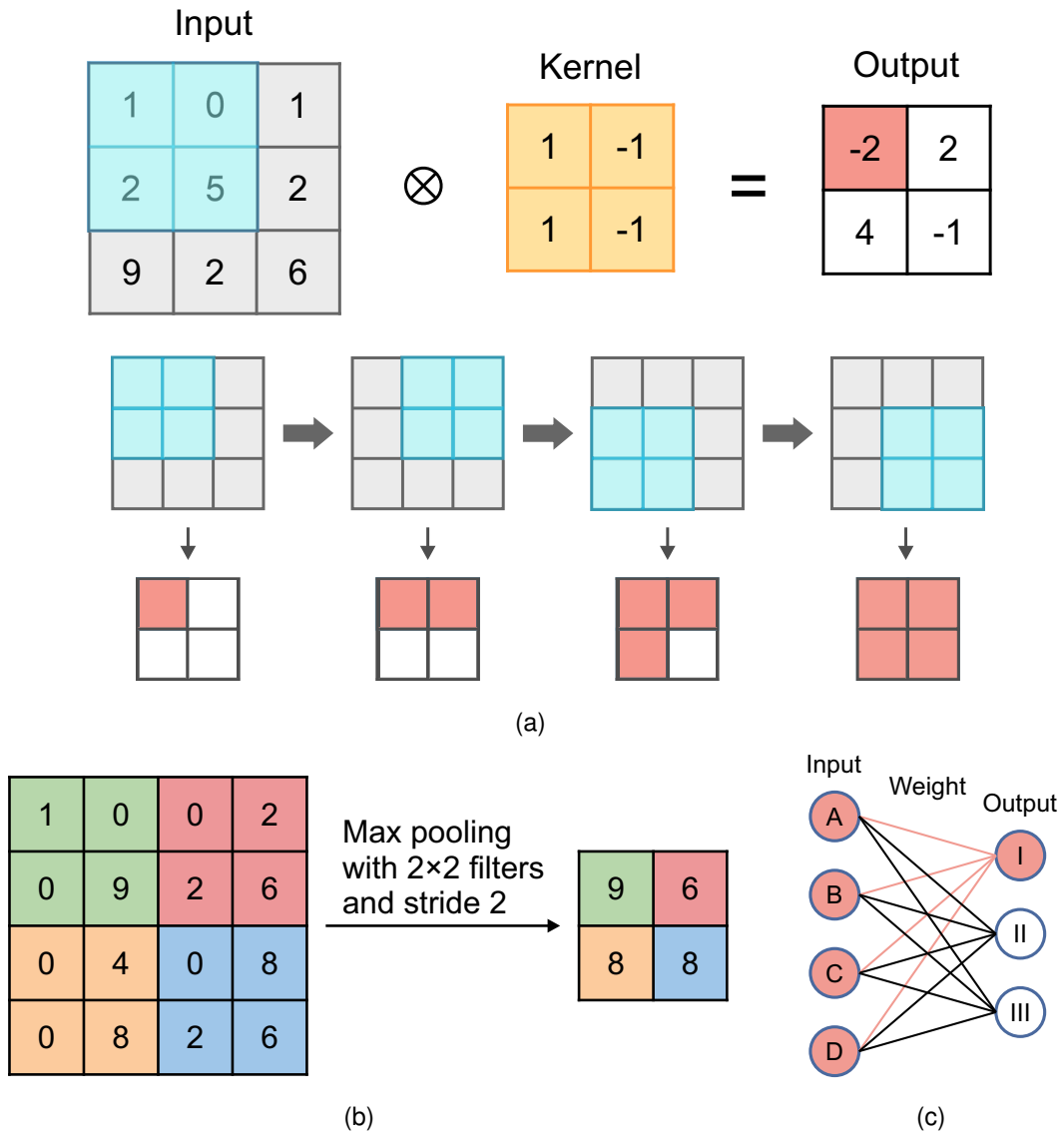


**Figure 6.6.:** Machine learning basics: (a) illustration of convolution operation (a 2x2 kernel applied to a 3x3 image, resulting in a 2x2 image), (b) max pooling operation, (c) a fully connected layer.

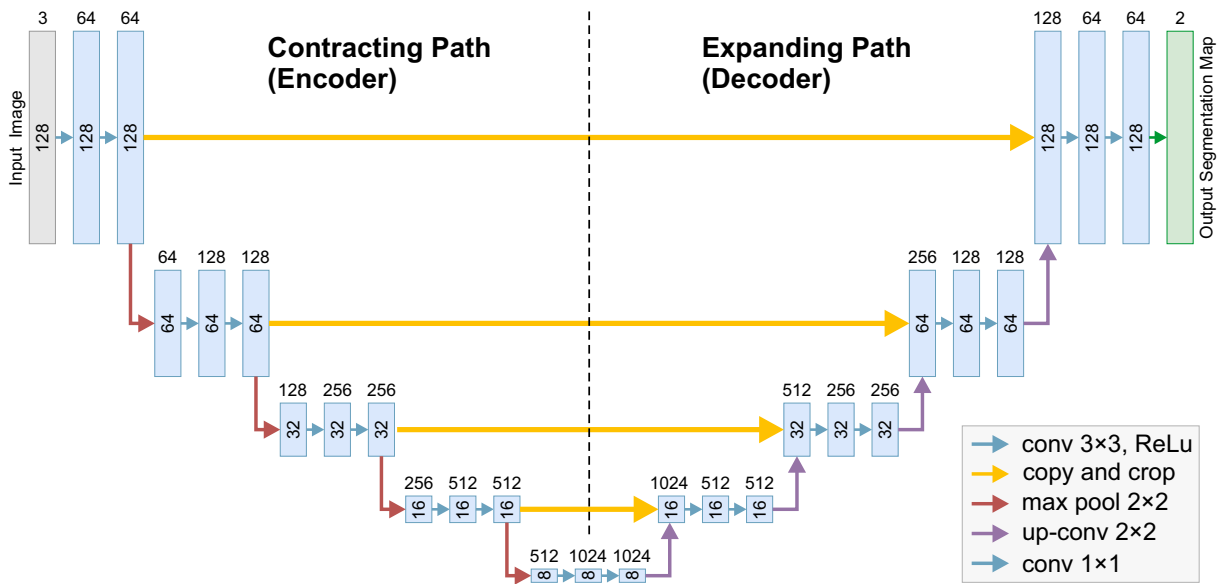


Figure 6.7.: Original U-Net architecture.

maps in the contracting path get concatenated at the same level as the feature maps in the expanding path.

### 6.2.1. Neural Networks

The CNN used in this dissertation is optimized based on the original U-Net, and the detailed architecture is depicted in Fig. 6.8. This CNN consists of 18 convolutional layers with a  $3 \times 3$  kernel for each layer, starting at the input layer for the speckle image. Each convolutional layer in the encoder path is followed by a nonlinear activation function (ReLu) and a max pooling operation with a stride of 2 for down-sampling. In the decoder path, transposed convolutional layers are used instead of max pooling layers for up-sampling.

The FCNNs are the most elementary neural network architectures for machine learning. The FCNNs have been used for MMF image reconstruction in early time [168–170], but the performance was restrained due to the limited computational power. In this dissertation, a simple FCNN is implemented, as shown in Fig. 6.9. Each input  $112 \times 112$  image is flattened ( $112 \times 112 = 12544$  nodes) and fed into the neural network. The first fully connected layer of 784 nodes transforms the input to the 784 output with a sigmoid activation function and a dropout regularization. The second fully connected layer repeats the process. The result from the output layer, which has 784 nodes, is reshaped into a  $28 \times 28$  image that can be compared to the ground truth.

## 6.2. Multimode Fiber Imaging Reconstruction: Handwritten Digits

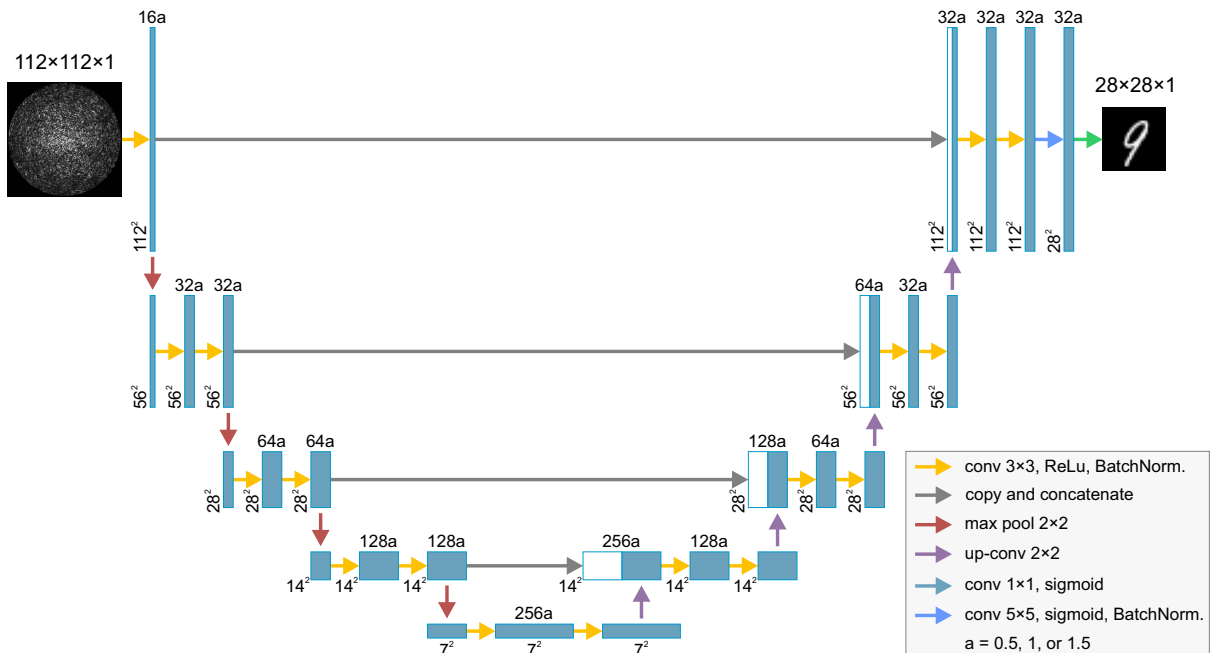


**Figure 6.8.:** The optimized U-Net architecture.

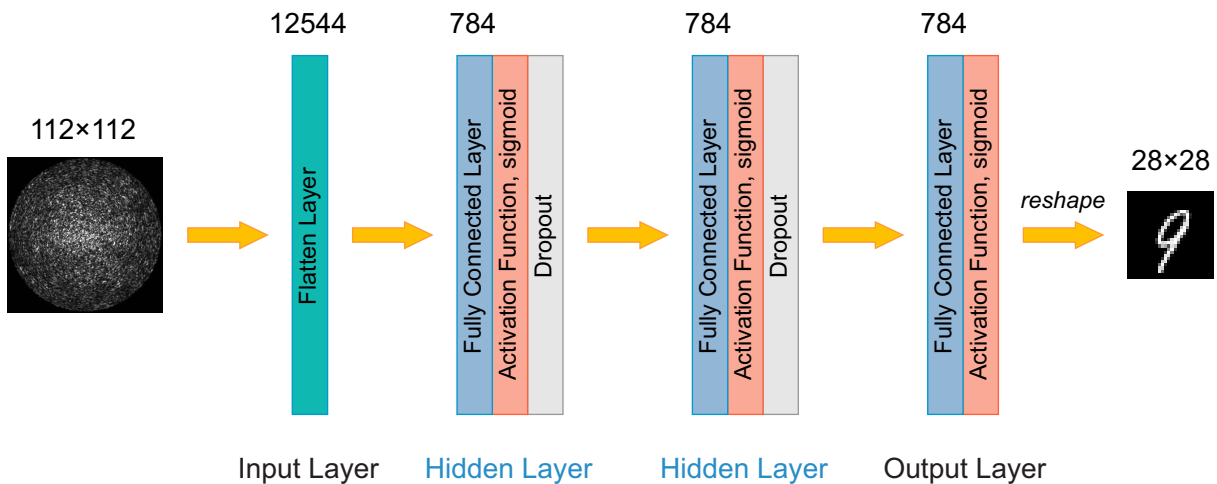


**Figure 6.9.:** The architecture of the fully connected neural network (FCNN).

Both neural networks were trained using Adam optimization with a batch size of 256 images. Besides, an early stopping condition was added to shorten the training time. It was found that batch-normalization regularization was crucial for the performance of the CNN, while dropout regularization functioned better for the FCNN. Therefore, batch normalization and dropout were applied in the CNN and FCNN, respectively. The objective functions used to compare the output of neural networks against ground truth (MNIST digits in this

experiment)

The objective function, i.e., the Structural Similarity Index (SSIM), was used to compare the output of neural networks against ground truth (MNIST digits in this experiment), which is a commonly used perceptual metric based on visible structures in the images [171]. It is defined as

$$SSIM(x, y) = [l(x, y)]^\alpha \cdot [c(x, y)]^\beta \cdot [s(x, y)]^\gamma, \quad (6.7)$$

where  $x$  and  $y$  are two images being compared,  $l(x, y)$  is the luminance comparison function,  $c(x, y)$  is the contrast comparison function,  $s(x, y)$  is the structure comparison function, and  $\alpha > 0$ ,  $\beta > 0$ , and  $\gamma > 0$  denote the relative importance of each of the metrics. Hence, the SSIM is a combination function that yields the similarity index value, which combines all these comparison functions on different aspects.

The luminance comparison function is described as

$$l(x, y) = \frac{2 \mu_x \mu_y + C_1}{\mu_x^2 + \mu_y^2 + C_1}, \quad (6.8)$$

where  $\mu_x$  and  $\mu_y$  are the luminance measured by averaging over all the pixel values in images  $x$  and  $y$ , given as

$$\mu_x = \frac{1}{N} \sum_{i=1}^n x_i \quad (6.9)$$

and

$$\mu_y = \frac{1}{N} \sum_{i=1}^n y_i, \quad (6.10)$$

where  $x_i$  and  $y_i$  are the  $i$ -th value of the images  $x$  and  $y$ , respectively. Furthermore, the images  $x$  and  $y$  have the same total number of pixel values ( $N$ ). The  $C_1$  is a constant to ensure stability when the denominator becomes 0, given by

$$C_1 = (K_1 L_d)^2, \quad (6.11)$$

where  $L_d$  is the dynamic range for the pixel values, and  $K_1$  is a normal constant. In our calculation, we set  $L_d$  as 1 and  $K_1$  as 0.01.

The contrast comparison function is defined as

$$c(x, y) = \frac{2 \sigma_x \sigma_y + C_2}{\sigma_x^2 + \sigma_y^2 + C_2}, \quad (6.12)$$

where  $\sigma_x$  and  $\sigma_y$  are the contrast measured by taking the standard deviation of all the pixel values in images  $x$  and  $y$ , given as

$$\sigma_x = \left( \frac{1}{N-1} \sum_{i=1}^n (x_i - \mu_x)^2 \right)^{1/2} \quad (6.13)$$

and

$$\sigma_y = \left( \frac{1}{N-1} \sum_{i=1}^n (y_i - \mu_y)^2 \right)^{1/2}. \quad (6.14)$$

Same as the  $C_1$ ,  $C_2$  is also a constant, given by

$$C_2 = (K_2 L_d)^2, \quad (6.15)$$

where  $K_2$  is a normal constant as  $K_1$ .

The structure comparison function is expressed as

$$s(x, y) = \frac{\sigma_{xy} + C_3}{\sigma_x \sigma_y + C_3} \quad (6.16)$$

with

$$\sigma_{xy} = \frac{1}{N-1} \sum_{i=1}^n (x_i - \mu_x)(y_i - \mu_y). \quad (6.17)$$

Finally, to simplify the Eq. 6.7, we set  $\alpha = \beta = \gamma = 1$ ,  $C_3 = C_2/2$ ,  $K_1 = 0.01$ ,  $K_2 = 0.03$ , and  $L_d = 1$ , the SSIM can be expressed as

$$SSIM(x, y) = \frac{(2\mu_x\mu_y + 10^{-4})(2\sigma_{xy} + 9 \times 10^{-4})}{(\mu_x^2 + \mu_y^2 + 10^{-4})(\sigma_x^2 + \sigma_y^2 + 9 \times 10^{-4})}. \quad (6.18)$$

When train the neural networks, the SSIM loss function is defined as

$$Loss_{SSIM} = 1 - SSIM. \quad (6.19)$$

### 6.2.2. Image Reconstruction through Multimode Fibers

To verify the reconstruction performance of these two networks, the same MNIST dataset was employed for MMF imaging reconstruction. The output speckles (5000 images) were experimentally collected with a 400- $\mu\text{m}$  core diameter MMF using the setup in Fig. 6.2. Then, a dataset of 5000 pairs (input MNIST digits images and output speckle images) was used to train the neural networks, which was divided into two parts: the training dataset (4750 pairs) and the validation dataset (250 pairs). The training was conducted on the same computer (NVIDIA DGX Station A100 Version 5.0.5, GNU/Linux 5.4.0-80-generic

x86\_64). Both networks were trained using the same dataset. The results of MMF imaging reconstruction for ten representative images (digits 0 to 9) from the validation dataset are shown in Fig. 6.10.

The trained FCNN and U-Net both can reconstruct from the speckles to ground truth with remarkable fidelity, as shown in Fig. 6.10(a), 6.10(c), and 6.10(d). It is clear that both neural networks performed excellently on MMF imaging reconstruction, but the SSIM of FCNN is slightly higher than that of U-Net. Compared to U-Net, the architecture of FCNN is much easier, and the training time of FCNN is much less than U-Net for the same amount of epochs. Besides, the implementation difficulty of FCNN is much lower than U-Net, which means it is easy to modify the FCNN, e.g., for different image sizes. Therefore, in the following, we focus on using FCNN; however, the U-Net will also be used as a comparison.

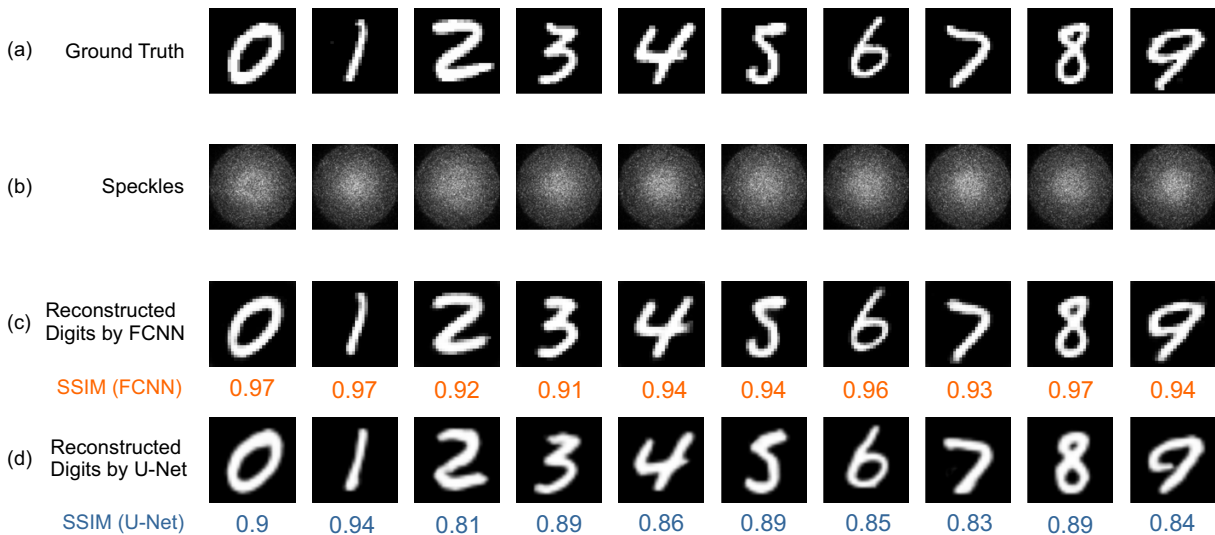


**Figure 6.10.:** Demonstration of MMF imaging reconstruction on MNIST dataset with a 400- $\mu\text{m}$  core diameter MMF. (a) Representative samples of  $28 \times 28$  ground truth images. (b) The corresponding output speckles ( $112 \times 112$ ) collected by the setup in Fig. 6.2. (c) Reconstructed  $28 \times 28$  images (digits) produced by FCNN and the SSIM related to the ground truth are shown below each reconstructed image. (d) The same images reconstructed by U-Net and its SSIM.

### 6.2.3. Imaging Reconstruction under Thermal Perturbation

Multimode fiber imaging is very sensitive to ambient changes, and the most common two factors are geometric deformations and temperature perturbations. A detailed study of bending in MMF imaging can be found in [141]. However, multimode fiber imaging still suffers from temperature perturbations as it is not avoidable. For example, when using MMF-based endoscopy during medical operations, the room temperature and organ tem-

perature are different, and this temperature change will undoubtedly influence the quality of MMF imaging. In this section, multimode fiber imaging with temperature perturbations will be studied.

The speckle acquisition was conducted using the setup shown in Fig. 6.2 in the temperature range of 25 to 75°C. The MMF was heated constantly during the speckle acquisition. The transmission characteristics of MMF drift over time, which may degrade the reconstruction quality. These temporal changes can be caused by thermal and mechanical perturbations. To minimize these changes in MMF itself over time, the speckles were acquired at 25°C (acquisition 1), then acquired at 30°C (acquisition 2), and the speckles were collected again at 25°C. The process of speckle acquisition is illustrated in Fig. 6.11. As the whole process takes a few days to complete, reducing the environmental influence in this way is possible. For example, the neural network is trained using the mixed dataset of acquisitions 1 and 3 (both at 25°C) and then tested on the speckles collected at 30°C (acquisition 2).

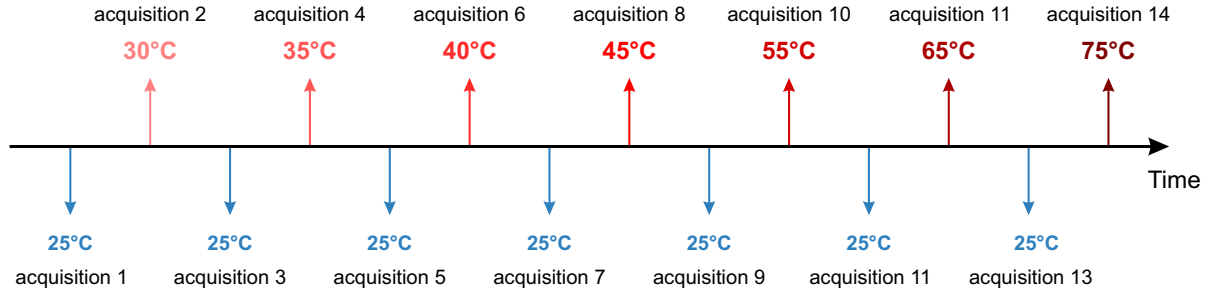


**Figure 6.11.:** Speckle acquisitions at different temperatures with time.

As the speckle changes drastically caused by temperature perturbations, the SSIM method is not ideal for evaluating the similarity between two speckle images. Here, another method, the Mean Square Error (MSE), is introduced to compare two speckle images generated with the same input digit, which is defined as

$$MSE = \frac{1}{MN} \sum_{i=1}^M \sum_{i=1}^N [X(m, n) - Y(m, n)] . \quad (6.20)$$

where  $X$  and  $Y$  are the two images with  $m \times n$  pixels. Figure 6.12 shows the speckle changes (with a 200- $\mu\text{m}$  core diameter MMF) at different temperatures and the corresponding MSE compared to the speckle acquired at 25°C, which indicates that the speckle changes drastically when the temperature increases from 25 to 75°C.

To quantitatively explain the MSE values, a simulation is performed. Random noises, i.e., related to different MSE values, are applied to the speckle patterns collected with a 200- $\mu\text{m}$  core diameter MMF at 25°C to generate the simulated noised datasets, and the FCNN and U-Net are both trained with simulated datasets.

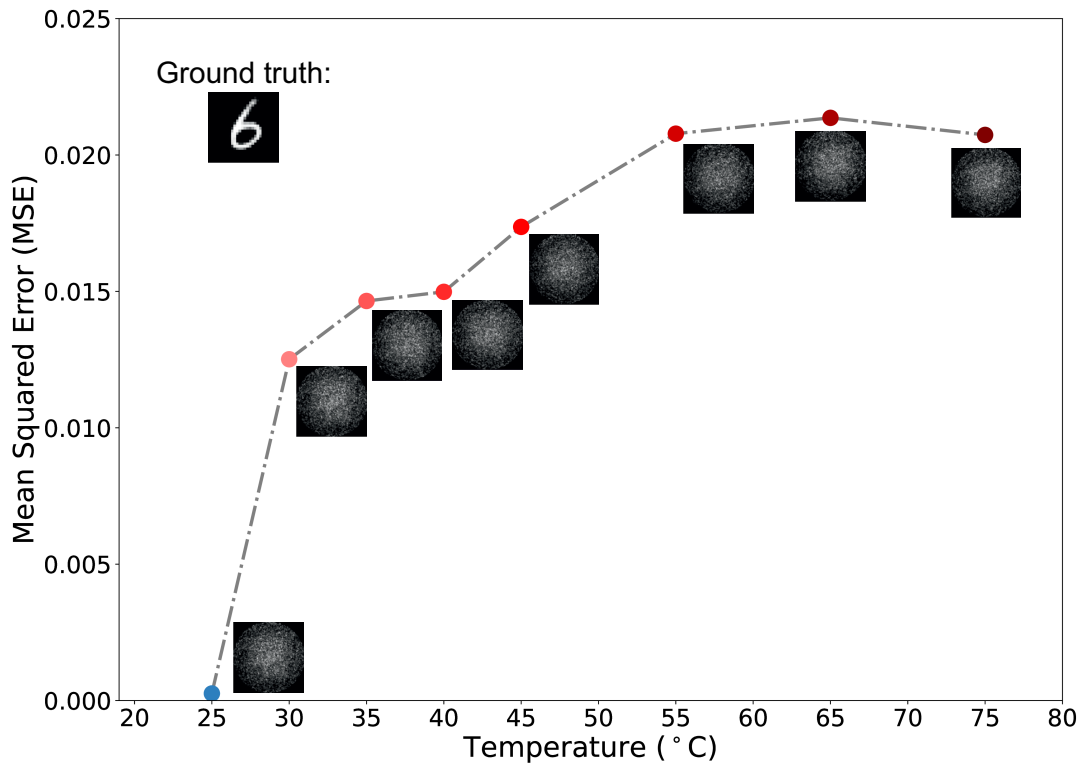


**Figure 6.12.:** Speckle patterns of the ground truth digit 6 (acquired with a 200- $\mu\text{m}$  core diameter MMF) at different temperatures with corresponding MSE compared to that acquired at 25°C.

First, the FCNN is trained, and the results are shown in Fig. 6.13. In general, when no noise is applied, the FCNN can reconstruct the image with remarkable fidelity. With noise, the reconstruction fidelity gradually drops, and from the MSE value of 0.0332, the performance of the FCNN is no longer promising, especially for relatively complex digits like 4, 7, and 9. It also proves that the neural network performance in MMF imaging is affected by image complexity. The results indicate that the FCNN can only reconstruct the images within a certain level of scrambled speckle patterns.

As the MSE values in Fig. 6.13 are smaller than 0.0332, which assumes that the FCNN may reconstruct the digits with promising fidelity. Therefore, the FCNN is trained with the measured data acquired with a 200- $\mu\text{m}$  core diameter MMF at different temperatures. Figure 6.14 shows the results of MMF imaging reconstruction at different temperatures for ten representative images (digits 0 to 9) from the validation dataset. The FCNN recovers the ground truth image with promising fidelity up to 45°C (MSE 0.0174), while the fidelity drops drastically when the temperature increases to 75°C. It is unsurprising that, as shown in Fig. 6.12, the speckle is scrambled strongly since the temperature reaches 55°C. These results also agree with the simulation results shown in Fig. 6.13.

Furthermore, the same simulation is carried out using U-Net, and the results are shown in Fig. 6.15. Same as the FCNN, without noise, the fidelity of image reconstruction with U-Net is remarkable too. It clearly shows that, with noise, the U-Net generally performs better than the FCNN. For example, with an MSE value of 0.0332, which is nearly the limit for FCNN, U-Net can still revive the images with good fidelity. The largest MSE value is located at the MSE value of around 0.0214, according to Fig. 6.12; therefore, the U-Net is assumed to be robust to reconstruct the images. Consequently, U-Net is trained with the same measured data as the FCNN and Fig. 6.16 presents the results. It demonstrates that up to 75°C, U-Net still can yield high fidelity, which agrees with the simulation results. For example, for digit 6, at 75°C, the MSE of speckle changes is 0.0214 (according to Fig. 6.12), and the related SSIM of the reconstructed image is 0.71 (see Fig. 6.16). The MSE values of 0.0148 and 0.0332 correspond to the SSIM values of 0.81 and 0.60, respectively, as shown in Table 6.2. As  $0.0148 < 0.0214 < 0.0332$  and  $0.60 < 0.71 < 0.81$ , it leads to the conclusion that the measured results agree with the simulated results.

Comparing the quality of reconstructed images of the FCNN and U-Net reveals that image reconstruction through an MMF using neural networks, both the FCNN and U-Net, is remarkable. Both neural networks are robust to a certain level of thermal perturbation applied to the MMF imaging system; the images are reconstructed with great fidelity when the temperature increases from room temperature ( $\sim 25^\circ\text{C}$ ) to  $45^\circ\text{C}$ , but in the range of 45 to  $75^\circ\text{C}$ , the fidelity of FCNN drastically drops while U-Net still can revive the images with relatively high fidelity.

**Table 6.2.:** Comparison of MSE and SSIM of simulation and measurement results.

Target Image	Methods	MSE	SSIM
MNIST Handwritten Digit 6	Simulation (random noise applied)	0.0148	0.81
		0.0332	0.60
	Measurement (75°C)	0.0214	0.71



**Figure 6.13.:** MNIST digits reconstructed by a fully connected neural network (FCNN) with simulated noised datasets. The SSIM values indicate the similarities between reconstructed and ground truth images.



**Figure 6.14.:** MNIST digits reconstructed by a fully connected neural network (FCNN) at different temperatures (speckles acquired with a 200- $\mu\text{m}$  core diameter MMF). (a) shows the ground truth images, (b)-(i) represent the reconstructed images at different temperatures with the corresponding SSIM.

Applied MSE		0.0000	0.0037	0.0148	0.0332	0.0591	0.0924	0.1329	0.1811	0.2364	0.2991
(a)	Reconstructed digit 0										
	SSIM (U-Net)	0.90	0.90	0.86	0.75	0.65	0.45	0.37	0.50	0.44	0.43
(b)	Reconstructed digit 1										
	SSIM (U-Net)	0.95	0.92	0.81	0.61	0.58	0.41	0.33	0.24	0.31	0.29
(c)	Reconstructed digit 2										
	SSIM (U-Net)	0.92	0.89	0.86	0.76	0.59	0.53	0.59	0.46	0.37	0.43
(d)	Reconstructed digit 3										
	SSIM (U-Net)	0.88	0.86	0.76	0.71	0.49	0.46	0.46	0.43	0.42	0.39
(e)	Reconstructed digit 4										
	SSIM (U-Net)	0.88	0.85	0.78	0.70	0.59	0.52	0.41	0.47	0.43	0.31
(f)	Reconstructed digit 5										
	SSIM (U-Net)	0.94	0.92	0.83	0.70	0.61	0.52	0.50	0.45	0.41	0.23
(g)	Reconstructed digit 6										
	SSIM (U-Net)	0.93	0.90	0.81	0.60	0.57	0.40	0.47	0.35	0.44	0.30
(h)	Reconstructed digit 7										
	SSIM (U-Net)	0.89	0.86	0.77	0.64	0.52	0.32	0.32	0.28	0.24	0.31
(i)	Reconstructed digit 8										
	SSIM (U-Net)	0.96	0.94	0.88	0.78	0.73	0.65	0.57	0.47	0.42	0.36
(j)	Reconstructed digit 9										
	SSIM (U-Net)	0.94	0.95	0.88	0.74	0.71	0.56	0.60	0.48	0.41	0.30

**Figure 6.15.:** MNIST digits reconstructed by U-Net with simulated noised datasets. The SSIM values indicate the similarities between reconstructed and ground truth images.

(a)	Ground Truth										
(b)	Reconstructed at 25°C										
	SSIM (U-Net)	0.91	0.92	0.79	0.89	0.85	0.88	0.92	0.89	0.93	0.83
(c)	Reconstructed at 30°C										
	SSIM (U-Net)	0.81	0.97	0.73	0.87	0.77	0.82	0.71	0.90	0.88	0.83
(d)	Reconstructed at 35°C										
	SSIM (U-Net)	0.82	0.93	0.75	0.88	0.73	0.80	0.75	0.88	0.77	0.80
(e)	Reconstructed at 40°C										
	SSIM (U-Net)	0.76	0.90	0.69	0.86	0.82	0.80	0.71	0.80	0.77	0.74
(f)	Reconstructed at 45°C										
	SSIM (U-Net)	0.68	0.94	0.75	0.79	0.70	0.75	0.69	0.91	0.78	0.79
(g)	Reconstructed at 55°C										
	SSIM (U-Net)	0.56	0.79	0.63	0.79	0.60	0.75	0.64	0.85	0.73	0.63
(h)	Reconstructed at 65°C										
	SSIM (U-Net)	0.73	0.91	0.68	0.71	0.66	0.74	0.69	0.78	0.72	0.73
(i)	Reconstructed at 75°C										
	SSIM (U-Net)	0.78	0.85	0.60	0.68	0.72	0.68	0.71	0.70	0.78	0.70

**Figure 6.16.:** MNIST digits reconstructed by U-Net at different temperatures (speckles acquired with a 200- $\mu\text{m}$  core diameter MMF). (a) shows the ground truth images, (b)-(i) represent the reconstructed images at different temperatures with the corresponding SSIM.

### 6.2.4. Discussion

The average SSIM of the complete dataset versus the applied MSE value in the simulation is shown in Fig. 6.17(a), and the average SSIM versus temperature is shown in Fig. 6.17(b). In the simulation, FCNN leads to a lower SSIM than U-Net with applied noise. The same trend also occurs in the measurement, but in the temperature range of 25 to 35°C, FCNN performs slightly better than U-Net. It might be caused by the instability in the speckles over acquisition. One is that besides the thermal perturbation during the experiment, the changes in the ambiance and MMF itself may contribute to additional distortion in the speckles. Another possibility is that, due to the thermo-optic effects, thermal expansion, and photoelastic effects, the temperature increase leads to the core diameter expansion and length increasing, contributing to the speckle changes. These phenomena may partially explain the difference between simulation and measurement results.

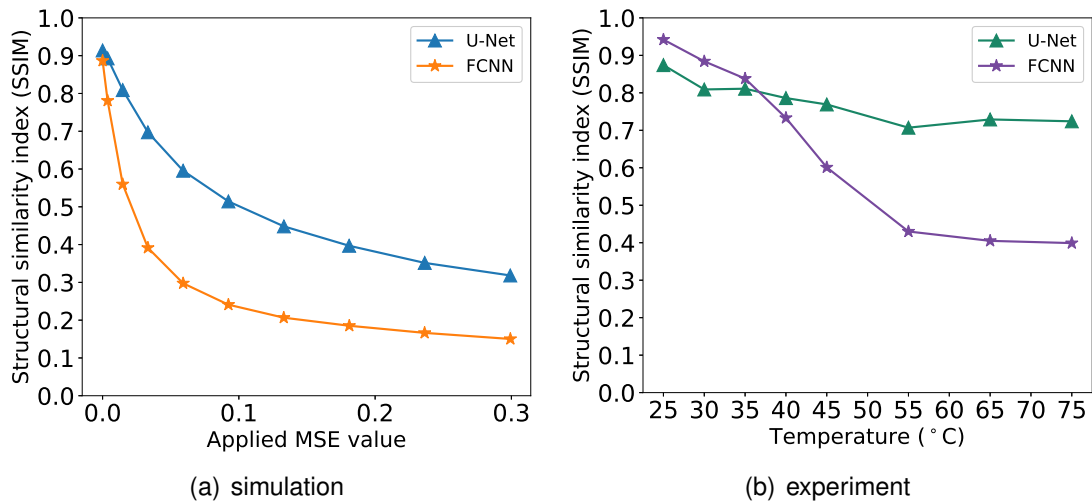


**Figure 6.17.:** Average SSIM versus (a) applied MSE values in simulation and (b) temperature changes in experiment.

## 6.3. Multimode Fiber Imaging Reconstruction: Natural Images

As the complexity of the images limits the practical implementation of MMF imaging, the reconstruction of natural images transmitted through an MMF is investigated by fine-tuning different neural networks. The original natural image dataset contains 6899 images from eight distinct classes: airplane, motorbike, person, cat, flower, car, fruit, and dog. By data

augmentation, i.e., rotation, an input dataset of 10238 images is created, and the speckle patterns are collected using the same setup. As the size of the ground truth image is  $64 \times 64$ , a 400- $\mu\text{m}$  core diameter MMF is used to guarantee coupling efficiency. The size of the collected speckle image is  $112 \times 112$ . A dataset of 10238 pairs of ground truth and speckle images is created and divided into training and validation datasets with a ratio of 19:1, resulting in 9726 pairs for training and 512 pairs for testing.

### 6.3.1. Multi-Hidden-Layer Fully Connected Neural Network

The proposed FCNN is proven to be able to revive the MNIST handwritten digits with high fidelity. Therefore, here, it is also used to reconstruct natural images. As the proposed FCNN is optimized for the MNIST dataset, fine-tuning the network for the natural image dataset is necessary. The FCNN is determined to be trained using Adam optimization with a batch size of 256 images, and early stopping is implemented at 100 epochs after the validation loss stops improving. The learning rate is 0.0001, and the objective function is MSE.

The reconstruction results of the proposed FCNN (2 hidden layers) are shown in Fig. 6.18(d), which shows the shapes of the ground truth images but not the details. The SSIM values are not as high as those of the MNIST dataset but are promising. Furthermore, the effectiveness of the number of layers is investigated, in particular, testing the same architecture of FCNN with one hidden layer and three hidden layers. The image reconstructions of 1-hidden-layer and 3-hidden-layer FCNN are presented in Fig. 6.18(c) and Fig. 6.18(e). The reconstructed images of 1-hidden-layer FCNN contain the most details and also have better SSIM. The result of the 2-hidden-layer FCNN is less noisy than that of the 1-hidden-layer FCNN but is more blurry. It is the same for the 3-hidden-layer FCNN; the results are less noisy but more blurry than the 2-hidden-layer model. The results show that adding hidden layers in the FCNN does not improve the reconstruction accuracy.

Figure 6.19 shows the MSE losses of multi-hidden-layer FCNNs calculated by objective function over the training and testing datasets. Both training loss and validation loss of 1-hidden-layer FCNN are lower than those of 2-hidden-layer or 3-hidden-layer FCNN. It indicates that more hidden layers do not lead to lower MSE loss but increase the training time as more parameters are added to the model.



**Figure 6.18.:** Natural images reconstructed by multi-hidden-layer fully connected neural network (FCNN): (c) 1-hidden-layer FCNN, (d) 2-hidden-layer FCNN, and (e) 3-hidden-layer FCNN. The SSIM values indicate the similarities between reconstructed and ground truth images.

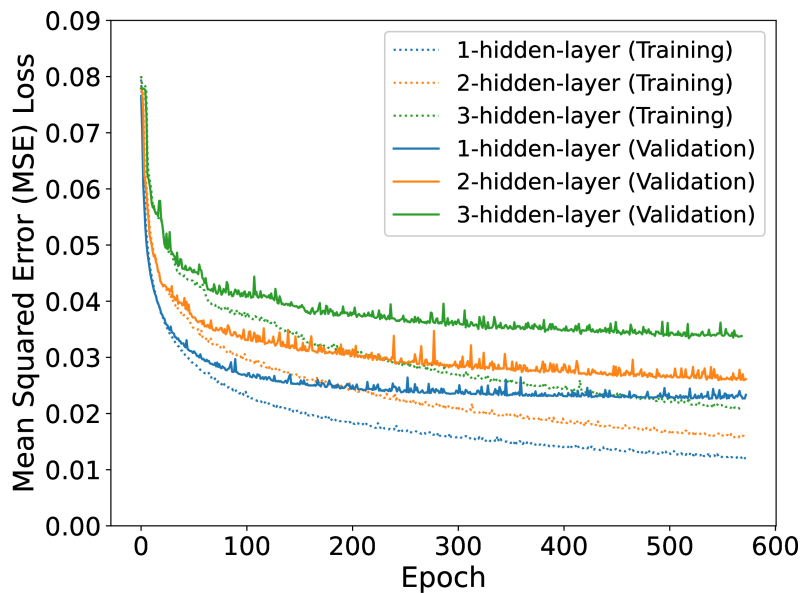


**Figure 6.19.:** Training (dotted line) and validation (solid line) losses as a function of the number of epochs for multi-hidden-layer FCNN: 1-hidden-layer (blue), 2-hidden-layer (orange), and 3-hidden-layer (green).

Besides the MSE loss function, the SSIM loss function is also tested, and these two loss functions deliver comparable reconstruction qualities. Therefore, the MSE loss function is still used in the MMF imaging system.

### 6.3.2. U-Net

The U-Net is widely used in machine-learning-based medical image classification and segmentation. It is proven to be more robust to thermal perturbation in MNIST digits reconstruction. Therefore, here, U-Net is also applied to the reconstruction of natural images. The architecture of U-Net is the same as Fig. 6.8, but the training parameters of the network are optimized according to the size of the natural image. The U-Net is trained using Adam optimization with a batch size of 32 images, and early stopping is also included at 100 epochs after the validation loss stops decreasing. The learning rate is determined to be 0.0005, and the loss function is MSE, too. The reconstructed images are presented in Fig. 6.20. The SSIM values are comparable to the results of the FCNN, as the reconstructed images are more blurry and contain fewer details.

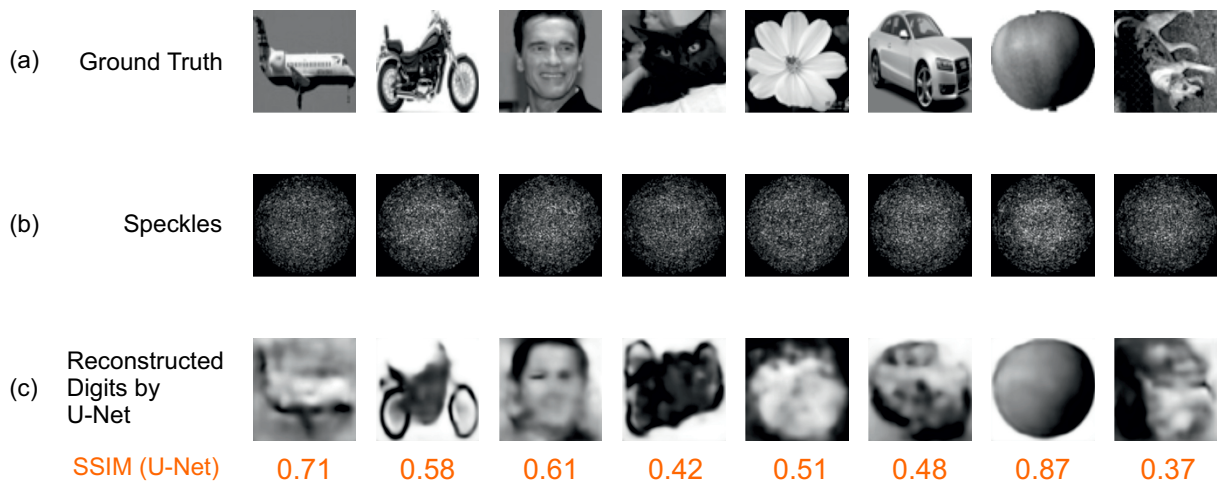


**Figure 6.20.:** Natural images reconstructed by U-Net. The SSIM values indicate the similarities between reconstructed and ground truth images.

### 6.3.3. Discussion

In this section, several architectures of neural networks are implemented for reconstructing natural images. Overall, all architectures are able to revive the general shapes of the ground truth images. With additional layers, i.e., deeper neural networks, the FCNN and U-Net can reduce the noise level and, conversely, also lose more details. Table 6.3 compares

**Table 6.3.:** Summary of average SSIM, training time, and the number of training parameters for different neural network architectures.

Architecture	Average SSIM	Training time (s)	Number of parameters
1-hidden-layer FCNN	0.63	1089	68157440
2-hidden-layer FCNN	0.57	1346	84934656
3-hidden-layer FCNN	0.46	1562	101711872
U-Net	0.54	1294	4407673

the average SSIM, the training time, and the total number of parameters of different architectures. It can be observed that the average SSIM decreases with more hidden layers in the FCNN. With more hidden layers, the total number of parameters certainly increases, resulting in a longer training time as they are proportionate. The U-Net needs relatively fewer training parameters but still requires longer training time. Additionally, other architectures of neural networks, e.g., Generative Adversarial Network (GAN), are also tested, but they do not provide significant improvement compared to the 1-hidden-layer FCNN. Therefore, the proposed 1-hidden-layer FCNN can reconstruct natural images with high fidelity compared to other architectures. This architecture is also faster and easier to adapt to other datasets.

## 6.4. Summary

A multimode fiber imaging system combined with deep learning is developed in this chapter. Two problems that limit the practical usability of MMF imaging are studied: thermal perturbation and reconstruction of natural images.

An MMF imaging setup with speckle acquisition is introduced. Two types of neural networks are exploited, i.e., fully connected neural networks and convolutional neural networks (U-Net). Both networks are first tested on the MNIST handwritten digits dataset. The reconstruction results show that both neural networks can reconstruct the MNIST handwritten digits with remarkable fidelity. Then, the influence of thermal perturbation on image reconstruction is simulated and verified experimentally. To apply the thermal perturbation, the MMF is heated from 25 to 75°C. The speckles at the output distal end of the MMF are collected at different temperatures. The experimental results are in good agreement with the simulated results. It shows that, up to a certain level of thermal perturbation, i.e., the temperature changes from 25 to 45°C in this work, both FCNN and U-Net are robust to the thermal perturbation. In the range of 25 to 35°C, the FCNN performs slightly better than the U-Net, and from 45 to 75°C, the U-Net can revive the digits with better fidelity compared to

the FCNN.

Moreover, the reconstruction of the natural images is also investigated with the proposed imaging system. The revival of the natural image is carried out with multilayer FCNN and U-Net. Compared to the convolutional neural network, i.e., U-Net, the proposed 1-hidden-layer FCNN has advantages like higher reconstruction fidelity, faster training time, and simpler neural network architecture.

This work may provide a guideline for implementing the MMF imaging system practically. For example, in the low-temperature range, like medical endoscopic imaging, the FCNN is preferred, as it performs faster than the U-Net with comparable fidelity. Nevertheless, U-Net may be favored in industrial scenarios, as a high-temperature range is usually needed. The reconstruction of the natural images with thermal perturbation needs to be investigated for future use.



# 7. Conclusion and Outlook

## 7.1. Conclusion

In this dissertation, fiber-optic multimode interference sensing and imaging are presented. Several MMI-based fiber sensors have been developed and studied for temperature and strain measurement, and further, an MMF imaging system with deep learning has been investigated. The temperature and strain sensitivities of the proposed sensors are significantly improved, and these sensors provide guidelines and possibilities for developing MMI-based fiber sensors for future studies. The MMF imaging system with deep learning is tested under a common and unavoidable influence, thermal perturbation, on image reconstruction by MMF imaging. Two neural networks are designed and adapted for the corresponding system, and the results show they are robust to thermal perturbation. This research promotes the practical usability of MMF imaging systems in various fields like medical endoscopic imaging and industrial applications.

In Chapter 1, a brief history of optical fibers is introduced first, and the development of optical fiber sensors and fiber-optic imaging is followed. The aims and objectives of this dissertation are pointed out, and the layout of this dissertation is given.

In Chapter 2, the fundamentals and state of the art of MMI-based fiber sensors and MMF imaging systems are presented. The related characteristics of the MMF, including the NA and the number of modes, are introduced. The sensing principle of the simplest structure to generate multimode interference, the so-called SMS structure, is described as the foundation of most MMI-based fiber sensors. Further, the current research status of MMI-based fiber sensors is summarized. The sensing principle and literature research indicate a fundamental discussion: whether the sensitivity is affected by the length of the MMF in the SMS structure. Besides, it also reveals that high-sensitivity and multi-parameter sensing are significantly needed. Three possibilities are suggested to enhance the performance of MMI-based fiber sensors, including new fiber sensor structures, new compensation methods, and new types of fibers. For MMF imaging, the traditional method to measure the TM of the MMF is introduced, which is relatively time-consuming and unstable to the ambient changes and deformation of the MMF. With the blossom of machine learning methods, MMF imaging combined with machine learning draws massive attention. The current evolution of applying machine learning to MMF imaging is studied. Its advantages, tolerant to

the deformation of the MMF, and drawbacks, the performance of neural networks limited by the complexity of the images, are summarized, which leads to two research topics: MMF imaging with deep learning under thermal perturbation and the reconstruction of natural images through an MMF.

In Chapter 3, a comprehensive characterization of standard MMF is conducted experimentally to evaluate the core diameter, NA, and length dependences of the strain and temperature sensitivities of a standard MMF-based SMS structure. The measurement results show that (i) a larger core diameter brings to higher temperature sensitivity and lower strain sensitivity (absolute value), (ii) higher NA does not affect the temperature sensitivity but results in higher strain sensitivity (absolute value), and (iii) longer MMF length leads to lower temperature sensitivity but does not influence the strain sensitivity. It is noticed that the strain sensitivities are relatively low during all the measurements. Subsequently, exploiting the low strain sensitivities, the standard SMS-based strain-insensitive temperature sensing is demonstrated. The mean temperature sensitivity is  $6.14 \text{ pm}/^\circ\text{C}$ , and its standard deviation is  $0.39 \text{ pm}/^\circ\text{C}$ . The findings will be of great significance for designing SMS structures, and strain-insensitive temperature sensing will be of practical use for its simplicity and cost efficiency.

In Chapter 4, according to the possibility summarized in Chapter 2 that the new type of fiber may enhance the performance of the MMI-based fiber sensors by increasing sensitivity and reducing crosstalk, a new specialty fiber, i.e., square-core fiber, is investigated. The SCF has a square-shaped silica core surrounded by circular polymer cladding. An SMS structure consisting of a segment of the SCF is fabricated and tested for temperature and strain sensing. The simulation of beam propagation in the SMS structure consisting of circular core and square-core fiber is carried out. The experimental results show that SCF is promising for sensing compared to other specialty fibers with circular cores. Similar to the standard MMF-based SMS structure, the strain sensitivity is extremely low compared to the temperature sensitivity. Therefore, it also has the potential to exhibit strain-insensitive temperature sensing. The obtained mean temperature sensitivity is  $-22.35 \text{ pm}/^\circ\text{C}$ , with a standard deviation of  $0.44 \text{ pm}/^\circ\text{C}$ , in the strain range of 0 to  $500 \mu\epsilon$ , which is  $\sim 3.5$  times higher than the sensitivity (absolute value) of a standard MMF-based configuration (in Chapter 2) under the same condition. This investigation proves that the new type of fiber may improve the sensitivity, and this study will also contribute to the design of strain-insensitive temperature sensors and the development of specialty fiber-based SMS structures in the future.

In Chapter 5, based on the conclusion in Chapter 2 that the new sensor structure has the potential to increase the sensitivity, a core-offset SMS structure is developed for temperature and strain sensing. This sensor consists of a standard MMF and can be easily fabricated using a commercial arc fusion splicer. Six samples, with the core offsets of 0

(aligned), 10, 15, 20, 25, and 30  $\mu\text{m}$ , are created, and their performances, with the core offsets at input and output SMF/MMF boundaries, are investigated. The obtained maximal temperature sensitivity is 13.92  $\text{pm}/^\circ\text{C}$ , which is  $\sim$ two times the value of the aligned SMS sensor, while the strain sensitivity is  $-1.19 \text{ pm}/\mu\epsilon$ , which is  $\sim$ eight times higher. The experimental results also show that both temperature and strain sensitivities—with the core offset at the input SMF/MMF boundary—are higher than those with the core offset at the output SMF/MMF boundary. As the maximal sensitivity for both temperature and strain are obtained with the 20- $\mu\text{m}$  core offset, not the largest core offset of 30- $\mu\text{m}$ , it reveals a ceiling of offset-induced sensitivity improvement. Additionally, pull tests of the core-offset SMS structures are carried out, and the results indicate that they can withstand at least 1.5% of strain regardless of the offset amplitudes. This study proved that the new structure is able to improve the sensitivity and will be a valuable method for enhancing the sensitivities of SMS temperature and strain sensors in the future, with the simplicity, cost efficiency, and robustness of this sensor configuration.

In Chapter 6, an MMF imaging system combined with deep learning is developed to study two factors that limit its practical usability. The experimental setup is built based on the SLM, the core component, illuminated by an expanded laser beam. The information of the images is carried by the reflected beam and coupled into an MMF. At the output distal end of the MMF, the speckle patterns are captured by a CMOS camera. Two neural networks are designed and adapted for image construction, i.e., fully connected neural networks (FCNN) and convolutional neural networks (U-Net). First, the MNIST handwritten digits dataset is reconstructed with both neural networks. The results show that both neural networks can revive the images with remarkable fidelity. Subsequently, the MMF is heated from 25 to 75 $^\circ\text{C}$  to apply the thermal perturbation to the MMF imaging system. Moreover, the speckles are collected at different temperatures. The reconstruction results of experimental data agree with the simulation, which shows that to a certain level of thermal perturbation, i.e., the temperature changes from 25 to 45 $^\circ\text{C}$  in this study, both FCNN and U-Net are robust to the thermal perturbation. The FCNN performs slightly better than the U-Net in the range of 25 to 35 $^\circ\text{C}$ , but from 45 to 75 $^\circ\text{C}$ , the U-Net can reconstruct the digits with better fidelity compared to the FCNN. Furthermore, the reconstruction of natural images, which are more complex than the MNIST handwritten digits, is also investigated with the same imaging system. Based on the FCNN, a multilayer FCNN is developed and tested on the revival of natural images. The results show that the proposed 1-hidden-layer FCNN is superior to the U-Net and other multilayer FCNNs due to the higher reconstruction fidelity, faster training time, and simpler network architecture. This study benefits the practical use of the MMF imaging system. Depending on the complexity of different applications, suitable neural networks can be employed. For example, in the low-temperature range, like medical endoscopic imaging, the FCNN is preferred due to the high fidelity with less training time.

The U-Net may be a better choice for industry, as a high-temperature range is usually needed, like oil prospecting.

## 7.2. Outlook

The improvement of the MMI-based sensor configurations presented in this dissertation includes enhanced sensitivities for temperature and strain sensing, easy-to-fabricate structures, and cost efficiency. A new specialty fiber, square-core fiber, is used, and its sensing ability, comparable to other specialty fibers, is proven. However, the characteristics of the square-core fiber still need to be well demonstrated. The sensing performance can be improved with a better understanding of the square-core fiber. To fabricate an SMS structure, it is critical that the end faces of the MMF are perfectly cleaved. Specialty fibers are usually made of uncommon materials, not silica. For instance, the cladding material of square-core fiber is hard-polymer, which cannot be spliced to the SMFs. Further, there is no matured technique to cleave the square-core fiber, and the imperfect end faces of the square-core fiber lead to a noisy transmission spectrum. It results in difficulty localizing the spectral dip/peak as the indicator to calculate the sensitivity. With the development of manufacturing, cleaving, and fiber-related accessories, specialty fibers will contribute significantly to the evolution of optical fiber sensors.

The MMI-based fiber sensors are very sensitive to ambient changes and deformation of the fibers, which leads to inaccurate sensitivity. For example, temperature changes cause the expansion of the fiber, resulting in changes in fiber length and core diameter, which influences temperature sensitivity. So reducing the crosstalk and the undesirable influence is crucial to boost the sensitivity accuracy. In Chapter 3, strain-insensitive temperature sensing is investigated, implying that a zero-strain sensitivity can be realized at a specific core diameter. The same goes for Chapter 4, which shows that square-core fiber exhibits strain-insensitive temperature measurement. In future studies, the core diameter dependence needs to be studied systematically, and it is necessary to explore different specialty fibers for the purpose of reducing crosstalk. As the square-core fiber has a square-shaped core, it is easier to apply a coating on the flat surfaces of the fiber core than on the circular-shaped core. Choosing specific materials may eliminate the crosstalk and increase the sensitivity.

The study of the core-offset SMS structure using standard MMF comprehensively presents the characteristics of this configuration, and the sensitivity is enhanced significantly. Considering the studies of specialty fibers and strain-insensitive temperature sensing, it motivates a possibility to combine the core-offset SMS structure with specialty fibers, which may boost the sensitivity and reduce the crosstalk simultaneously. With this, high-sensitivity multi-parameter sensing can be achieved with high accuracy.

The preliminary demonstration of the MMF imaging system combined with deep learning for image reconstruction under thermal perturbation shows that the neural networks are robust to the thermal perturbation applied to the MMF imaging system. It broadens the practical usability of MMF imaging systems. However, a wider temperature range cannot be tested due to the limit of the experimental conditions, as the large core diameter MMFs mostly have polymer claddings that cannot endure high temperatures. Using specialty MMF and investigating higher temperatures certainly will further expand the use of the MMF imaging system, for example, in industry. In general, reconstructing complex images, i.e., natural images, is still challenging. The complexity of the images limits the neural networks. With the evolution of deep learning techniques, this limit can be lifted in the near future. Besides, using the unique characteristics of specialty MMFs for imaging may contribute, too. As MMF sensing has been established for decades, and MMF imaging is developing rapidly, implementing sensing into the imaging system will be beneficial. For example, optical fiber-based medical endoscopes are widely used for surgeries, and measuring the temperature during the operation is vital. Other devices are usually needed to measure the temperature separately, and they cannot measure the temperature with the endoscopes in specific tissues or organs. If the endoscope can measure the temperature simultaneously with imaging, it will simplify the devices and can measure the temperature particularly. It is the future of multimode fiber.



# List of Symbols

$a$	fiber core radius
$b$	fiber cladding radius
$n_{co}$	refractive index of the MMF core
$n_{cl}$	refractive index of the MMF cladding
$\theta_{max}$	maximum acceptance angle
$n_0$	refractive index of surround
$N_m$	number of modes allowed to propagate in the optical fiber
$g$	refractive index profile parameter
$V$	normalized optical frequency, i.e., $V$ -number
$\lambda$	vacuum wavelength
$P_{out}$	power in the output SMF in the SMS structure
$A_m$	field amplitude determined by the modal overlap between the fundamental mode of the SMF and the concerned $m$ -th symmetric mode of the MMF
$\beta_m$	propagation constant of the $m$ -th mode
$\Psi_S$	fundamental modal field of the SMF
$w_s$	gaussian spot size of the mode in SMF
$a_S$	core radius of SMF
$V_S$	$V$ -number of the SMF
$a_M$	core radius of MMF
$\Psi_m$	modal field for the $m$ -th mode in an MMF
$A$	a constant
$k_0$	free-space wave number
$E_{IP}(\theta_x, \theta_y)$	image information carried by an input light wave
$E_{OP}(\xi, \eta)$	output light wave
$T(\xi, \eta; x, y)$	transmission matrix of the turbid medium
$T(\xi, \eta; x, y)^{-1}$	inversion of the Transmission matrix of the turbid medium
$\alpha_1$	thermal expansion coefficient of the MMF material

## List of Symbols

---

$\xi$	normalized thermo-optic coefficient of the MMF material
$T$	temperature
$\nu$	poisson ratio of the fiber
$p_e$	effective strain-optic coefficient
$\varepsilon$	strain
$R^2$	linear regression coefficients
$s$	spot size of the beam focused by the objective lens
$M^2$	laser beam quality factor
$f$	focal length
$D$	beam diameter
$BPP$	beam parameter product
$\theta$	laser beam's divergence angle (half-angle)
$w_0$	beam waist
$R$	beam radius
$y_{jk}$	non-linear activation function
$v_i$	input vector
$W_{jk}$	weights matrix
$b_{j0}$	bias term
$l(x, y)$	luminance comparison function
$c(x, y)$	contrast comparison function
$s(x, y)$	structure comparison function
$\mu$	luminance measured by averaging over all the pixel values in one image
$N$	total number of pixel values in one image
$C_1$	a constant
$L_d$	dynamic range for the pixel values
$K_1$	a normal constant
$\sigma$	contrast measured by taking the standard deviation of all the pixel values in one image
$C_2$	a constant
$K_2$	a normal constant
$C_3$	a constant

# List of Abbreviations

<b>SMF</b>	single-mode fiber
<b>FBGs</b>	fiber Bragg gratings
<b>LPGs</b>	long-period gratings
<b>SMS</b>	single-mode–multimode–single-mode
<b>MMI</b>	multimode interference
<b>MMF</b>	multimode fiber
<b>TM</b>	transmission matrix
<b>NA</b>	numerical aperture
<b>ITU-T</b>	International Telecommunication Union Telecommuni- cation Standardization Sector
<b>SI</b>	step-index
<b>GI</b>	graded-index
<b>RI</b>	refractive index
<b>TIR</b>	total internal reflection
<b>POF</b>	polymer optical fiber
<b>NCF</b>	no-core fiber
<b>FFT</b>	fast Fourier transform
<b>OSA</b>	optical spectrum analyzer
<b>ITO</b>	indium tin oxide
<b>RH</b>	relative humidity
<b>MMMF</b>	multimode microfiber
<b>MZI</b>	Mach–Zehnder interferometer
<b>FSR</b>	free spectrum range
<b>SMSMS</b>	SMF-MMF-SMF-MMF-SMF
<b>MSM</b>	MMF–SMF–MMF
<b>TCF</b>	twin core fiber
<b>TCSMF</b>	three-core single mode fiber
<b>SNS</b>	SMF-NCF-SMF
<b>HCF</b>	hollow core fiber
<b>HACF</b>	hollow annular core fiber

## List of Abbreviations

---

<b>PCF</b>	photonic crystal fiber
<b>SLM</b>	spatial light modulator
<b>DMD</b>	digital micromirror device
<b>BS</b>	beam splitter
<b>ANNs</b>	artificial neural networks
<b>DNNs</b>	deep neural networks
<b>CNN</b>	convolutional neural network
<b>VGG</b>	visual geometry group
<b>PCA</b>	principal component analysis
<b>SVM</b>	support vector machine
<b>SHL-DNN</b>	single hidden layer dense neural network
<b>SSIM</b>	Structural Similarity Index Measure
<b>FC</b>	full-connected
<b>OAM</b>	orbital angular momentum
<b>DSSIM</b>	structural dissimilarity index merit
<b>MSE</b>	mean squared error
<b>BLS</b>	broadband light source
<b>SCF</b>	square-core fiber
<b>BE</b>	beam expander
<b>HWP</b>	half-wave plate
<b>P</b>	polarizer
<b>I</b>	iris
<b>Obj</b>	objective lens
<b>L</b>	lens
<b>DOEs</b>	diffracting optical elements
<b>CGH</b>	computer-generated hologram
<b>BPP</b>	beam parameter product
<b>FCNN</b>	fully connected neural network
<b>FCNNs</b>	fully connected neural networks

# List of Figures

2.1. Schematic of the cross-section of a standard optical fiber. . . . .	9
2.2. Comparison of (1) single-mode fiber, (2) step-index multimode fiber, and (3) graded-index multimode fiber. . . . .	10
2.3. Numerical aperture of optical fiber. . . . .	11
2.4. Schematic of the basic SMS fiber structure. . . . .	13
2.5. Schematic of (a) basic SMS fiber structure and (b) basic SMS composed of NCF. . . . .	15
2.6. Schematic of the SMS fiber structure composed of (a) etched MMF and (b) polished MMF. . . . .	16
2.7. Schematic of SMS structure with tapered fiber: (a) tapered MMF; (b) tapered multi-mode microfiber (MMMMF) combining Fresnel reflection; (c) multi-tapered MMF; and (d) MMF sandwiched between two half-tapered SMFs. . . . .	18
2.8. Schematic of cascaded SMS fiber structure: (a) SMF-MMF-SMF-MMF-SMF; (b) SMF-MMF-TCF-MMF-SMF; (c) SMF-MMF-TCSMF-MMF-SMF; and (d) SMF-NCF-SMF-MMF-SMF. . . . .	19
2.9. Schematic of the basic SMS fiber structure. . . . .	24
2.10. Example of a commonly used MMF imaging system. P, polarizer; BS1, beam splitter; L1, lens; L2, lens; TL1, tube lens; OBJ1, objective lens; MMF, multimode fiber; OBJ2, objective lens; TL2, tube lens; BS2, beam splitter; L3, lens; L4, lens. . . . .	25
2.11. Concept of a reference-less MMF imaging system. P, polarizer; L1, lens; L2, lens; SLM, spatial light modulator; TL1, tube lens; OBJ1, objective lens; MMF, multimode fiber; OBJ2, objective lens; TL2, tube lens. . . . .	26
3.1. Schematic diagram of the experimental setup for temperature and strain measurement. BLS, broadband light source; SMF, single-mode fiber; MMF, multimode fiber; OSA, optical spectrum analyzer. . . . .	35

3.2. Temperature measurement results for the MMF with different core diameters. Measured spectral dependence on temperature: (a) 50- $\mu\text{m}$ core diameter, (b) 105- $\mu\text{m}$ core diameter, and (c) 200- $\mu\text{m}$ core diameter. Spectral dip shifts as a function of temperature: (d) 50- $\mu\text{m}$ core diameter, (e) 105- $\mu\text{m}$ core diameter, and (f) 200- $\mu\text{m}$ core diameter. . . . .	36
3.3. Strain measurement results for the MMF with different core diameters. Measured spectral dependence on strain: (a) 50- $\mu\text{m}$ core diameter, (c) 105- $\mu\text{m}$ core diameter, and (e) 200- $\mu\text{m}$ core diameter. Dip wavelength versus strain: (b) 50- $\mu\text{m}$ core diameter, (d) 105- $\mu\text{m}$ core diameter, and (f) 200- $\mu\text{m}$ core diameter. . . . .	37
3.4. Temperature measurement results for the MMF with different NAs. Measured spectral dependence on temperature: (a) 0.22 NA, (b) 0.39 NA, and (c) 0.5 NA. Spectral dip shifts as a function of temperature: (d) 0.22 NA, (e) 0.39 NA, and (f) 0.5 NA. . . . .	38
3.5. Strain measurement results for the MMF with different NAs. Measured spectral dependence on strain: (a) 0.22 NA, (b) 0.39 NA, and (c) 0.5 NA. Dip wavelength versus strain: (d) 0.22 NA, (e) 0.39 NA, and (f) 0.5 NA. . . . .	39
3.6. Temperature measurement results for the MMF with different lengths. Measured spectral dependence on temperature: (a) 2 cm, (b) 4 cm, (c) 8 cm, (d) 12 cm, and (e) 16 cm. . . . .	40
3.7. Temperature measurement results for the MMF with different lengths. Spectral dip shifts as a function of temperature: (a) 2 cm, (b) 4 cm, (c) 8 cm, (d) 12 cm, and (e) 16 cm. . . . .	41
3.8. Strain measurement results for the MMF with different lengths. Measured spectral dependence on strain: (a) 4 cm, (b) 8 cm, and (c) 12 cm. Dip wavelength versus strain: (d) 4 cm, (e) 8 cm, and (f) 12 cm. . . . .	42
3.9. Measured temperature sensitivity plotted as a function of strain. The gray area indicates the $\pm 10\%$ range of the mean temperature sensitivity. . . . .	43
3.10. Temperature measurement results with varied applied strains in the range of 0 to 1100 $\mu\epsilon$ with steps of 100 $\mu\epsilon$ . . . . .	44
3.11. Spectral dip shifts as a function of temperature with varied strains applied in the range of 0 to 1100 $\mu\epsilon$ with steps of 100 $\mu\epsilon$ . . . . .	45
4.1. (a) Photo of square-core fiber from the top view. (b) Schematic diagram of the square core shape. . . . .	48
4.2. Beam propagation in an SCF-based SMS structure with phase distributions at different lengths of the SCF. . . . .	49

4.3. Beam propagation in a circular MMF-based SMS structure with phase distributions at different lengths of the circular MMF. . . . .	50
4.4. Schematic diagram of the experimental setup and the sensor configuration. BLS, broadband light source; SMF, single-mode fiber; SCF, square-core fiber; OSA, optical spectrum analyzer. . . . .	51
4.5. (a) Measured dependence of spectral dip shifts on temperature in the range of 30 to 80°C in steps of 10°C. (b) Dip shift as a function of temperature. The blue solid line represents the dip wavelength shift against temperature, and the green dash-dotted line represents the dip power against temperature. . .	52
4.6. (a) Measured dependence of spectral dip shifts on strain in the range of 0 to 100 $\mu\epsilon$ in steps of 20 $\mu\epsilon$ . (b) Dip shift as a function of strain. The blue solid line represents the dip wavelength shift against strain, and the green dash-dotted line represents the dip power against strain. . . . .	53
4.7. Temperature measurement results with varied applied strains. Measured spectral dependences on temperature: (a) 0 $\mu\epsilon$ , (b) 100 $\mu\epsilon$ , (c) 200 $\mu\epsilon$ , (d) 300 $\mu\epsilon$ , (e) 400 $\mu\epsilon$ , and (f) 500 $\mu\epsilon$ strains applied. . . . .	54
4.8. Spectral dip shifts as a function of temperature with varied strains applied: (a) 0 $\mu\epsilon$ , (b) 100 $\mu\epsilon$ , (c) 200 $\mu\epsilon$ , (d) 300 $\mu\epsilon$ , (e) 400 $\mu\epsilon$ , and (f) 500 $\mu\epsilon$ strains applied. . . . .	55
4.9. Measured temperature sensitivity plotted as a function of strain. The gray area indicates the $\pm 3\%$ range of the mean temperature sensitivity. . . . .	56
5.1. (a) Schematic diagram of the core-offset SMS structure with an offset at the input SMF/MMF boundary. (b) Image of the core offset spliced (offset = 20 $\mu\text{m}$ ). 60	
5.2. Images of core-offset spliced parts with offset amplitudes of (a) 10 $\mu\text{m}$ , (b) 15 $\mu\text{m}$ , (c) 20 $\mu\text{m}$ , (d) 25 $\mu\text{m}$ , and (c) 30 $\mu\text{m}$ . . . . .	60
5.3. Temperature measurement results for the input core-offset SMS structure. Measured spectral dependences on temperature with core-offsets of (a) 10 $\mu\text{m}$ , (b) 15 $\mu\text{m}$ , (c) 20 $\mu\text{m}$ , (d) 25 $\mu\text{m}$ , and (c) 30 $\mu\text{m}$ . . . . .	61
5.4. Temperature measurement results for the input core-offset SMS structure. Spectral dip shifts plotted as a function of temperature with core-offsets of (a) 10 $\mu\text{m}$ , (b) 15 $\mu\text{m}$ , (c) 20 $\mu\text{m}$ , (d) 25 $\mu\text{m}$ , and (c) 30 $\mu\text{m}$ . . . . .	62
5.5. Temperature measurement results for the output core-offset SMS structure. Measured spectral dependences on temperature with core-offsets of (a) 10 $\mu\text{m}$ , (b) 15 $\mu\text{m}$ , (c) 20 $\mu\text{m}$ , (d) 25 $\mu\text{m}$ , and (e) 30 $\mu\text{m}$ . Spectral dip shifts plotted as a function of temperature with core-offsets of (f) 10 $\mu\text{m}$ , (g) 15 $\mu\text{m}$ , (h) 20 $\mu\text{m}$ , (i) 25 $\mu\text{m}$ , and (j) 30 $\mu\text{m}$ . . . . .	63

## List of Figures

---

5.6. Strain measurement results for the input core-offset SMS structure. Measured spectral dependences on strain with core-offsets of (a) 10 $\mu\text{m}$ , (b) 15 $\mu\text{m}$ , (c) 20 $\mu\text{m}$ , (d) 25 $\mu\text{m}$ , and (c) 30 $\mu\text{m}$ . . . . .	64
5.7. Strain measurement results for the input core-offset SMS structure. Spectral dip shifts plotted as a function of strain with core-offsets of (a) 10 $\mu\text{m}$ , (b) 15 $\mu\text{m}$ , (c) 20 $\mu\text{m}$ , (d) 25 $\mu\text{m}$ , and (c) 30 $\mu\text{m}$ . . . . .	65
5.8. Strain measurement results for the output core-offset SMS structure. Measured spectral dependences on strain with core-offsets of (a) 10 $\mu\text{m}$ , (b) 15 $\mu\text{m}$ , (c) 20 $\mu\text{m}$ , (d) 25 $\mu\text{m}$ , and (e) 30 $\mu\text{m}$ . Spectral dip shifts plotted as a function of strain with core-offsets of (f) 10 $\mu\text{m}$ , (g) 15 $\mu\text{m}$ , (h) 20 $\mu\text{m}$ , (i) 25 $\mu\text{m}$ , and (j) 30 $\mu\text{m}$ . . . . .	66
5.9. Measured results of the aligned SMS sensor in the same conditions as core-offset sensors: (a) measured spectral dependences on temperature, (b) spectral dip shifts plotted as a function of temperature, (c) measured spectral dependences on strain, and (d) spectral dip shifts plotted as a function of strain. 67	67
5.10. Summary of measurement with the input and output core-offset SMS structures: (a) temperature and (b) strain. . . . .	68
6.1. Flowchart of MMF imaging system with deep learning. . . . .	72
6.2. Schematic diagram of the experimental setup; BE, beam expander; HWP, half-wave plate; P, polarizer; I1, iris; BS, beam splitter; SLM, spatial light modulator; L1, lens; I2, iris; L2, lens; Obj1, objective lens; MMF, multimode fiber; Obj2, objective lens; L3, lens; CMOS, CMOS camera. . . . .	72
6.3. Simplified working principle of the SLM. CGH, computer-generated hologram; SLM, spatial light modulator; DOE, diffracting optical element. . . . .	74
6.4. Schematic diagram of beam quality measurement. . . . .	75
6.5. Flowchart of the multimode fiber imaging data acquisition via MATLAB. . . . .	76
6.6. Machine learning basics: (a) illustration of convolution operation (a $2 \times 2$ kernel applied to a $3 \times 3$ image, resulting in a $2 \times 2$ image), (b) max pooling operation, (c) a fully connected layer. . . . .	79
6.7. Original U-Net architecture. . . . .	80
6.8. The optimized U-Net architecture. . . . .	81
6.9. The architecture of the fully connected neural network (FCNN). . . . .	81

6.10. Demonstration of MMF imaging reconstruction on MNIST dataset with a 400- $\mu\text{m}$ core diameter MMF. (a) Representative samples of $28 \times 28$ ground truth images. (b) The corresponding output speckles ( $112 \times 112$ ) collected by the setup in Fig. 6.2. (c) Reconstructed $28 \times 28$ images (digits) produced by FCNN and the SSIM related to the ground truth are shown below each reconstructed image. (d) The same images reconstructed by U-Net and its SSIM. . . . .	84
6.11. Speckle acquisitions at different temperatures with time. . . . .	85
6.12. Speckle patterns of the ground truth digit 6 (acquired with a 200- $\mu\text{m}$ core diameter MMF) at different temperatures with corresponding MSE compared to that acquired at $25^\circ\text{C}$ . . . . .	86
6.13. MNIST digits reconstructed by a fully connected neural network (FCNN) with simulated noised datasets. The SSIM values indicate the similarities between reconstructed and ground truth images. . . . .	88
6.14. MNIST digits reconstructed by a fully connected neural network (FCNN) at different temperatures (speckles acquired with a 200- $\mu\text{m}$ core diameter MMF). (a) shows the ground truth images, (b)-(i) represent the reconstructed images at different temperatures with the corresponding SSIM. . . . .	89
6.15. MNIST digits reconstructed by U-Net with simulated noised datasets. The SSIM values indicate the similarities between reconstructed and ground truth images. . . . .	90
6.16. MNIST digits reconstructed by U-Net at different temperatures (speckles acquired with a 200- $\mu\text{m}$ core diameter MMF). (a) shows the ground truth images, (b)-(i) represent the reconstructed images at different temperatures with the corresponding SSIM. . . . .	91
6.17. Average SSIM versus (a) applied MSE values in simulation and (b) temperature changes in experiment. . . . .	92
6.18. Natural images reconstructed by multi-hidden-layer fully connected neural network (FCNN): (c) 1-hidden-layer FCNN, (d) 2-hidden-layer FCNN, and (e) 3-hidden-layer FCNN. The SSIM values indicate the similarities between reconstructed and ground truth images. . . . .	94
6.19. Training (dotted line) and validation (solid line) losses as a function of the number of epochs for multi-hidden-layer FCNN: 1-hidden-layer (blue), 2-hidden-layer (orange), and 3-hidden-layer (green). . . . .	94
6.20. Natural images reconstructed by U-Net. The SSIM values indicate the similarities between reconstructed and ground truth images. . . . .	95



# List of Tables

3.1. Temperature and strain sensitivities measured with different core diameters of the MMF. . . . .	36
3.2. Temperature and strain sensitivities measured with different NAs of the MMF.	38
3.3. Temperature and strain sensitivities measured with different lengths of the MMF. . . . .	42
4.1. Parameters of the fibers used in the beam propagation simulation. . . . .	48
4.2. Comparison of temperature sensitivities with other MMI-based optical fiber sensors using specialty fibers. . . . .	53
6.1. Components list of the MMF imaging system. . . . .	73
6.2. Comparison of MSE and SSIM of simulation and measurement results. . . .	87
6.3. Summary of average SSIM, training time, and the number of training parameters for different neural network architectures. . . . .	96



# Acknowledgments

I would like to express my deepest gratitude to my doctoral supervisor Prof. Dr.-Ing. habil. Dr. h.c. Alexander W. Koch, for this opportunity to do my Ph.D. at the Institute for Measurement Systems and Sensor Technology (MST) of the Technical University of Munich (TUM), where the research environment is vigorous and interdisciplinary. I appreciate that he gives me scientific freedom to pursue works that interest me. His knowledge, insight, and constructive suggestions also helped me with my publications.

I could not have undertaken this journey without the generosity of Prof. Dr. Yosuke Mizuno for his knowledge, expertise, and unconditional support. It was an unforgettable time at his lab, where I tried some new topics, experienced different cultures, and felt very welcome. I am always inspired by his passion for research when I talk with Mizuno-Sensei. I am also so appreciative of his thoughtfulness to me.

I am deeply indebted to Dr.-Ing. Martin Jakobi for his support in every aspect, from scientific work to spare time, at MST. I am thankful that he was always patient and considerate. Thanks should also go to Ms. Rita von Grafenstein for the most helpful and perfect organization of my work at MST. I would like to extend my thanks to all the members at MST for their support.

Many thanks go to my collaborator, Changyan Zhu, a Ph.D. student from Nanyang Technological University, for his contribution to the topic of multimode fiber imaging. Without him, this topic would not be possible. I am grateful for the chance to work with him. I would like to acknowledge Ennio Colicchia, who was supervised by me, for his excellent work on multimode fiber imaging. We started this topic almost from zero. Without his help, results would not be so promising in such a short time.

I could not enjoy the journey without my cool colleagues. Dr.-Ing. Patrick Kienle and Dr.-Ing. Michael Köhler are always there for discussions and are more than colleagues to me, as we had so much fun in our leisure time. I appreciate our time together. I also had the pleasure of working with Dr.-Ing. Shengjia Wang, Dr.-Ing. Moritz Graf, Dr.-Ing. Franziska Brändle, Maximilian Fink, and Qiang Bian.

Words cannot express my gratitude to my friends for their caring, encouragement, and love. It was always enjoyable to be with Dr.-Ing. Xingchen Dong and Dr.rer.nat. Xinxu Zhao to discuss our work and have fun. Without Michael Schild, Dr.-Ing. Philipp Heidingsfelder, and Sebastian Strobel, I would not start my Ph.D. in Germany. I am so grateful that they

## Acknowledgments

---

always took care of me and enriched my life here. I particularly thank Marcella Schild for the substantial amount of time and effort she dedicated to proofreading my dissertation.

Special thanks to my friend, colleague, and office buddy Wolfgang Kurz. I am so happy to know him and appreciative that he became such a good friend. We had many laughs, fun, and even arguments in our office. We also developed traditions for ourselves, e.g., live streaming and traveling in the world. These things made and will continue to make my life colorful.

Special appreciation belongs to my friend Di Liu. I am thankful she is always there for me, no matter which scenario. I cherish the help and joy she brought to my daily life, which would not be nice without her. They are always precious memories of our talking, trips, and activities.

Of course, many special thanks to all my close friends in China for always being supportive, caring, and funny. Without them, this journey would be harder for me, especially in the last few abnormal years.

I am extremely grateful to my mother, the most important person, for her unconditional understanding, support, and love. I would be remiss in not mentioning my family members. Their belief in me has kept my spirits and motivation high during this process.

My very personal gratitude belongs to Ayu, who means a lot to me.

Munich, January 2023  
Kun Wang

# Bibliography

- [1] Theodore H. Maiman. “Stimulated Optical Radiation in Ruby”. In: *Nature* 187.4736 (1960), pp. 493–494. DOI: 10.1038/187493a0.
- [2] Charles K. Kao and George A. Hockham. “Dielectric-fibre surface waveguides for optical frequencies”. In: *Proceedings of the Institution of Electrical Engineers* 113.7 (1966), pp. 1151–1158. DOI: 10.1049/piee.1966.0189.
- [3] Anne Schwarz-Pfeiffer, Viktorija Mecnika, Markus Beckers, Thomas Gries, and Stefan Jockenhoevel. “Optical Fibers”. In: *Handbook of Smart Textiles*. Ed. by Xi-aoming Tao. Singapore: Springer Singapore, 2015, pp. 79–108. DOI: 10.1007/978-981-4451-45-1\_4.
- [4] Felix P. Kapron, Donald B. Keck, and Robert D. Maurer. “Radiation losses in glass optical waveguides”. In: *Applied Physics Letters* 17.10 (1970), pp. 423–425. DOI: 10.1063/1.1653255. eprint: <https://doi.org/10.1063/1.1653255>.
- [5] Masaharu Horiguchi and Hiroshi Osanai. “Spectral losses of low-OH-content optical fibres”. In: *Electronics Letters* 12 (12 June 1976), 310–312(2).
- [6] Terenumi Miya, Y Terunuma, Tatsuya Hosaka, and Tadakazu Miyashita. “Ultimate low-loss single-mode fibre at 1.55  $\mu\text{m}$ ”. In: *Electronics Letters* 15 (4 Feb. 1979), 106–108(2).
- [7] Govind P Agrawal. *Fiber-optic communication systems, 5th Edition*. Wiley, 2021.
- [8] Alan Willner, ed. *Optical Fiber Telecommunications VII, 1st Edition*. Academic Press, 2019.
- [9] Ignacio R Matias, Satoshi Ikezawa, and Jesus Corres. *Fiber Optic Sensors: current status and future possibilities*. Vol. 21. Springer, 2016.
- [10] Shizhuo Yin, Paul B Ruffin, and TS Francis. *Fiber optic sensors*. CRC press, 2017.
- [11] Hiroshi Murata. *Handbook of optical fibers and cables*. Vol. 1. CRC Press, 2020.
- [12] Govind P Agrawal. “Nonlinear fiber optics”. In: *Nonlinear Science at the Dawn of the 21st Century*. Springer, 2000, pp. 195–211.
- [13] Andrew D Yablon. *Optics of fusion splicing*. Springer, 2005.

- [14] Xu-dong Wang and Otto S. Wolfbeis. "Fiber-Optic Chemical Sensors and Biosensors (2015–2019)". In: *Analytical Chemistry* 92.1 (2020). PMID: 31665884, pp. 397–430. DOI: 10.1021/acs.analchem.9b04708. eprint: <https://doi.org/10.1021/acs.analchem.9b04708>.
- [15] Angela Leung, P. Mohana Shankar, and Raj Mutharasan. "A review of fiber-optic biosensors". In: *Sensors and Actuators B: Chemical* 125.2 (2007), pp. 688–703. DOI: 10.1016/j.snb.2007.03.010.
- [16] Quan Chai, Yang Luo, Jing Ren, Jianzhong Zhang, Jun Yang, Libo Yuan, and Gang-Ding Peng. "Review on fiber-optic sensing in health monitoring of power grids". In: *Optical Engineering* 58.7 (2019), p. 072007. DOI: 10.1117/1.oe.58.7.072007.
- [17] Yi Bao, Ying Huang, Matthew S. Hoehler, and Genda Chen. "Review of Fiber Optic Sensors for Structural Fire Engineering". In: *Sensors* 19.4 (2019), p. 877. DOI: 10.3390/s19040877.
- [18] K.O. Hill and G. Meltz. "Fiber Bragg grating technology fundamentals and overview". In: *Journal of Lightwave Technology* 15.8 (1997), pp. 1263–1276. DOI: 10.1109/50.618320.
- [19] Bai-Ou Guan, Hwa-Yaw Tam, Xiao-Ming Tao, and Xiao-Yi Dong. "Simultaneous strain and temperature measurement using a superstructure fiber Bragg grating". In: *IEEE Photonics Technology Letters* 12.6 (2000), pp. 675–677. DOI: 10.1109/68.849081.
- [20] Vikram Bhatia and Ashish M Vengsarkar. "Optical fiber long-period grating sensors". In: *Optics Letters* 21.9 (1996), pp. 692–694. DOI: 10.1364/OL.21.000692.
- [21] Yiping Wang. "Review of long period fiber gratings written by CO<sub>2</sub> laser". In: *Journal of Applied Physics* 108.8 (2010), p. 081101. DOI: 10.1063/1.3493111.
- [22] Mohammed Nasser Alahbabi, YT Cho, and TP Newson. "Simultaneous temperature and strain measurement with combined spontaneous Raman and Brillouin scattering". In: *Optics letters* 30.11 (2005), pp. 1276–1278.
- [23] Hang-Eun Joe, Huitaek Yun, Seung-Hwan Jo, Martin B.G. Jun, and Byung-Kwon Min. "A review on optical fiber sensors for environmental monitoring". In: *International Journal of Precision Engineering and Manufacturing-Green Technology* 5.1 (2018), pp. 173–191. DOI: 10.1007/s40684-018-0017-6.

- [24] Yosuke Mizuno, Zuyuan He, and Kazuo Hotate. "Measurement range enlargement in Brillouin optical correlation-domain reflectometry based on temporal gating scheme". In: *Optics Express* 17.11 (May 2009), pp. 9040–9046. DOI: 10.1364/oe.17.009040.
- [25] Andrey Kobaykov, Michael Sauer, and Dipak Chowdhury. "Stimulated Brillouin scattering in optical fibers". In: *Advances in Optics and Photonics* 2.1 (Mar. 2010), pp. 1–59. DOI: 10.1364/AOP.2.000001.
- [26] Yong Wang, Qing Huang, Wenjie Zhu, Minghong Yang, and Elfed Lewis. "Novel optical fiber SPR temperature sensor based on MMF-PCF-MMF structure and gold-PDMS film". In: *Optics express* 26.2 (2018), pp. 1910–1917.
- [27] Qiaokang Liang, Kunlin Zou, Jianyong Long, Jing Jin, Dan Zhang, Gianmarc Copola, Wei Sun, Yaonan Wang, and Yunjian Ge. "Multi-Component FBG-Based Force Sensing Systems by Comparison With Other Sensing Technologies: A Review". In: *IEEE Sensors Journal* 18.18 (2018), pp. 7345–7357. DOI: 10.1109/JSEN.2018.2861014.
- [28] Muhammad Arif Riza, Yun li Go, Sulaiman Wadi Harun, and Robert R. J. Maier. "FBG Sensors for Environmental and Biochemical Applications—A Review". In: *IEEE Sensors Journal* 20.14 (2020), pp. 7614–7627. DOI: 10.1109/JSEN.2020.2982446.
- [29] Qiang Wu, Yuwei Qu, Juan Liu, Jinhui Yuan, Sheng-Peng Wan, Tao Wu, Xing-Dao He, Bin Liu, Dejun Liu, Youqiao Ma, Yuliya Semenova, Pengfei Wang, Xiangjun Xin, and Gerald Farrell. "Singlemode-Multimode-Singlemode Fiber Structures for Sensing Applications—A Review". In: *IEEE Sensors Journal* 21.11 (2021), pp. 12734–12751. DOI: 10.1109/JSEN.2020.3039912.
- [30] Kun Wang, Xingchen Dong, Michael H. Köhler, Patrick Kienle, Qiang Bian, Martin Jakobi, and Alexander W. Koch. "Advances in Optical Fiber Sensors Based on Multimode Interference (MMI): A Review". In: *IEEE Sensors Journal* 21.1 (2021), pp. 132–142. DOI: 10.1109/JSEN.2020.3015086.
- [31] Yujuan Zhang, Linlin Xue, Tongxin Wang, Li Yang, Bing Zhu, and Qijin Zhang. "High Performance Temperature Sensing of Single Mode-Multimode-Single Mode Fiber With Thermo-Optic Polymer as Cladding of Multimode Fiber Segment". In: *IEEE Sensors Journal* 14.4 (2014), pp. 1143–1147. DOI: 10.1109/JSEN.2013.2293536.
- [32] Ricardo Oliveira, Jonas H Osório, Stenio Aristilde, Lúcia Bilro, Rogerio N Nogueira, and Cristiano MB Cordeiro. "Simultaneous measurement of strain, temperature and refractive index based on multimode interference, fiber tapering and fiber Bragg gratings". In: *Measurement Science and Technology* 27.7 (2016), p. 075107.

- [33] Ke Tian, Gerald Farrell, Xianfan Wang, Wenlei Yang, Yifan Xin, Haidong Liang, Elfed Lewis, and Pengfei Wang. "Strain sensor based on gourd-shaped single-mode-multimode-single-mode hybrid optical fibre structure". In: *Optics Express* 25.16 (2017), pp. 18885–18896. DOI: 10.1364/oe.25.018885.
- [34] Zhi-bo Liu, Yang Li, Yan Liu, Zhong-Wei Tan, and Shuisheng Jian. "A Static Axial Strain Fiber Ring Cavity Laser Sensor Based on Multi-Modal Interference". In: *IEEE Photonics Technology Letters* 25.21 (2013), pp. 2050–2053. DOI: 10.1109/1pt.2013.2280755.
- [35] Joaquin Ascorbe, Jesus M. Corres, Francisco J. Arregui, and Ignacio R. Matias. "Recent Developments in Fiber Optics Humidity Sensors". In: *Sensors* 17.4 (2017), p. 893. DOI: 10.3390/s17040893.
- [36] Xianfan Wang, Gerald Farrell, Elfed Lewis, Ke Tian, Libo Yuan, and Pengfei Wang. "A Humidity Sensor Based on a Singlemode-Side Polished Multimode–Singlemode Optical Fibre Structure Coated with Gelatin". In: *Journal of Lightwave Technology* 35.18 (Sept. 2017), pp. 4087–4094. DOI: 10.1109/jlt.2017.2730484.
- [37] Susana Silva, O Frazão, J Viegas, LA Ferreira, FM Araújo, F Xavier Malcata, and JL Santos. "Temperature and strain-independent curvature sensor based on a singlemode/multimode fiber optic structure". In: *Measurement science and technology* 22.8 (2011), p. 085201.
- [38] Xudong Zhang, Chunyu Liu, Jiping Liu, and Jiuru Yang. "Single Modal Interference-Based Fiber-Optic Sensor for Simultaneous Measurement of Curvature and Strain With Dual-Differential Temperature Compensation". In: *IEEE Sensors Journal* 18.20 (2018), pp. 8375–8380. DOI: 10.1109/JSEN.2018.2868064.
- [39] Xixi Li, Dejun Liu, Rahul Kumar, Wai Pang Ng, Yong-qing Fu, Jinhui Yuan, Chongxiu Yu, Yufeng Wu, Guorui Zhou, Gerald Farrell, Yuliya Semenova, and Qiang Wu. "A simple optical fiber interferometer based breathing sensor". In: *Measurement Science and Technology* 28.3 (2017), p. 035105. DOI: 10.1088/1361-6501/aa577d.
- [40] Abian B. Socorro, Enrique Santamaria, Joaquin Fernandez-Irigoyen, Ignacio Del Villar, Jesus M. Corres, Francisco J. Arregui, and Ignacio R. Matias. "Fiber-Optic Immunosensor Based on an Etched SMS Structure". In: *IEEE Journal of Selected Topics in Quantum Electronics* 23.2 (Mar. 2017), pp. 314–321. DOI: 10.1109/jstqe.2016.2633819.

- [41] Qiang Wu, Minwei Yang, Jinhui Yuan, Hau Ping Chan, Youqiao Ma, Yuliya Semenova, Pengfei Wang, Chongxiu Yu, and Gerald Farrell. "The use of a bend singlemode–multimode–singlemode (SMS) fibre structure for vibration sensing". In: *Optics & Laser Technology* 63 (2014), pp. 29–33.
- [42] Yu Qian, Yong Zhao, Qi-lu Wu, and Yang Yang. "Review of salinity measurement technology based on optical fiber sensor". In: *Sensors and Actuators B: Chemical* 260 (2018), pp. 86–105. DOI: 10.1016/j.snb.2017.12.077.
- [43] Qingqiang Meng, Xinyong Dong, Kai Ni, Yi Li, Ben Xu, and Zhemin Chen. "Optical Fiber Laser Salinity Sensor Based on Multimode Interference Effect". In: *IEEE Sensors Journal* 14.6 (June 2014), pp. 1813–1816. DOI: 10.1109/jsen.2014.2298511.
- [44] Erich Spitz and Alain Werts. "Transmission des images à travers une fibre optique". In: *Comptes Rendus Hebdomadaires Des Seances De L Academie Des Sciences Serie B* 264.14 (1967), pp. 1015–+.
- [45] Amnon Yariv. "On transmission and recovery of three-dimensional image information in optical waveguides". In: *J. Opt. Soc. Am.* 66.4 (Apr. 1976), pp. 301–306. DOI: 10.1364/JOSA.66.000301.
- [46] A. Gover, C. P. Lee, and A. Yariv. "Direct transmission of pictorial information in multimode optical fibers\*". In: *J. Opt. Soc. Am.* 66.4 (Apr. 1976), pp. 306–311. DOI: 10.1364/JOSA.66.000306.
- [47] Gilmore J. Dunning and R. C. Lind. "Demonstration of image transmission through fibers by optical phase conjugation". In: *Opt. Lett.* 7.11 (Nov. 1982), pp. 558–560. DOI: 10.1364/OL.7.000558.
- [48] Ioannis N. Papadopoulos, Salma Farahi, Christophe Moser, and Demetri Psaltis. "Focusing and scanning light through a multimode optical fiber using digital phase conjugation". In: *Opt. Express* 20.10 (May 2012), pp. 10583–10590. DOI: 10.1364/OE.20.010583.
- [49] Ioannis N. Papadopoulos, Salma Farahi, Christophe Moser, and Demetri Psaltis. "High-resolution, lensless endoscope based on digital scanning through a multimode optical fiber". In: *Biomed. Opt. Express* 4.2 (Feb. 2013), pp. 260–270. DOI: 10.1364/BOE.4.000260.
- [50] Yuecheng Shen, Yan Liu, Cheng Ma, and Lihong V. Wang. "Sub-Nyquist sampling boosts targeted light transport through opaque scattering media". In: *Optica* 4.1 (Jan. 2017), pp. 97–102. DOI: 10.1364/OPTICA.4.000097.

- [51] Jiamiao Yang, Yuecheng Shen, Yan Liu, Ashton S. Hemphill, and Lihong V. Wang. "Focusing light through scattering media by polarization modulation based generalized digital optical phase conjugation". In: *Applied Physics Letters* 111.20 (2017), p. 201108. DOI: 10.1063/1.5005831. eprint: <https://doi.org/10.1063/1.5005831>.
- [52] Antonio M. Caravaca-Aguirre, Eyal Niv, Donald B. Conkey, and Rafael Piestun. "Real-time resilient focusing through a bending multimode fiber". In: *Opt. Express* 21.10 (May 2013), pp. 12881–12887. DOI: 10.1364/OE.21.012881.
- [53] Ruo Yu Gu, Reza Nasiri Mahalati, and Joseph M. Kahn. "Design of flexible multimode fiber endoscope". In: *Opt. Express* 23.21 (Oct. 2015), pp. 26905–26918. DOI: 10.1364/OE.23.026905.
- [54] Damien Loterie, Salma Farahi, Ioannis Papadopoulos, Alexandre Goy, Demetri Psaltis, and Christophe Moser. "Digital confocal microscopy through a multimode fiber". In: *Opt. Express* 23.18 (Sept. 2015), pp. 23845–23858. DOI: 10.1364/OE.23.023845.
- [55] Yu Liu and Li Wei. "Low-cost high-sensitivity strain and temperature sensing using graded-index multimode fibers". In: *Applied Optics* 46.13 (May 2007), pp. 2516–2519. DOI: 10.1364/ao.46.002516.
- [56] Yuan Gong, Tian Zhao, Yun-Jiang Rao, and Yu Wu. "All-Fiber Curvature Sensor Based on Multimode Interference". In: *IEEE Photonics Technology Letters* 23.11 (June 2011), pp. 679–681. DOI: 10.1109/lpt.2011.2123086.
- [57] Qiang Wu, Agus Muhamad Hatta, Pengfei Wang, Yuliya Semenova, and Gerald Farrell. "Use of a Bent Single SMS Fiber Structure for Simultaneous Measurement of Displacement and Temperature Sensing". In: *IEEE Photonics Technology Letters* 23.2 (Jan. 2011), pp. 130–132. DOI: 10.1109/lpt.2010.2093515.
- [58] Jie Huang, Xinwei Lan, Hanzheng Wang, Lei Yuan, Tao Wei, Zhan Gao, and Hai Xiao. "Polymer optical fiber for large strain measurement based on multimode interference". In: *Optics Letters* 37.20 (Oct. 2012), pp. 4308–4310. DOI: 10.1364/ol.37.004308.
- [59] Goki Numata, Neisei Hayashi, Marie Tabaru, Yosuke Mizuno, and Kentaro Nakamura. "Ultra-Sensitive Strain and Temperature Sensing Based on Modal Interference in Perfluorinated Polymer Optical Fibers". In: *IEEE Photonics Journal* 6.5 (Oct. 2014), pp. 1–7. DOI: 10.1109/jphot.2014.2352637.

- [60] Susana Silva, Edwin G. P. Pachon, Marcos A. R. Franco, Juliano G. Hayashi, F. Xavier Malcata, Orlando Frazão, Pedro Jorge, and Cristiano M. B. Cordeiro. "Ultrahigh-sensitivity temperature fiber sensor based on multimode interference." In: *Applied Optics* 51.16 (June 2012), pp. 3236–3242. DOI: 10.1364/ao.51.003236.
- [61] Yaofei Chen, Qun Han, Tiegeng Liu, and Hai Xiao. "Wavelength Dependence of the Sensitivity of All-Fiber Refractometers Based on the Singlemode–Multimode–Singlemode Structure". In: *IEEE Photonics Journal* 6.4 (Aug. 2014), pp. 1–7. DOI: 10.1109/jphot.2014.2344004.
- [62] Ren Xi Gao, Qiang Wang, Fang Zhao, Bo Meng, and Shi Liang Qu. "Optimal design and fabrication of SMS fiber temperature sensor for liquid". In: *Optics Communications* 283.16 (2010), pp. 3149–3152. DOI: 10.1016/j.optcom.2010.04.027.
- [63] R.X. Gao, W.J. Liu, Y.Y. Wang, Q. Wang, F. Zhao, and S.L. Qu. "Design and fabrication of SMS fiber refractometer for liquid". In: *Sensors and Actuators A: Physical* 179 (2012), pp. 5–9. DOI: 10.1016/j.sna.2012.02.020.
- [64] Yong Zhao, Lu Cai, Xue-Gang Li, Fan-chao Meng, and Zhao Zhao. "Investigation of the high sensitivity RI sensor based on SMS fiber structure". In: *Sensors and Actuators A: Physical* 205 (2014), pp. 186–190. DOI: 10.1016/j.sna.2013.10.023.
- [65] Yamile Cardona-Maya, Ignacio Del Villar, Abian B. Socorro, Jesus M. Corres, Ignacio R. Matias, and Juan F. Botero-Cadavid. "Wavelength and Phase Detection Based SMS Fiber Sensors Optimized With Etching and Nanodeposition". In: *Journal of Lightwave Technology* 35.17 (Sept. 2017), pp. 3743–3749. DOI: 10.1109/jlt.2017.2719923.
- [66] Omar Fuentes, Ignacio Del Villar, Jose R. Vento, Abian B. Socorro, Elieser E. Gallego, Jesus M. Corres, and Ignacio R. Matias. "Increasing the Sensitivity of an Optic Level Sensor With a Wavelength and Phase Sensitive Single-Mode Multimode Single-Mode Fiber Structure". In: *IEEE Sensors Journal* 17.17 (Sept. 2017), pp. 5515–5522. DOI: 10.1109/jsen.2017.2724849.
- [67] Jieyuan Tang, Junjie Zhou, Junwen Guan, Shun Long, Jianhui Yu, Heyuan Guan, Huihui Lu, Yunhan Luo, Jun Zhang, and Zhe Chen. "Fabrication of Side-Polished Single Mode-Multimode-Single Mode Fiber and Its Characteristics of Refractive Index Sensing". In: *IEEE Journal of Selected Topics in Quantum Electronics* 23.2 (Mar. 2017), pp. 238–245. DOI: 10.1109/jstqe.2016.2615941.

- [68] Xianfan Wang, Ke Tian, Libo Yuan, Elfed Lewis, Gerald Farrell, and Pengfei Wang. "A High-Temperature Humidity Sensor Based on a Singlemode-Side Polished Multimode-Singlemode Fiber Structure". In: *Journal of Lightwave Technology* 36.13 (July 2018), pp. 2730–2736. DOI: 10.1109/jlt.2018.2815955.
- [69] Xianfan Wang, Jiquan Zhang, Ke Tian, Shunbin Wang, Libo Yuan, Elfed Lewis, Gerald Farrell, and Pengfei Wang. "Investigation of a novel SMS fiber based planar multimode waveguide and its sensing performance". In: *Optics Express* 26.20 (Oct. 2018), pp. 26534–26543. DOI: 10.1364/oe.26.026534.
- [70] Pengfei Wang, Gilberto Brambilla, Ming Ding, Yuliya Semenova, Qiang Wu, and Gerald Farrell. "High-sensitivity, evanescent field refractometric sensor based on a tapered, multimode fiber interference." In: *Optics Letters* 36.12 (June 2011), pp. 2233–2235. DOI: 10.1364/ol.36.002233.
- [71] Biyao Yang, Yanxiong Niu, Bowen Yang, Yanhui Hu, Lingling Dai, Yiheng Yin, and Ming Ding. "High Sensitivity Curvature Sensor With Intensity Demodulation Based on Single-Mode-Tapered Multimode–Single-Mode Fiber". In: *IEEE Sensors Journal* 18.3 (Feb. 2018), pp. 1094–1099. DOI: 10.1109/jsen.2017.2782241.
- [72] Claudécir R. Biazoli, Susana Silva, Marcos A. R. Franco, Orlando Frazão, and Cristiano M. B. Cordeiro. "Multimode interference tapered fiber refractive index sensors". In: *Appl. Opt.* 51.24 (Aug. 2012), pp. 5941–5945. DOI: 10.1364/AO.51.005941.
- [73] Ricardo M. Andre, Claudécir R. Biazoli, Susana O. Silva, Manuel B. Marques, Cristiano M. B. Cordeiro, and Orlando Frazao. "Strain-Temperature Discrimination Using Multimode Interference in Tapered Fiber". In: *IEEE Photonics Technology Letters* 25.2 (Jan. 2013), pp. 155–158. DOI: 10.1109/lpt.2012.2230617.
- [74] Qizhen Sun, Haipeng Luo, Hongbo Luo, Macheng Lai, Deming Liu, and Lin Zhang. "Multimode microfiber interferometer for dual-parameters sensing assisted by Fresnel reflection". In: *Optics Express* 23.10 (May 2015), pp. 12777–12783. DOI: 10.1364/oe.23.012777.
- [75] Yong Zhao, Lu Cai, and Hai-Feng Hu. "Fiber-Optic Refractive Index Sensor Based on Multi-Tapered SMS Fiber Structure". In: *IEEE Sensors Journal* 15.11 (Nov. 2015), pp. 6348–6353. DOI: 10.1109/jsen.2015.2458893.
- [76] Guoyong Sun, Gang Wu, Fan Wang, Ruyou Tang, and Guiming Qiu. "High-Stress Resistance Fiber Refractometer Based on MMF Sandwiched Between Two SMF Half-Tapers". In: *IEEE Photonics Technology Letters* 28.12 (June 2016), pp. 1336–1339. DOI: 10.1109/lpt.2016.2543245.

- [77] Linh Viet Nguyen, Dusun Hwang, Sucbei Moon, Dae Seung Moon, and Youngjoo Chung. "High temperature fiber sensor with high sensitivity based on core diameter mismatch". In: *Optics Express* 16.15 (July 2008), pp. 11369–11375. DOI: 10.1364/oe.16.011369.
- [78] Yue Ma, Xueguang Qiao, Tuan Guo, Ruohui Wang, Jing Zhang, Yinyan Weng, Qiangzhou Rong, Manli Hu, and Zhongyao Feng. "Mach-Zehnder Interferometer Based on a Sandwich Fiber Structure for Refractive Index Measurement". In: *IEEE Sensors Journal* 12.6 (June 2012), pp. 2081–2085. DOI: 10.1109/jsen.2012.2184751.
- [79] Rui Xiong, Hongyun Meng, Qiqi Yao, Ben Huang, Yongmei Liu, Hongchao Xue, Chunhua Tan, and Xuguang Huang. "Simultaneous Measurement of Refractive Index and Temperature Based on Modal Interference". In: *IEEE Sensors Journal* 14.8 (Aug. 2014), pp. 2524–2528. DOI: 10.1109/jsen.2014.2310463.
- [80] Zhengrong Tong, Jun Su, Ye Cao, and Weihua Zhang. "Simultaneous Measurement Based on Composite Interference Structure". In: *IEEE Photonics Technology Letters* 26.13 (July 2014), pp. 1310–1313. DOI: 10.1109/lpt.2014.2320593.
- [81] Yue Wu, Li Pei, Wenxing Jin, Youchao Jiang, Yuguang Yang, Ya Shen, and Shuisheng Jian. "Highly sensitive curvature sensor based on asymmetrical twin core fiber and multimode fiber". In: *Optics & Laser Technology* 92 (2017), pp. 74–79. DOI: 10.1016/j.optlastec.2017.01.007.
- [82] Yong Zhao, Lu Cai, and Xue-Gang Li. "Temperature-Insensitive Optical Fiber Curvature Sensor Based on SMF-MMF-TCSMF-MMF-SMF Structure". In: *IEEE Transactions on Instrumentation and Measurement* 66.1 (Jan. 2017), pp. 141–147. DOI: 10.1109/tim.2016.2615479.
- [83] Yaofei Chen, Yan Wang, Ruoyu Chen, Wenkai Yang, Hao Liu, Tiegeng Liu, and Qun Han. "A Hybrid Multimode Interference Structure-Based Refractive Index and Temperature Fiber Sensor". In: *IEEE Sensors Journal* 16.2 (Jan. 2016), pp. 331–335. DOI: 10.1109/jsen.2015.2484346.
- [84] Zhaojun Li, Liangtao Hou, Lingling Ran, Jing Kang, and Jiuru Yang. "Ultra-Sensitive Fiber Refractive Index Sensor with Intensity Modulation and Self-Temperature Compensation". In: *Sensors* 19.18 (2019), p. 3820. DOI: 10.3390/s19183820.
- [85] Simon Pevec and Denis Donlagić. "Multiparameter fiber-optic sensors: a review". In: *Optical Engineering* 58.7 (2019), pp. 1–26. DOI: 10.1117/1.oe.58.7.072009.

- [86] Ke Tian, Meng Zhang, Gerald Farrell, Ruoning Wang, Elfed Lewis, and Pengfei Wang. "Highly sensitive strain sensor based on composite interference established within S-tapered multimode fiber structure". In: *Optics Express* 26.26 (Dec. 2018), pp. 33982–33992. DOI: 10.1364/oe.26.033982.
- [87] M. Y. Mohd Noor, A. I. Azmi, A. S. Abdullah, A. S. Mohd Supa'at, N. Mohd Kassim, M. H. Ibrahim, and N. H. Ngajikin. "High Sensitivity of Balloon-Like Bent MMI Fiber Low-Temperature Sensor". In: *IEEE Photonics Technology Letters* 27.18 (Sept. 2015), pp. 1989–1992. DOI: 10.1109/lpt.2015.2448944.
- [88] Ke Tian, Gerald Farrell, Elfed Lewis, Xianfan Wang, Haidong Liang, and Pengfei Wang. "A high sensitivity temperature sensor based on balloon-shaped bent SMF structure with its original polymer coating". In: *Measurement Science and Technology* 29.8 (2018), p. 085104. DOI: 10.1088/1361-6501/aac992.
- [89] Huihao Wang, Hongyun Meng, Rui Xiong, Qinghao Wang, Ben Huang, Xing Zhang, Wei Yu, Chunhua Tan, and Xuguang Huang. "Simultaneous measurement of refractive index and temperature based on asymmetric structures modal interference". In: *Optics Communications* 364 (2015), pp. 191–194. DOI: 10.1016/j.optcom.2015.11.015.
- [90] Yuan Sun, Deming Liu, Ping Lu, Qizhen Sun, Wei Yang, Shun Wang, Li Liu, and Jiangshan Zhang. "Dual-Parameters Optical Fiber Sensor With Enhanced Resolution Using Twisted MMF Based on SMS Structure". In: *IEEE Sensors Journal* 17.10 (May 2017), pp. 3045–3051. DOI: 10.1109/jsen.2017.2673959.
- [91] Ke Tian, Yifan Xin, Wenlei Yang, Tao Geng, Jing Ren, Ya-Xian Fan, Gerald Farrell, Elfed Lewis, and Pengfei Wang. "A Curvature Sensor Based on Twisted Single-Mode–Multimode–Single-Mode Hybrid Optical Fiber Structure". In: *Journal of Lightwave Technology* 35.9 (May 2017), pp. 1725–1731. DOI: 10.1109/JLT.2017.2650941.
- [92] Jiali An, Yongxing Jin, Mingming Sun, and Xinyong Dong. "Relative Humidity Sensor Based on SMS Fiber Structure With Two Waist-Enlarged Tapers". In: *IEEE Sensors Journal* 14.8 (Aug. 2014), pp. 2683–2686. DOI: 10.1109/JSEN.2014.2313878.
- [93] Pengfei Wang, Shuo Zhang, Ruoning Wang, Gerald Farrell, Meng Zhang, Tao Geng, Elfed Lewis, and Ke Tian. "Temperature-insensitive refractometer based on an RI-modulated singlemode-multimode-singlemode fibre structure". In: *Optics Express* 27.10 (May 2019), pp. 13754–13764. DOI: 10.1364/oe.27.013754.

- [94] Ignacio Del Villar, Abian B. Socorro, Jesus M. Corres, Francisco J. Arregui, and Ignacio R. Matias. "Refractometric sensors based on multimode interference in a thin-film coated single-mode–multimode–single-mode structure with reflection configuration". In: *Appl. Opt.* 53.18 (June 2014), pp. 3913–3919. DOI: 10.1364/AO.53.003913.
- [95] Susana Silva, O. Frazão, J.L. Santos, and F.X. Malcata. "A reflective optical fiber refractometer based on multimode interference". In: *Sensors and Actuators B: Chemical* 161.1 (2012), pp. 88–92. DOI: <https://doi.org/10.1016/j.snb.2011.09.045>.
- [96] Jiangtao Zhou, Yiping Wang, Changrui Liao, Bing Sun, Jun He, Guolu Yin, Shen Liu, Zhengyong Li, Guanjun Wang, Xiaoyong Zhong, and Jing Zhao. "Intensity modulated refractive index sensor based on optical fiber Michelson interferometer". In: *Sensors and Actuators B: Chemical* 208 (2015), pp. 315–319. DOI: <https://doi.org/10.1016/j.snb.2014.11.014>.
- [97] Da-Peng Zhou, Li Wei, Wing-Ki Liu, Yu Liu, and John W Y Lit. "Simultaneous measurement for strain and temperature using fiber Bragg gratings and multimode fibers". In: *Applied Optics* 47.10 (Apr. 2008), pp. 1668–1672. DOI: 10.1364/ao.47.001668.
- [98] Wenjun Zhou, Yan Zhou, Xinyong Dong, Li-Yang Shao, Jia Cheng, and J. Albert. "Fiber-Optic Curvature Sensor Based on Cladding-Mode Bragg Grating Excited by Fiber Multimode Interferometer". In: *IEEE Photonics Journal* 4.3 (June 2012), pp. 1051–1057. DOI: 10.1109/jphot.2012.2202895.
- [99] Yong Zhao, Lu Cai, Xue-Gang Li, and Fan-Chao Meng. "Liquid concentration measurement based on SMS fiber sensor with temperature compensation using an FBG". In: *Sensors and Actuators B: Chemical* 196 (2014), pp. 518–524. DOI: 10.1016/j.snb.2014.01.075.
- [100] Chao Li, Tigang Ning, Xiaodong Wen, Jing Li, Jingjing Zheng, Haidong You, Hongyao Chen, Chan Zhang, and Wei Jian. "Strain and temperature discrimination using a fiber Bragg grating and multimode interference effects". In: *Optics Communications* 343 (2015), pp. 6–9. DOI: 10.1016/j.optcom.2014.12.066.
- [101] Markus J. Schmid and Mathias S. Müller. "Measuring Bragg gratings in multimode optical fibers". In: *Opt. Express* 23.6 (Mar. 2015), pp. 8087–8094. DOI: 10.1364/OE.23.008087.
- [102] Ke Wang, Denis V. Klimov, and Zbigniew Kolber. "Seawater pH sensor based on the long period grating in a single-mode–multimode–single-mode structure". In: *Optical Engineering* 48.3 (2009), pp. 1–4. DOI: 10.1117/1.3093625.

- [103] Jie Huang, Xinwei Lan, Amardeep Kaur, Hanzheng Wang, Lei Yuan, and Hai Xiao. "Temperature compensated refractometer based on a cascaded SMS/LPFG fiber structure". In: *Sensors and Actuators B: Chemical* 198 (2014), pp. 384–387. DOI: 10.1016/j.snb.2014.03.062.
- [104] Agus Muhamad Hatta, Yuliya Semenova, Qiang Wu, and Gerald Farrell. "Strain sensor based on a pair of single-mode-multimode-single-mode fiber structures in a ratiometric power measurement scheme". In: *Applied Optics* 49.3 (Jan. 2010), pp. 536–541. DOI: 10.1364/ao.49.000536.
- [105] Minghong Yang, Hongliang Liu, Dongsheng Zhang, and Xinling Tong. "Hydrogen sensing performance comparison of Pd layer and Pd/WO<sub>3</sub> composite thin film coated on side-polished single- and multimode fibers". In: *Sensors and Actuators B: Chemical* 149.1 (2010), pp. 161–164. DOI: 10.1016/j.snb.2010.06.006.
- [106] Xinwei Lan, Jie Huang, Qun Han, Tao Wei, Zhan Gao, Hongmin Jiang, Junhang Dong, and Hai Xiao. "Fiber ring laser interrogated zeolite-coated singlemode-multimode-singlemode structure for trace chemical detection". In: *Optics Letters* 37.11 (June 2012), pp. 1998–2000. DOI: 10.1364/ol.37.001998.
- [107] Haipeng Luo, Qizhen Sun, Zhilin Xu, Deming Liu, and Lin Zhang. "Simultaneous measurement of refractive index and temperature using multimode microfiber-based dual Mach–Zehnder interferometer". In: *Optics Letters* 39.13 (July 2014), pp. 4049–4052. DOI: 10.1364/ol.39.004049.
- [108] Haipeng Luo, Qizhen Sun, Xiaolei Li, Zhijun Yan, Yanpeng Li, Deming Liu, and Lin Zhang. "Refractive index sensitivity characteristics near the dispersion turning point of the multimode microfiber-based Mach–Zehnder interferometer". In: *Optics Letters* 40.21 (Nov. 2015), pp. 5042–5045. DOI: 10.1364/ol.40.005042.
- [109] Hae Young Choi, Gopinath Mudhana, Kwan Seob Park, Un-Chul Paek, and Byeong Ha Lee. "Cross-talk free and ultra-compact fiber optic sensor for simultaneous measurement of temperature and refractive index". In: *Optics Express* 18.1 (Jan. 2010), pp. 141–149. DOI: 10.1364/oe.18.000141.
- [110] Yong Zhao, Lu Cai, and Xue-gang Li. "In-fiber modal interferometer for simultaneous measurement of curvature and temperature based on hollow core fiber". In: *Optics & Laser Technology* 92 (2017), pp. 138–141. DOI: 10.1016/j.optlastec.2017.01.024.
- [111] Yaxun Zhang, Ai Zhou, Boyang Qin, Quan Xu, Zhihai Liu, Jun Yang, and Libo Yuan. "Simultaneous Measurement of Temperature and Curvature Based on Hollow Annular Core Fiber". In: *IEEE Photonics Technology Letters* 26.11 (June 2014), pp. 1128–1131. DOI: 10.1109/lpt.2014.2316532.

- [112] Binbin Song, Yinping Miao, Wei Lin, Hao Zhang, Jixuan Wu, and Bo Liu. “Multi-mode interferometer-based twist sensor with low temperature sensitivity employing square coreless fibers”. In: *Opt. Express* 21.22 (Nov. 2013), pp. 26806–26811. DOI: 10.1364/OE.21.026806.
- [113] Xudong Zhang, Chunyu Liu, Jiping Liu, and Jiuru Yang. “Single Modal Interference-Based Fiber-Optic Sensor for Simultaneous Measurement of Curvature and Strain With Dual-Differential Temperature Compensation”. In: *IEEE Sensors Journal* 18.20 (Oct. 2018), pp. 8375–8380. DOI: 10.1109/jsen.2018.2868064.
- [114] Fan Yang, Z.K. Wang, and D.N. Wang. “A highly sensitive optical fiber strain sensor based on cascaded multimode fiber and photonic crystal fiber”. In: *Optical Fiber Technology* 47 (2019), pp. 102–106. DOI: 10.1016/j.yofte.2018.11.029.
- [115] Xue-Gang Li, Yong Zhao, Lu Cai, and Qi Wang. “Simultaneous Measurement of RI and Temperature Based on a Composite Interferometer”. In: *IEEE Photonics Technology Letters* 28.17 (Sept. 2016), pp. 1839–1842. DOI: 10.1109/lpt.2016.2573828.
- [116] David J Richardson, John M Fini, and Lynn E Nelson. “Space-division multiplexing in optical fibres”. In: *Nature Photonics* 7.5 (2013), pp. 354–362.
- [117] Sergey Turtaev, Ivo T. Leite, Tristan Altwegg-Boussac, Janelle M. P. Pakan, Nathalie L. Rochefort, and Tomáš Čižmár. “High-fidelity multimode fibre-based endoscopy for deep brain in vivo imaging”. In: *Light: Science & Applications* 7.1 (2018), p. 92. DOI: 10.1038/s41377-018-0094-x. eprint: 1806.01654.
- [118] Werner Göbel, Jason N. D. Kerr, Axel Nimmerjahn, and Fritjof Helmchen. “Miniaturized two-photon microscope based on a flexible coherent fiber bundle and a gradient-index lens objective”. In: *Opt. Lett.* 29.21 (Nov. 2004), pp. 2521–2523. DOI: 10.1364/OL.29.002521.
- [119] Sebastian A. Vasquez-Lopez, Raphaël Turcotte, Vadim Koren, Martin Plöschner, Zahid Padamsey, Martin J. Booth, Tomáš Čižmár, and Nigel J. Emptage. “Subcellular spatial resolution achieved for deep-brain imaging in vivo using a minimally invasive multimode fiber”. In: *Light: Science & Applications* 7.1 (2018), p. 110. DOI: 10.1038/s41377-018-0111-0.
- [120] Vivien Szabo, Cathie Ventalon, Vincent De Sars, Jonathan Bradley, and Valentina Emiliani. “Spatially Selective Holographic Photoactivation and Functional Fluorescence Imaging in Freely Behaving Mice with a Fiberscope”. In: *Neuron* 84.6 (2014), pp. 1157–1169. DOI: <https://doi.org/10.1016/j.neuron.2014.11.005>.

- [121] Michael Hughes, Tou Pin Chang, and Guang-Zhong Yang. “Fiber bundle endocytoscopy”. In: *Biomed. Opt. Express* 4.12 (Dec. 2013), pp. 2781–2794. DOI: 10.1364/B0E.4.002781.
- [122] Tomáš Čižmár and Kishan Dholakia. “Exploiting multimode waveguides for pure fibre-based imaging”. In: *Nature Communications* 3.1 (2012), p. 1027. DOI: 10.1038/ncomms2024.
- [123] Piergiorgio Caramazza, Oisín Moran, Roderick Murray-Smith, and Daniele Faccio. “Transmission of natural scene images through a multimode fibre”. In: *Nature Communications* 10.1 (2019), p. 2029. DOI: 10.1038/s41467-019-10057-8.
- [124] Martin Plöschner, Tomáš Tyc, and Tomáš Čižmár. “Seeing through chaos in multimode fibres”. In: *Nature Photonics* 9.8 (2015), pp. 529–535. DOI: 10.1038/nphoton.2015.112.
- [125] Joseph W Goodman. *Speckle phenomena in optics: theory and applications*. Roberts and Company Publishers, 2007.
- [126] I. M. Vellekoop and A. P. Mosk. “Focusing coherent light through opaque strongly scattering media”. In: *Opt. Lett.* 32.16 (Aug. 2007), pp. 2309–2311. DOI: 10.1364/OL.32.002309.
- [127] I. M. Vellekoop, E. G. van Putten, A. Lagendijk, and A. P. Mosk. “Demixing light paths inside disordered metamaterials”. In: *Opt. Express* 16.1 (Jan. 2008), pp. 67–80. DOI: 10.1364/OE.16.000067.
- [128] Jonghee Yoon, KyeoReh Lee, Jongchan Park, and YongKeun Park. “Measuring optical transmission matrices by wavefront shaping”. In: *Opt. Express* 23.8 (Apr. 2015), pp. 10158–10167. DOI: 10.1364/OE.23.010158.
- [129] Youngwoon Choi, Taeseok Daniel Yang, Christopher Fang-Yen, Pilsung Kang, Kyoung Jin Lee, Ramachandra R. Dasari, Michael S. Feld, and Wonshik Choi. “Overcoming the Diffraction Limit Using Multiple Light Scattering in a Highly Disordered Medium”. In: *Phys. Rev. Lett.* 107 (2 July 2011), p. 023902. DOI: 10.1103/PhysRevLett.107.023902.
- [130] C. W. J. Beenakker. “Random-matrix theory of quantum transport”. In: *Rev. Mod. Phys.* 69 (3 July 1997), pp. 731–808. DOI: 10.1103/RevModPhys.69.731.
- [131] Youngwoon Choi, Changhyeong Yoon, Moonseok Kim, Taeseok Daniel Yang, Christopher Fang-Yen, Ramachandra R. Dasari, Kyoung Jin Lee, and Wonshik Choi. “Scanner-Free and Wide-Field Endoscopic Imaging by Using a Single Multimode Optical Fiber”. In: *Phys. Rev. Lett.* 109 (20 Nov. 2012), p. 203901. DOI: 10.1103/PhysRevLett.109.203901.

- [132] Moussa N’Gom, Theodore B. Norris, Eric Michielssen, and Raj Rao Nadakuditi. “Mode control in a multimode fiber through acquiring its transmission matrix from a reference-less optical system”. In: *Opt. Lett.* 43.3 (Feb. 2018), pp. 419–422. DOI: 10.1364/OL.43.000419.
- [133] Liang Deng, Joseph D. Yan, Daniel S. Elson, and Lei Su. “Characterization of an imaging multimode optical fiber using a digital micro-mirror device based single-beam system”. In: *Opt. Express* 26.14 (July 2018), pp. 18436–18447. DOI: 10.1364/OE.26.018436.
- [134] Tianrui Zhao, Sebastien Ourselin, Tom Vercauteren, and Wenfeng Xia. “Seeing through multimode fibers with real-valued intensity transmission matrices”. In: *Opt. Express* 28.14 (July 2020), pp. 20978–20991. DOI: 10.1364/OE.396734.
- [135] Navid Borhani, Eirini Kakkava, Christophe Moser, and Demetri Psaltis. “Learning to see through multimode fibers”. In: *Optica* 5.8 (Aug. 2018), pp. 960–966. DOI: 10.1364/OPTICA.5.000960.
- [136] Li Deng. “The mnist database of handwritten digit images for machine learning research”. In: *IEEE Signal Processing Magazine* 29.6 (2012), pp. 141–142.
- [137] Olaf Ronneberger, Philipp Fischer, and Thomas Brox. “U-Net: Convolutional Networks for Biomedical Image Segmentation”. In: *Medical Image Computing and Computer-Assisted Intervention – MICCAI 2015*. Ed. by Nassir Navab, Joachim Hornegger, William M. Wells, and Alejandro F. Frangi. Cham: Springer International Publishing, 2015, pp. 234–241.
- [138] Karen Simonyan and Andrew Zisserman. *Very Deep Convolutional Networks for Large-Scale Image Recognition*. 2014. DOI: 10.48550/ARXIV.1409.1556.
- [139] Ping Wang and Jianglei Di. “Deep learning-based object classification through multimode fiber via a CNN-architecture SpeckleNet”. In: *Appl. Opt.* 57.28 (Oct. 2018), pp. 8258–8263. DOI: 10.1364/AO.57.008258.
- [140] Gary B. Huang, Marwan Mattar, Tamara Berg, and Eric Learned-Miller. “Labeled Faces in the Wild: A Database for Studying Face Recognition in Unconstrained Environments”. In: *Workshop on Faces in ‘Real-Life’ Images: Detection, Alignment, and Recognition*. Erik Learned-Miller and Andras Ferencz and Frédéric Jurie. Marseille, France, Oct. 2008.
- [141] Pengfei Fan, Tianrui Zhao, and Lei Su. “Deep learning the high variability and randomness inside multimode fibers”. In: *Opt. Express* 27.15 (July 2019), pp. 20241–20258. DOI: 10.1364/OE.27.020241.

- [142] Han Xiao, Kashif Rasul, and Roland Vollgraf. *Fashion-MNIST: a Novel Image Dataset for Benchmarking Machine Learning Algorithms*. 2017. DOI: 10.48550/ARXIV.1708.07747.
- [143] Ian T. Jolliffe and Jorge Cadima. “Principal component analysis: a review and recent developments”. In: *Philosophical Transactions of the Royal Society A: Mathematical, Physical and Engineering Sciences* 374 (2016).
- [144] Changyan Zhu, Eng Aik Chan, You Wang, Weina Peng, Ruixiang Guo, Baile Zhang, Cesare Soci, and Yidong Chong. “Image reconstruction through a multimode fiber with a simple neural network architecture”. In: *Scientific reports* 11.1 (2021), pp. 1–10.
- [145] Zhenyu Ju, Zhenming Yu, Ziyi Meng, Ning Zhan, Lili Gui, and Kun Xu. “Simultaneous illumination and imaging based on a single multimode fiber”. In: *Opt. Express* 30.9 (Apr. 2022), pp. 15596–15606. DOI: 10.1364/OE.454850.
- [146] Jonas Jongejan, Henry Rowley, Takashi Kawashima, Jongmin Kim, and Nick Fox-Gieg. “The quick, draw!-ai experiment (2016)”. In: URL <http://quickdraw.withgoogle.com> 4 (2016).
- [147] Marina E. Plissiti, P. Dimitrakopoulos, G. Sfikas, Christophoros Nikou, O. Krikoni, and A. Charchanti. “Sipakmed: A New Dataset for Feature and Image Based Classification of Normal and Pathological Cervical Cells in Pap Smear Images”. In: *2018 25th IEEE International Conference on Image Processing (ICIP)*. 2018, pp. 3144–3148. DOI: 10.1109/ICIP.2018.8451588.
- [148] Fu Feng, Jia-An Gan, Jingpeng Nong, Peng-Fei Chen, Guangyong Chen, Changjun Min, Xiacong Yuan, and Michael Somekh. “Data transmission with up to 100 orbital angular momentum modes via commercial multi-mode fiber and parallel neural networks”. In: *Opt. Express* 30.13 (June 2022), pp. 23149–23162. DOI: 10.1364/OE.459810.
- [149] Binbin Song, Chang Jin, Jixuan Wu, Wei Lin, Bo Liu, Wei Huang, and Shengyong Chen. “Deep learning image transmission through a multimode fiber based on a small training dataset”. In: *Opt. Express* 30.4 (Feb. 2022), pp. 5657–5672. DOI: 10.1364/OE.450999.
- [150] Zhoutian Liu, Lele Wang, Yuan Meng, Tiantian He, Sifeng He, Yousi Yang, Liuyue Wang, Jiading Tian, Dan Li, Ping Yan, et al. “All-fiber high-speed image detection enabled by deep learning”. In: *Nature communications* 13.1 (2022), pp. 1–8.
- [151] Arun Kumar, Ravi K. Varshney, Siny Antony C., and Pratha Sharma. “Transmission characteristics of SMS fiber optic sensor structures”. In: *Optics Communications* 219.1 (2003), pp. 215–219. DOI: 10.1016/s0030-4018(03)01289-6.

- [152] Tomohito Kawa, Goki Numata, Heeyoung Lee, Neisei Hayashi, Yosuke Mizuno, and Kentaro Nakamura. "Single-end-access strain and temperature sensing based on multimodal interference in polymer optical fibers". In: *IEICE Electronics Express* 14.3 (2017), pp. 20161239–20161239. DOI: 10.1587/elex.14.20161239.
- [153] Zhigang Cao, Zhao Zhang, Xiaochun Ji, Tao Shui, Rui Wang, Chenchen Yin, Shenglai Zhen, Liang Lu, and Benli Yu. "Strain-insensitive and high temperature fiber sensor based on a Mach–Zehnder modal interferometer". In: *Optical Fiber Technology* 20.1 (2014), pp. 24–27. DOI: <https://doi.org/10.1016/j.yofte.2013.11.003>.
- [154] Chi Liu, Yajun Jiang, Bobo Du, Tao Wang, Dingyi Feng, Biqiang Jiang, and Dexing Yang. "Strain-insensitive twist and temperature sensor based on seven-core fiber". In: *Sensors and Actuators A: Physical* 290 (2019), pp. 172–176. DOI: <https://doi.org/10.1016/j.sna.2019.03.026>.
- [155] Enbang Li, Xiaolin Wang, and Chao Zhang. "Fiber-optic temperature sensor based on interference of selective higher-order modes". In: *Applied Physics Letters* 89.9 (2006), p. 091119. DOI: 10.1063/1.2344835. eprint: <https://doi.org/10.1063/1.2344835>.
- [156] Raymond M Measures and S Abrate. "Structural monitoring with fiber optic technology". In: *Appl. Mech. Rev.* 55.1 (2002), B10–B11.
- [157] Enbang Li. "Temperature compensation of multimode-interference-based fiber devices". In: *Opt. Lett.* 32.14 (July 2007), pp. 2064–2066. DOI: 10.1364/OL.32.002064.
- [158] Lucas B. Soldano and Erik C.M. Pennings. "Optical multi-mode interference devices based on self-imaging: principles and applications". In: *Journal of Lightwave Technology* 13.4 (1995), pp. 615–627. DOI: 10.1109/50.372474.
- [159] Yosuke Mizuno and Kentaro Nakamura. "Experimental study of Brillouin scattering in perfluorinated polymer optical fiber at telecommunication wavelength". In: *Applied Physics Letters* 97.2 (2010), p. 021103.
- [160] Yosuke Mizuno, Goki Numata, Tomohito Kawa, Heeyoung Lee, Neisei Hayashi, and Kentaro Nakamura. "Multimodal Interference in Perfluorinated Polymer Optical Fibers: Application to Ultrasensitive Strain and Temperature Sensing". In: *IEICE Transactions on Electronics* E101.C.7 (2018), pp. 602–610. DOI: 10.1587/transle.E101.C.602.
- [161] Matthias C. Velsink, Zhouping Lyu, Pepijn W. H. Pinkse, and Lyubov V. Amitonova. "Comparison of round- and square-core fibers for sensing, imaging, and spectroscopy". In: *Opt. Express* 29.5 (Mar. 2021), pp. 6523–6531. DOI: 10.1364/OE.417021.

- [162] Madhu Veetikazhy, Anders Kragh Hansen, Dominik Marti, Stefan Mark Jensen, Anja Lykke Borre, Esben Ravn Andresen, Kishan Dholakia, and Peter Eskil Andersen. "BPM-Matlab: an open-source optical propagation simulation tool in MATLAB". In: *Opt. Express* 29.8 (Apr. 2021), pp. 11819–11832. DOI: 10.1364/OE.420493.
- [163] Huiwen Niu, Shuo Zhang, Wenhuan Chen, Yue Liu, Xiang Li, Yunxiang Yan, Shengjia Wang, Tao Geng, Weimin Sun, and Libo Yuan. "Optical Fiber Sensors Based on Core-Offset Structure: A Review". In: *IEEE Sensors Journal* 21.20 (2021), pp. 22388–22401. DOI: 10.1109/JSEN.2021.3110852.
- [164] Biao Wang, Weigang Zhang, Zhiyong Bai, Liyu Zhang, Tieyi Yan, Lei Chen, and Quan Zhou. "Mach-Zehnder Interferometer Based on Interference of Selective High-Order Core Modes". In: *IEEE Photonics Technology Letters* 28.1 (2016), pp. 71–74. DOI: 10.1109/LPT.2015.2483518.
- [165] Xinghu Fu, Fan Liu, Yu Zhang, Jing Wen, Dong Wang, Haiyang Xie, Guangwei Fu, and Weihong Bi. "A refractive-index sensitivity-enhanced sensor by core-offset splicing the triple cladding quartz specialty fiber". In: *Optical Fiber Technology* 46 (2018), pp. 63–67. DOI: <https://doi.org/10.1016/j.yofte.2018.09.005>.
- [166] Francisco F. Medina, Jorge Garcia-Sucerquia, Román Castañeda, and Giorgio Matteucci. "Angular criterion to distinguish between Fraunhofer and Fresnel diffraction". In: *Optik* 115.11 (2004), pp. 547–552. DOI: <https://doi.org/10.1078/0030-4026-00547>.
- [167] Babak Rahmani, Damien Loterie, Georgia Konstantinou, Demetri Psaltis, and Christophe Moser. "Multimode optical fiber transmission with a deep learning network". In: *Light: science & applications* 7.1 (2018), pp. 1–11.
- [168] Shigeki Aisawa, Kazuhiro Noguchi, and Takao Matsumoto. "Remote image classification through multimode optical fiber using a neural network". In: *Opt. Lett.* 16.9 (May 1991), pp. 645–647. DOI: 10.1364/OL.16.000645.
- [169] Takao Matsumoto, Masafumi Koga, Kazuhiro Noguchi, and Shigeki Aizawa. "Proposal for neural-network applications to fiber-optic transmission". In: *1990 IJCNN International Joint Conference on Neural Networks*. 1990, 75–80 vol.1. DOI: 10.1109/IJCNN.1990.137549.
- [170] Ronald K. Marusarz and Mohammad R. Sayeh. "Neural network-based multimode fiber-optic information transmission". In: *Appl. Opt.* 40.2 (Jan. 2001), pp. 219–227. DOI: 10.1364/AO.40.000219.
- [171] Zhou Wang, A.C. Bovik, H.R. Sheikh, and E.P. Simoncelli. "Image quality assessment: from error visibility to structural similarity". In: *IEEE Transactions on Image Processing* 13.4 (2004), pp. 600–612. DOI: 10.1109/TIP.2003.819861.

# Publications

## Journal Publications

- [J-1] **Kun Wang**, Yosuke Mizuno, Xingyu Su, Xingchen Dong, Wolfgang Kurz, Maximilian Fink, Heeyoung Lee, Martin Jakobi, and Alexander W. Koch. “Core diameter and numerical aperture dependences on the performance of fiber-optic multimode interference sensing”. In: *Applied Physics Express* 16.1 (Dec. 2022), p. 012003. DOI: 10.35848/1882-0786/aca9bc.
- [J-2] **Kun Wang**, Yosuke Mizuno, Kazuya Kishizawa, Yuma Toyoda, Heeyoung Lee, Koichi Ichige, Wolfgang Kurz, Xingchen Dong, Martin Jakobi, and Alexander W. Koch. “Temperature sensing based on multimode interference in polymer optical fibers: sensitivity enhancement by PC-APC connections”. In: *Japanese Journal of Applied Physics* 61.11 (Oct. 2022), p. 118001. DOI: 10.35848/1347-4065/ac9810.
- [J-3] **Kun Wang**, Yosuke Mizuno, Xingchen Dong, Wolfgang Kurz, Maximilian Fink, Martin Jakobi, and Alexander W. Koch. “Strain-insensitive high-sensitivity temperature sensing based on multimode interference in a square-core fiber”. In: *Japanese Journal of Applied Physics* 61.7 (June 2022), p. 078002. DOI: 10.35848/1347-4065/ac74fe.
- [J-4] **Kun Wang**, Xingchen Dong, Patrick Kienle, Maximilian Fink, Wolfgang Kurz, Michael H. Köhler, Martin Jakobi, and Alexander W. Koch. “Optical Fiber Sensor for Temperature and Strain Measurement Based on Multimode Interference and Square-Core Fiber”. In: *Micromachines* 12.10 (2021). DOI: 10.3390/mi12101239.
- [J-5] **Kun Wang**, Xingchen Dong, Michael H. Köhler, Patrick Kienle, Qiang Bian, Martin Jakobi, and Alexander W. Koch. “Advances in Optical Fiber Sensors Based on Multimode Interference (MMI): A Review”. In: *IEEE Sensors Journal* 21.1 (2021), pp. 132–142. DOI: 10.1109/JSEN.2020.3015086.
- [J-6] Maximilian Fink, Michael Schardt, Valentin Baier, **Kun Wang**, Martin Jakobi, and Alexander W. Koch. “Low-cost scanning LIDAR architecture with a scalable frame rate for autonomous vehicles”. In: *Appl. Opt.* 62.3 (Jan. 2023), pp. 675–682. DOI: 10.1364/AO.479765.

- [J-7] Patrick Kienle, Nicholas E. Fest, Agnia D. Larasati, **Kun Wang**, Michael H. Köhler, Martin Jakobi, and Alexander W. Koch. “Analyse eines fehlerkompensierten Lasertriangulationssystems”. In: *tm - Technisches Messen* 88.s1 (2021), s59–s64. DOI: doi:10.1515/teme-2021-0060.
- [J-8] Xingchen Dong, Ali K. Yetisen, Jie Dong, **Kun Wang**, Patrick Kienle, Martin Jakobi, and Alexander W. Koch. “Hyperspectral Fingerprints for Atomic Layer Mapping of Two-Dimensional Materials with Single-Layer Accuracy”. In: *The Journal of Physical Chemistry C* 125.30 (2021), pp. 16583–16590. DOI: 10.1021/acs.jpcc.1c03802. eprint: <https://doi.org/10.1021/acs.jpcc.1c03802>.
- [J-9] Michael H. Köhler, Michael Schardt, Michael Müller, Patrick Kienle, **Kun Wang**, Xingchen Dong, Carsten Giebeler, Benjamin R. Wiesent, Martin Jakobi, and Alexander W. Koch. “Static Fourier transform mid-infrared spectrometer with increased spectral resolution using a stepped mirror”. In: *OSA Continuum* 3.8 (Aug. 2020), pp. 2134–2142. DOI: 10.1364/OSAC.397095.
- [J-10] Patrick Kienle, Lorena Batarilo, Markus Akgül, Michael H. Köhler, **Kun Wang**, Martin Jakobi, and Alexander W. Koch. “Optical Setup for Error Compensation in a Laser Triangulation System”. In: *Sensors* 20.17 (2020). DOI: 10.3390/s20174949.
- [J-11] Xingchen Dong, Yucheng Zhang, Hongwei Li, Yuntian Yan, Jianqing Li, Jian Song, **Kun Wang**, Martin Jakobi, Ali K. Yetisen, and Alexander W. Koch. “Microscopic Image Deblurring by a Generative Adversarial Network for 2D Nanomaterials: Implications for Wafer-Scale Semiconductor Characterization”. In: *ACS Applied Nano Materials* 5.9 (2022), pp. 12855–12864. DOI: 10.1021/acsnam.2c02725. eprint: <https://doi.org/10.1021/acsnam.2c02725>.
- [J-12] Xingchen Dong, Hongwei Li, Zhutong Jiang, Theresa Grünleitner, İnci Güler, Jie Dong, **Kun Wang**, Michael H. Köhler, Martin Jakobi, Bjoern H. Menze, Ali K. Yetisen, Ian D. Sharp, Andreas V. Stier, Jonathan J. Finley, and Alexander W. Koch. “3D Deep Learning Enables Accurate Layer Mapping of 2D Materials”. In: *ACS Nano* 15.2 (2021). PMID: 33464815, pp. 3139–3151. DOI: 10.1021/acsnano.0c09685. eprint: <https://doi.org/10.1021/acsnano.0c09685>.
- [J-13] Xingchen Dong, Hongwei Li, Yuntian Yan, Haoran Cheng, Hui Xin Zhang, Yucheng Zhang, Tien Dat Le, **Kun Wang**, Jie Dong, Martin Jakobi, et al. “Deep-Learning-Based Microscopic Imagery Classification, Segmentation, and Detection for the Identification of 2D Semiconductors”. In: *Advanced Theory and Simulations* (2022), p. 2200140.

## Preprints

- [P-1] **Kun Wang**, Yosuke Mizuno, Xingchen Dong, Wolfgang Kurz, Maximilian Fink, Heeyoung Lee, Martin Jakobi, and Alexander W. Koch. *Fiber-optic multimode interference sensing: comprehensive characterization and its potential for strain-insensitive temperature sensing*. 2022. DOI: 10.48550/ARXIV.2204.11044.
- [P-2] Maximilian Fink, Michael Schardt, Valentin Baier, **Kun Wang**, Martin Jakobi, and Alexander W. Koch. *Full-Waveform Modeling for Time-of-Flight Measurements based on Arrival Time of Photons*. 2022. DOI: 10.48550/ARXIV.2208.03426.

## Conference Publications

- [C-1] **Kun Wang**, Yosuke Mizuno, Kazuya Kishizawa, Yuma Toyoda, Heeyoung Lee, Koichi Ichige, Wolfgang Kurz, Xingchen Dong, Martin Jakobi, and Alexander W. Koch. "Accuracy improvement in POF-MMI-based temperature sensing by higher-order mode excitation". In: *30th International Conference on Plastic Optical Fibers (POF 2022)*. 2022, Paper 12.
- [C-2] **Kun Wang**, Xingchen Dong, Michael H Köhler, Patrick Kienle, Qiang Bian, Maximilian Fink, Martin Jakobi, and Alexander W Koch. "Optical fiber sensors based on multimode interference using square-core fiber for temperature measurement". In: *Photonic Instrumentation Engineering VIII*. Vol. 11693. International Society for Optics and Photonics. 2021, 116930R.
- [C-3] Xingchen Dong, **Kun Wang**, Jie Dong, Michael H Köhler, Martin Jakobi, and Alexander W. Koch. "Hyperspectral Imaging Microscopy and Nanoscopy: Theory and Practice". In: *DokDok 2019/*. 2019.
- [C-4] Michael H. Köhler, Bastian C. Vauth, Clara J. Kiesselbach, Xingchen Dong, **Kun Wang**, Patrick Kienle, Michael Schardt, Carsten Giebeler, Benjamin R. Wiesent, and Alexander W. Koch. "Compact static Fourier transform spectrometer for time-resolved mid-infrared spectroscopy". In: *Electro-Optical and Infrared Systems: Technology and Applications XVII*. Ed. by Duncan L. Hickman and Helge Bürsing. Vol. 11537. International Society for Optics and Photonics. SPIE, 2020, p. 1153707. DOI: 10.1117/12.2571489.
- [C-5] Patrick Kienle, Michael H. Köhler, **Kun Wang**, Martin Jakobi, and Alexander W. Koch. "Increasing the sensitivity of laser triangulation systems using structured optical surfaces". In: *ODS 2020: Industrial Optical Devices and Systems*. Ed. by Ryuichi Katayama and Yuzuru Takashima. Vol. 11500. International Society for Optics and Photonics. SPIE, 2020, 115000J. DOI: 10.1117/12.2566094.
- [C-6] Xingchen Dong, Michael H. Köhler, **Kun Wang**, Martin Jakobi, and Alexander W. Koch. "Mapping the optical dielectric response of isolated monolayer MoS<sub>2</sub> by push-broom microspectroscopy". In: *Unconventional Optical Imaging II*. Ed. by Corinne Fournier, Marc P. Georges, and Gabriel Popescu. Vol. 11351. International Society for Optics and Photonics. SPIE, 2020, p. 113511I. DOI: 10.1117/12.2540501.
- [C-7] Xingchen Dong, Zhendong Li, Jie Dong, **Kun Wang**, Michael H. Köhler, Martin Jakobi, and Alexander W. Koch. "Line-scan hyperspectral imaging microscopy with structured illumination". In: *Unconventional Imaging and Adaptive Optics 2020*. Ed.

by Jean J. Dolne and Mark F. Spencer. Vol. 11508. International Society for Optics and Photonics. SPIE, 2020, 115080U. DOI: 10.1117/12.2565944.

- [C-8] Michael H. Köhler, Michael Schardt, Hamza B. Ghazala, Ennio Colicchia, Patrick Kienle, Xingchen Dong, **Kun Wang**, and Alexander W. Koch. "Static Fourier transform mid-infrared spectrometer with continuous background correction". In: *Applied Optical Metrology III*. Ed. by Erik Novak and James D. Trolinger. Vol. 11102. International Society for Optics and Photonics. SPIE, 2019, p. 1110218. DOI: 10.1117/12.2528404.

## Supervised Students

- [S-1] "Dimming Curve Evaluation For Light Industry". Bachelor thesis. Munich, Germany: Technical University of Munich, Aug. 2019.
- [S-2] "Simulation of multimode fiber sensing using COMSOL". IAESTE exchange student. Munich, Germany: Technical University of Munich, Sept. 2019.
- [S-3] "Multimode Fiber Imaging Using Neural Networks". Master thesis. Munich, Germany: Technical University of Munich, May 2021.
- [S-4] "Imaging through the multimode fiber with neural networks". Bachelor thesis. Munich, Germany: Technical University of Munich, June 2021.
- [S-5] "Simulation of beam propagation in SMS fibres with Matlab using open-source software". Bachelor thesis. Munich, Germany: Technical University of Munich, Sept. 2021.
- [S-6] "Study of factors affecting the sensitivities of SMS fiber sensors". Bachelor thesis. Munich, Germany: Technical University of Munich, Dec. 2021.
- [S-7] "Optimization of a Single Multimode Fiber Imaging System". Research practice. Munich, Germany: Technical University of Munich, Apr. 2022.
- [S-8] "Strain-insensitive temperature sensing with SMS fiber sensor". Engineer practice. Munich, Germany: Technical University of Munich, Apr. 2022.
- [S-9] "Characterization of core-offset SMS fiber sensors for temperature and strain sensing". Bachelor thesis. Munich, Germany: Technical University of Munich, May 2022.
- [S-10] "The process of seeing through multimode fiber". Advanced seminar. Munich, Germany: Technical University of Munich, July 2022.
- [S-11] "Investigation of deep learning methods for multimode fiber image reconstruction". Bachelor thesis. Munich, Germany: Technical University of Munich, Sept. 2022.
- [S-12] "Comparison of Neural Networks for Multimode Fiber Imaging". Research practice. Munich, Germany: Technical University of Munich, Oct. 2022.
- [S-13] "Neural networks applied on multimode fiber imaging and the performance degradation due to external perturbations". Master thesis. Munich, Germany: Technical University of Munich.